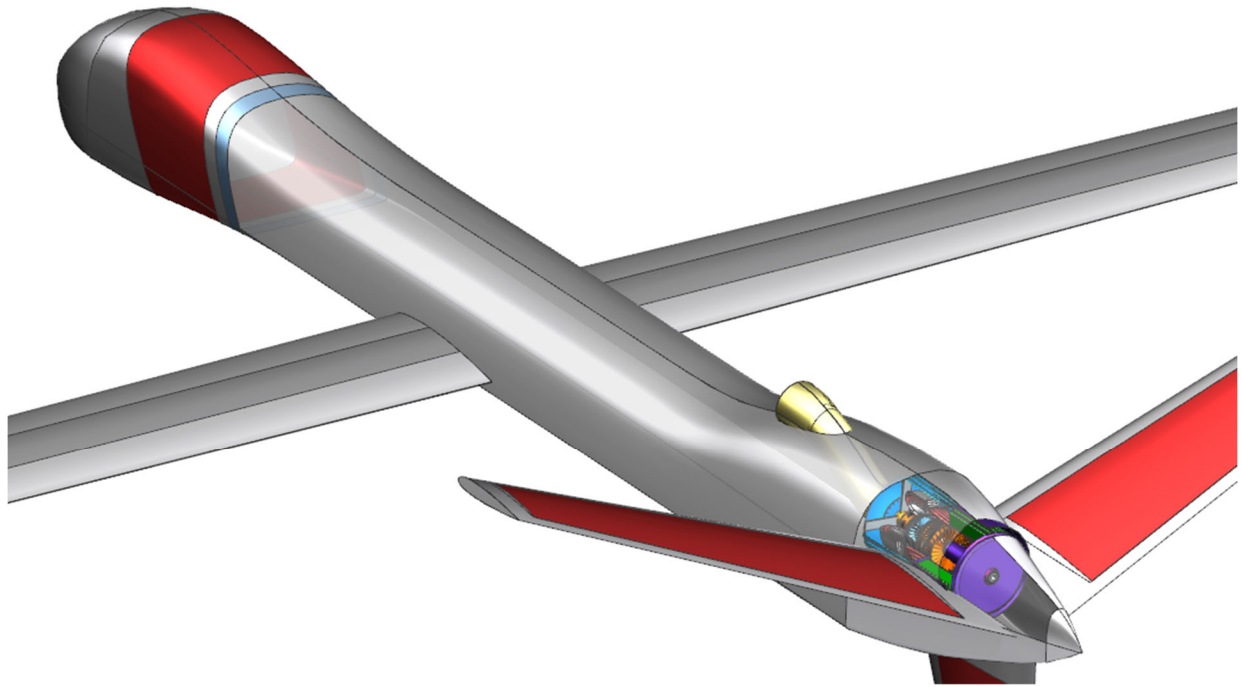


# **SR-1000BDE: A Next Generation Hybrid Electric Medium**

## **Altitude Long Endurance Gas Generator**



### **Faculty Advisors:**

Saeed Farokhi and Ray Taghavi

### **Team Lead:**

Jacksen Goyer

### **Team Members:**

Tim Aiken

Anthony Bendure

Blake Hartwell

Ryan Niday

Jameson Poth

Charles Richmond



Department of Aerospace Engineering

May 16th, 2019

---

**SR-1000BDE (Search and Rescue – 1000 Best Design Ever): A Next Generation Hybrid Electric Medium Altitude Long Endurance Gas Generator**

Design Team:

Timothy Aiken  
# 977202



Anthony Bendure  
# 907961



Jackson Goyer  
# 952602  
Team Lead



Blake Hartwell  
# 952604



Ryan Niday  
# 908355



Jameson Poth  
# 952682



Charles Richmond  
# 952608

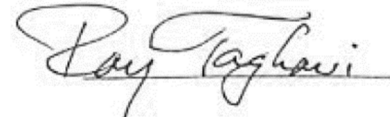


Faculty Advisors:

Dr. Saeed Farokhi  
# 005092



Dr. Ray Taghavi  
# 024860



---

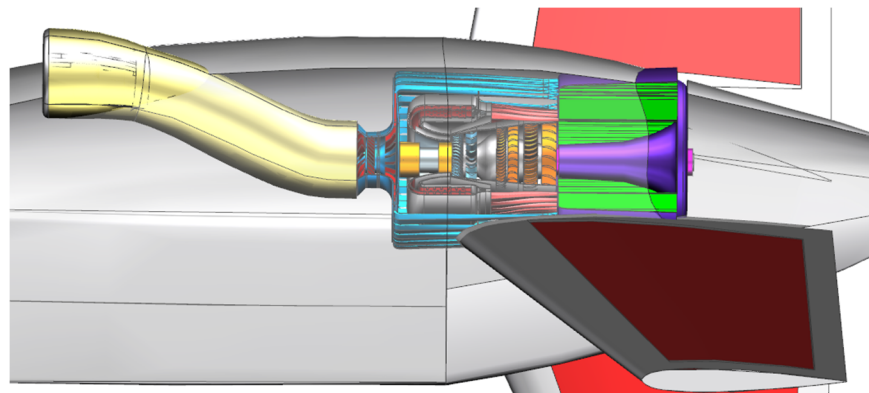
**Abstract**

The following report outlines the design of the SR-1000BDE turboshaft replacement engine for the TPE331-10 for use in a hybrid electric medium altitude long endurance search and rescue unmanned aerial vehicle (UAV). The SR-1000BDE incorporates several advanced technologies and concepts, available in 2025 for the engine's entry-into-service (EIS) date, that improve upon the TPE331-10 including:

- Additive manufacturing of accessory and subsystem components;
- High-efficiency engine components;
- Heat recuperator;
- Ceramic matrix composites.

The major design drivers for the following engine were to improve fuel consumption and maximize vehicle flight loiter time, while providing similar shaft power at a reduced engine weight. A heat exchanger is implemented into the cycle to provide a significant increase in thermal efficiency that decreases overall fuel consumption. Advanced, high temperature materials and coatings are used to eliminate turbine cooling and allow for the combustor to run at higher temperatures. Incorporating advanced materials and technologies in the SR-1000BDE drives down the weight and fuel consumption of the designed engine.

The SR-1000BDE offers a 40% decrease in power specific fuel consumption and a 41% decrease in fuel mass flow rate at loiter compared to the TPE331-10, while maintaining a maximum shaft power of 985 hp at takeoff. The following image presents the SR-1000BDE integrated into a sample aircraft.



<b>Performance</b>	
<b>Maximum speed</b>	260 KEAS
<b>Cruise speed</b>	220 KTAS
<b>Mission Fuel Burn</b>	602 gal
<b>Cruise BSFC</b>	0.325 lb/(hp*h)
<b>Takeoff BSFC</b>	0.329 lb/(hp*h)
<b>Engine Weight</b>	86.48 lbf
<b>Fan Diameter</b>	N/A
<b>Required Trade Studies</b>	
<b>Engine Cycle Design Space Carpet Plots Page #</b>	5, 6
<b>In-Depth Cycle Summary Page #</b>	7
<b>Final engine flowpath (Page #)</b>	9
<b>Final cycle study using chosen cycle program (Page #)</b>	7
<b>Detailed stage-by-stage turbomachinery design information (Page # for each component)</b>	32, 35 (Compressor) 65 (Turbine)
<b>Detailed design of velocity triangles for first stage of each component (list page #'s and component)</b>	30, 35 (Compressor) 68 (Turbine)

<b>Summary Data</b>	
<b>Design MN</b>	0.31
<b>Design Altitude</b>	7000ft
<b>Design Shaft Horsepower</b>	632
<b>Design BSFC</b>	0.308 lb/(hp*h)
<b>Design Overall Pressure Ratio</b>	9.83
<b>Design T4.1</b>	2170°R
<b>Design Engine Pressure Ratio</b>	9.83
<b>Design Fan / LPC Pressure Ratio</b>	N/A
<b>Design Chargeable Cooling Flow (%@25)</b>	0
<b>Design Non-Chargeable Cooling Flow (%@25)</b>	0

## Table of Contents

	Page #
Abstract .....	iii
List of Figures .....	v
List of Tables .....	vii
List of Symbols .....	viii
Acknowledgements .....	xi
1 Introduction .....	1
2 Concepts in Advanced Cycle Design .....	1
2.1 Engine Concepts for SR-1000BDE .....	2
2.2 Engine Components and Diagrams .....	3
2.3 On-Design Analysis of the Baseline Engine .....	3
2.4 Advanced Technologies and Concepts .....	4
2.5 On-Design Analysis of SR-1000BDE .....	5
2.6 Off-Design Analysis of SR-1000BDE .....	7
2.7 Performance Comparison with the Baseline Engine .....	8
3 Engine Flow Path .....	9
4 Detailed Component Design .....	10
4.1 Engine Subsonic Inlet .....	10
4.2 Compressor .....	24
4.3 Recuperator .....	39
4.4 Combustor .....	46
4.5 Turbine .....	61
4.6 Engine Exhaust .....	74
5 Engine Subsystems .....	75
5.1 Foil Bearing System .....	75
5.2 Starting System .....	76
5.3 Full Authority Digital Engine Control .....	77
5.4 Advanced Operational Concepts .....	79
6 SR-1000 BDE Cost Estimation .....	80
7 SR-1000 BDE Weight Estimation .....	81
8 Request for Proposal Requirements Summary .....	82
9 Engine Exploded View .....	83
10 References .....	84

## List of Figures

Figure 2.1: Station Map for SR-1000BDE [5] .....	3
Figure 2.2: Reverse Flow Combustor Configuration [4] .....	4
Figure 2.3: Parametric Study Showing SHP, PSFC, T4, and Mass Flow Rate [5] .....	5
Figure 2.4: Parametric Study for OPR and T4 [5] .....	6
Figure 4.1: SR-1000BDE Subsonic Transitioning S-Duct Inlet .....	10
Figure 4.2: Effect of Vortex Generators on Stall Mitigation [12] .....	11
Figure 4.3: Electro-Impulse De-Icing Operation [15] .....	12
Figure 4.4: Electrical Connection Diagram of EIDI System [14] .....	13
Figure 4.5: Spillage Drag and Highlight Area Calculations for Loiter and Cruise Flight Conditions .....	14
Figure 4.6: Average Wall Angle Sizing with Respect to Geometric Stall Data [19] .....	15
Figure 4.7: Throat Curvature Effect [18] .....	15
Figure 4.8: Duct Length Sizing .....	16



Figure 4.9: S-Duct Centerline and Area Distributions .....	17
Figure 4.10: External Geometry of Inlet.....	17
Figure 4.11: Wireframe Model of Transitioning S-Duct SR-1000BDE Inlet .....	18
Figure 4.12: Inlet Cross-Section of General Atomic MQ-9 Reaper [21] .....	18
Figure 4.13: Inlet Face Aspect Ratio Limits with Respect to Geometric Stall Margin Data [22].....	18
Figure 4.14: Slices for Capturing Inlet Transition.....	19
Figure 4.15: Cross-Section Shape Transition from Inlet Throat to Slice 6 .....	20
Figure 4.16: Internal Geometry of BDE Inlet.....	20
Figure 4.17: Definition Sketch of VG Geometry [12].....	21
Figure 4.18: Vortex Generator Dimensions.....	22
Figure 4.19: 3-D Printed Inlet Screen [23] .....	22
Figure 4.20: Inlet Structural Layout .....	24
Figure 4.21: Velocity Triangle Definition Sketch [9].....	27
Figure 4.22: Three Stream Surface Velocity Triangles .....	30
Figure 4.23: NACA-65 Series Cascade Data [10].....	31
Figure 4.24: Axial Compressor Conceptual 3-View .....	32
Figure 4.25: Impeller Exit Velocity Triangle Definition Sketch [9] .....	33
Figure 4.26: Centrifugal Compressor Velocity Triangles .....	35
Figure 4.27: Centrifugal Compressor Conceptual 3-View .....	36
Figure 4.28: Adjustment Factor Based on Reynolds Number [9] .....	37
Figure 4.29: Stall Margin Chart [33] .....	37
Figure 4.30: Allowable Stress vs. Temperature [9].....	38
Figure 4.31: 3-View of the Compressor .....	39
Figure 4.32: 4/3/4 elliptical tube MTU-heat exchanger matrix [39] .....	40
Figure 4.33: Comparative performance of power generation gas turbine variants [36].....	41
Figure 4.34: Recuperator effectiveness over time [36,37,40].....	42
Figure 4.35: Designed recuperator dimensions (not to scale).....	44
Figure 4.36: Radial recuperator [36] .....	44
Figure 4.37: Sample mullite ceramic recuperator [36].....	45
Figure 4.38: Isometric View of the Recuperator .....	46
Figure 4.39: Configuration cutaway .....	47
Figure 4.40: Correlation of $\theta$ -parameter to combustion efficiency [9].....	48
Figure 4.41: Flammability limits for kerosene type fuel [9].....	49
Figure 4.42: Definition sketch for dump diffuser (left) [45], wide angle diffuser with splitter vanes (center) [45], and hybrid diffuser (right) [47] .....	50
Figure 4.43: Dump gap term definitions.....	51
Figure 4.44: Relationship of CO and UHC production to combustor inlet temperature [54].....	52
Figure 4.45: NO <sub>x</sub> production as a function of equivalence ratio [9].....	53
Figure 4.46: Temperature dependence of regulated pollutants [8] .....	53
Figure 4.47: Correlation of cooling effectiveness to mass flow fraction [9] .....	55
Figure 4.48: Air partitioning definition sketch [58] .....	55
Figure 4.49: Liner and reference height definitions .....	56
Figure 4.50: Injectors and swirlers .....	58
Figure 4.51: Relight envelope [9].....	59
Figure 4.52: Hole spacing definition sketch .....	61
Figure 4.53: Combustor Isometric View .....	61
Figure 4.54: Constant Pitchline Turbine Definition Sketch [9].....	63
Figure 4.55: Stage Definition Sketch [9].....	64
Figure 4.56: Velocity Triangles for the Turbine.....	67

Figure 4.57: One Stage Gas Generator Turbine and Two-Stage Power Turbine Flowpath .....	70
Figure 4.58: Blade Design Definition Sketch [9] .....	70
Figure 4.59: Cutout of the Turbine .....	71
Figure 4.60: Smith Chart [9].....	73
Figure 4.61: Three View of the Turbine .....	74
Figure 4.62: Exhaust Nozzle.....	75
Figure 5.1: Foil Thrust Bearing [80].....	76
Figure 5.2: CAD of Foil Bearing on Left with Bump Foil Schematic Shown on Right [75].....	76
Figure 5.3: Layout of Bearings with Starter Shown in the SR-1000BDE .....	77
Figure 5.4: SR-1000BDE FADEC Engine Control and Sensor Schematic.....	79
Figure 5.5: A Comparison of Viable Operational Concepts with Respect to Loiter Time.....	80
Figure 9.1: SR-1000BDE Exploded View.....	83

### **List of Tables**

Table 2.1: Baseline Cycle at Loiter [5].....	4
Table 2.2: Cycle Efficiencies and Parameters .....	5
Table 2.3: Summary of Cycle for SR-1000BDE [5] .....	7
Table 2.4: Off-Design at Takeoff SLS Condition.....	7
Table 2.5: Off-Design at Takeoff +27°F Std. Day .....	7
Table 2.6: Off-Design at Cruise Condition.....	7
Table 2.7: SR-1000BDE Mission Profile .....	8
Table 2.8: Baseline Engine Mission Profile .....	8
Table 2.9: SR-1000BDE Comparison to Baseline Engine .....	8
Table 4.1: Salient Characteristics of SR-1000BDE Inlet .....	10
Table 4.2: Diffuser Flow Quality Improvements Due to Vortex Generators [11].....	12
Table 4.3: EIDI Energy Requirement Comparison with Thermal Strategies [14].....	13
Table 4.4: Optimized Parameters Referenced for VG Design [12].....	21
Table 4.5: Inlet Material Properties [28] [29] [30].....	23
Table 4.6: Compressor Cycle Parameters.....	25
Table 4.7: Compressor Inlet Flow Parameters.....	25
Table 4.8: Compressor Inlet Geometric Parameters.....	25
Table 4.9: Axial Compressor Parameters with Guidelines [9] .....	26
Table 4.10: Axial Compressor Stage Parameters .....	32
Table 4.11: Centrifugal Compressor Parameters .....	35
Table 4.12: Stress Analysis Results.....	38
Table 4.13: Initial values for the recuperator thermodynamic design .....	41
Table 4.14: Values used for matrix volume estimation .....	43
Table 4.15: Major combustor cycle parameters.....	46
Table 4.16: Station descriptions .....	47
Table 4.17: Values for calculating efficiency.....	49
Table 4.18: Diffuser exit flow characteristics.....	50
Table 4.19: Salient characteristics of combustor zones .....	56
Table 4.20: Dome geometry .....	56
Table 4.21: Total pressure loss breakdown. ....	57
Table 4.22: Hole distribution and size for air partitioning .....	58
Table 4.23: Flight conditions from RFP [1] .....	60
Table 4.24: Combustor material properties .....	60
Table 4.25: HPT Flow Data.....	62
Table 4.26: LPT Flow Data .....	62



Table 4.27: HPT Stage Design .....	65
Table 4.28: LPT Stage Design .....	66
Table 4.29: Stage Parameters .....	68
Table 4.30: HPT Temperature and Pressure Characteristics .....	68
Table 4.31: LPT Temperature and Pressure Characteristics .....	69
Table 4.32: Radii through the Turbine .....	69
Table 4.33: Salient Blade Design Characteristics .....	71
Table 4.34: Blade Stresses .....	72
Table 4.35: Turbine Efficiency .....	73
Table 4.36: Exhaust Nozzle Parameters .....	75
Table 4.37: Exhaust Nozzle Flow Data .....	75
Table 7.1: SR-1000BDE Weight Estimation .....	81

### List of Symbols

<u>Symbol</u>	<u>Description</u>	<u>Units</u>
$a$	Local speed of sound	m/s, ft/s
$a$	Semimajor axis of inlet elliptic lip (internal)	m, ft
$A_0$	Inlet (freestream) capture area	m <sup>2</sup> , ft <sup>2</sup>
$A_1$	Inlet capture area	m <sup>2</sup> , ft <sup>2</sup>
$A_L$	Liner area	m <sup>2</sup> , ft <sup>2</sup>
$A_R$	Casing area	m <sup>2</sup> , ft <sup>2</sup>
$A_{th}$	Inlet throat area	m <sup>2</sup> , ft <sup>2</sup>
$b$	Semiminor axis of inlet elliptic lip (internal)	m, ft
$b$	Axial length	m, ft
$b$	Function of fuel/air ratio	~
$B_t$	Thickness of turbulent boundary layer	m, ft
$\vec{C}$	Absolute velocity vector	m/s, ft/s
$C_r, C_\theta, C_z$	Radial, tangential, axial velocity components in the absolute frame of reference	m/s, ft/s
$C_h$	Stalling pressure rise coefficient	~
$C_{heff}$	Effective stalling pressure rise coefficient	~
$c_p$	Specific heat at constant pressure	J/kg*K, BTU/lbm*°R
$c_z$	Axial chord length	m, ft
$c$	Chord length	m, ft
$D$	Diameter	m, ft
$D$	Diffusion factor in turbomachinery	~
$D_g$	Dump gap	m, ft
$D_h$	Hole diameter	m, ft
$D_{add}$	Additive drag	N, lbf
$D_{spillage}$	Spillage drag	N, lbf
$e_c, e_t$	Polytropic efficiency of compressor or turbine	~
$F_{lip}$	Lip suction force	N, lbf
$F_{ef}$	Correction factor	~
$g$	Staggered spacing	m, ft
$h$	Height	m, ft
$h$	Enthalpy	J, BTU
$H$	Height	m, ft
$i$	Incidence angle	rad
$K$	Correction factor	~
$L$	Length	m, ft
$\dot{m}$	Mass flow rate	kg/s, lb/s
$M_T$	Blade tangential Mach number	~

$M_r$	Relative Mach number	~
$M_z$	Axial Mach number	~
$M$	Mach number	~
$n$	Exponent of superellipse	~
$N$	Number of blades	~
$N_h$	Number of holes	~
$o$	Throat opening	m, ft
$p$	Static pressure	Pa, psia
$p_t$	Total pressure	Pa, psia
$Pr$	Prandtl number	~
$q$	Dynamic pressure	Pa, psia
$q'$	Relative dynamic pressure	Pa, psia
$\dot{q}$	Heat transfer rate	W, BTU/s
$Q$	Heat exchange	J, BTU
$Re$	Reynolds number	~
$R$	Gas Constant	J/kg*K, BTU/lbm-°R
°R	Degree of reaction	~
$r$	Radius	m, ft
$r, \theta, z$	Cylindrical coordinates	~
$S$	Sharpness	~
$S'$	Swirl number	~
$s$	Spacing	m, ft
$T$	Static temperature	K, °R
$T_g$	Gas temperature	K, °R
$T_m$	Maximum wall temperature	K, °R
$T_t$	Total temperature	K, °R
$t$	Thickness	m, ft
$U$	Overall heat transfer coefficient	W/m²K, BTU/ft²°R
$\vec{U}$	Rotational velocity vector of rotor	m/s, ft/s
$V$	Volume	m³, ft³
$w$	Weight	kg, lb
$w_a$	Combustor inlet airflow	kg/s, lb/s
$W$	Mass flow rate	kg/s, lb/s
$\vec{W}, W$	Relative velocity vector, relative flow speed	m/s, ft/s
$W_r, W_\theta, W_z$	Radial tangential and axial velocity components in relative frame of reference	m/s, ft/s

<b><u>Greek Symbol</u></b>	<b><u>Description</u></b>	<b><u>Units</u></b>
----------------------------	---------------------------	---------------------

$\alpha$	Angle of attack	rad
$\alpha$	optimal area ratio	~
$\beta$	Relative flow angle with respect to the axial direction	rad
$\beta$	Area density	kg/m², lb/ft²
$\Gamma$	Circulation	~
$\delta^*$	Deviation angle	rad
$\gamma$	Ratio of specific heats	~
$\gamma^\circ$	Stagger angle	rad
$\Delta$	Difference	~
$\delta$	Boundary layer thickness	m, ft
$\epsilon$	Slip factor	~
$\epsilon_r$	Recuperator effectiveness	~
$\eta_{HPT}$	High Pressure Turbine efficiency	~
$\eta_{LPT}$	Low Pressure Turbine efficiency	~
$\theta$	Theta Parameter	~
$\theta$	Angle	rad



$\kappa$ .....	Thermal conductivity coefficient.....	W/mK, BTU/ft <sup>2</sup> °R
$\pi_c$ .....	Compressor total pressure ratio.....	~
$\pi_d$ .....	Inlet total pressure recovery.....	~
$\rho$ .....	Fluid Density.....	kg/m <sup>3</sup> , lbm/ft <sup>3</sup>
$\dot{\rho}$ .....	Power.....	W, BTU
$\sigma$ .....	Cascade or blade solidity.....	~
$\sigma$ .....	Stress.....	Pa, psia
$\sigma_{hoop}$ .....	Hoop stress.....	Pa, psia
$\tau$ .....	Total temperature ratio.....	~
$\varphi$ .....	Camber angle.....	rad
$\varphi$ .....	Diffuser wall divergence angle.....	rad
$\varphi$ .....	Flow coefficient.....	~
$\varphi$ .....	Equivalence ratio.....	~
$\Phi$ .....	Cooling effectiveness parameter.....	~
$\psi$ .....	Stage loading parameter.....	~
$\omega$ .....	Angular speed.....	rad/s, rpm

**Subscripts**

**Description**

1,2.....	Station numbering
b.....	Burner
c.....	Chord
c.....	Cold, cooling
c.....	Compressor
crit.....	Critical
CB.....	Center body
DZ.....	Dilution zone
h.....	Hub
h.....	Hot
lm.....	Logarithmic mean
L.....	Liner
m.....	Pitchline
max.....	Maximum
PZ.....	Primary zone
ref.....	Reference
R.....	Casing
r.....	Relative
sw.....	Swirler, swirl
SZ.....	Secondary zone
t.....	Tip
t.....	Total or Stagnation
th.....	Throat
tot.....	Total
VG.....	Vortex Generator
w.....	Wall

**Abbreviations and Acronyms**

**Description**

AIAA.....	American Institute of Aeronautics and Astronautics
AIP.....	Aerodynamic Interface Plane
CAD.....	Computer Aided Design
CMC.....	Ceramic Matrix Composite
CO.....	Carbon Monoxide
CO <sub>2</sub> .....	Carbon Dioxide
DPCP.....	Circumferential Distortion Intensity



---

DZ.....	Dilution Zone
D-Factor.....	Diffusion Factor
EBC.....	Environmental Barrier Coating
EEC.....	Engine Electronic Controller
EIDI.....	Electro-Impulse De-icing
EIS.....	Entry-into-Service
FAA.....	Federal Aviation Administration
FADEC.....	Full Authority Digital Engine Control
FOD.....	Foreign Object Damage
GE.....	General Electric
HP.....	Horse Power
H <sub>2</sub> O.....	Water Vapor
HPT.....	High-Pressure Turbine
HRPMM.....	High Reactance Permanent Magnet Starter/Generator
HUMS.....	Health and Usage Monitoring System
ICAO.....	International Civil Aviation Organization
LPT.....	Low Pressure Turbine
MS.....	Margin of Safety
NASA.....	National Aeronautics and Space Administration
NO <sub>x</sub> .....	Nitrogen Oxides
OPR.....	Operating Pressure Ratio
PR.....	Pressure Ratio
PSFC.....	Power Specific Fuel Consumption
PZ.....	Primary Zone
RFP.....	Request for Proposal
RPM.....	Rotations Per Minute
SHP.....	Shaft Horse Power
SLS.....	Sea Level Static
SN.....	Summerfield Number
Std.....	Standard
SZ.....	Secondary Zone
TBC.....	Thermal Barrier Coating
TRL.....	Technology Readiness Level
UAV.....	Unmanned Aerial Vehicle
UHC.....	Unburned Hydrocarbons
VG.....	Vortex Generators

**Acknowledgements**

The team would like to thank Dr. Saeed Farokhi and Dr. Ray Taghavi for their continued support and devotion to teaching us the fundamentals of aircraft propulsion. We would also like to thank Dr. Ian Halliwell for helping us to understand the gas turbine industry. Lastly, we would like to thank Dr. Christopher Depcik for building the foundation of our thermodynamic understanding and Dr. Mark Ewing for developing our basic structures knowledge. You all have helped in both this project and our overall understanding of aircraft engines.



## **1 Introduction**

The Request for Proposal (RFP) [1] called for a candidate engine to be used as the power generator for a hybrid-electric UAV. The current baseline engine that the SR-1000BDE will replace is the TPE331-10, first designed by Honeywell over 50 years ago [2]. The new turboshaft engine must have a lower fuel consumption, 20+ hour loiter time, and produce a similar power output while fitting within a similar engine envelope.

Recent advancements in unmanned aircraft have allowed for an increased capacity for UAVs to perform a range of dangerous tasks in emergency situations that were typically only trusted to manned missions. The effectiveness of unmanned search-and-rescue operations have proven that UAVs can find victims faster and with a success rate similar to their human-controlled counterparts [3]. Search and rescue vehicles strive to maximize flight times, and current trends are replacing typical gas turbine propulsion applications with a hybrid-electric propulsion system. The RFP requests a design to replace the turboprop gas turbine engine with an optimized gas turbine generator to pair with a previously designed hybrid-electric configuration.

The SR-1000BDE incorporates several cutting-edge technologies and concepts that allow it to meet and exceed the RFP requirements. The use of a recuperator provides a boost to thermal efficiency which drastically lowers fuel consumption. Ceramic matrix composites (CMCs) were used to decrease the weight of hot section components and eliminate turbine cooling. The use of CMCs also allows for higher combustor liner temperatures and less cooling air, providing a more uniform temperature profile at the turbine inlet.

## **2 Concepts in Advanced Cycle Design**

This section documents the design philosophies and performance analysis for the SR-1000BDE. It discusses the baseline cycle, the creation and optimization of a new cycle, and a comparison between the two cycles.

Responses to the RFP are required to have 25% fuel savings at loiter, be able to loiter for at least 20 hours, have a 10% increase in power to weight ratio, be lighter than the baseline engine, and stay within 5% of the power output of the baseline engine. It is also desired to have technical feasibility and low operating costs [1]. These will be the driving factors for the new design.

## **2.1 Engine Concepts for SR-1000BDE**

There were four cycles designs that were investigated for the SR-1000BDE:

- Original engine architecture with EIS dated efficiencies and trends;
- High-efficiency engine architecture using axial and centrifugal compressor stages with a higher cycle pressure ratio and a higher burner exit temperature;
- High-efficiency engine architecture using axial and centrifugal compressor stages, a reverse annular combustor, and a recuperator;
- High-efficiency engine architecture using axial and centrifugal compressor stages, a reverse annular combustor, and an intercooler.

Concept 1 uses complex architecture involving two centrifugal compressors and a reverse annular combustor. This design experiences a lot of pressure losses due to turning the flow. However, the design is very compact, which saves space on the aircraft. This design runs both centrifugal compressors off the same spool, which saves weight and manufacturing costs by not requiring a second shaft.

Concept 2 reduces pressure losses by having a single spool axial stage and centrifugal stage in the compressor. This design has a high cycle pressure ratio and a high burner exit temperature.

Concept 3 has a single spool compressor with an axial stage combined with a centrifugal stage. It also utilizes a recuperator to increase thermal efficiency and decrease fuel consumption. This cycle allows for a reduced cycle pressure ratio, and a lower burner exit temperature.

Concept 4 is similar to Concept 3, except it replaces the recuperator with an intercooler. The intercooler decreases the temperature between the compressor stages. This allows for better combustion and more power generation.

Concept 3 was selected for its lower fuel usage. The design is compact and the increase in complexity is offset by the fuel savings. Concept 3 was selected over Concept 2 because the decrease in burner exit temperature eliminates the need for cooling in the turbine. Concept 4 was not chosen due to the higher fuel consumption.

## 2.2 Engine Components and Diagrams

The schematic of an arbitrary cycle that is similar to the SR-1000BDE is shown in Figure 2.1. This figure was taken from GasTurb 13 [5]. The station numbers are defined as follows:

1. Inlet
2. Compressor Face
3. Compressor Exit
31. Recuperator Cold Side Inlet
35. Recuperator Cold Side Exit
4. Burner Exit
41. HPT Inlet
44. HPT Exit
45. LPT Inlet
5. LPT Exit
6. Recuperator Hot Side Inlet
7. Recuperator Hot Side Exit
8. Exhaust Exit

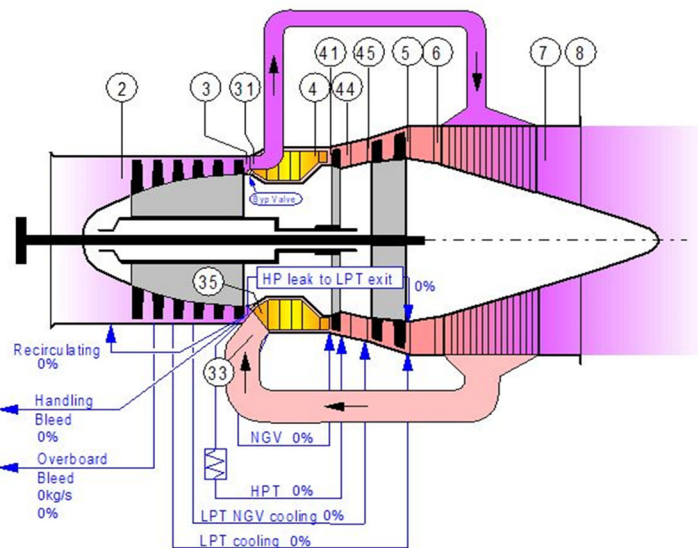


Figure 2.1: Station Map for SR-1000BDE [5]

## 2.3 On-Design Analysis of the Baseline Engine

The RFP provides a baseline cycle for the Honeywell TPE331-10 turboprop engine. GasTurb 13 was used to model the baseline cycle. The model matched the provided cycle, which validates the model and allows for optimization of that model. An off-design analysis of this cycle was then conducted for the



and the elimination of cooling in the turbine blades. The CMC turbine blades are approximately one-third the weight of metallic turbine blades and can handle temperatures up to 2860°R [6]. CMCs have been demonstrated on GE engines, which gives them a TRL of 9. Research from NASA Glenn has proven that CMCs can handle a surface temperature of 3160°R without the need of cooling. This is accomplished using environmental and thermal barrier coatings, EBCs and TBCs respectively [7]. This means that there is little risk that CMC technology will be ready at the EIS date of 2025.

**2.5 On-Design Analysis of SR-1000BDE**

The efficiencies and parameters in Table 2.2 were chosen using Mattingly’s Aircraft Engine Design 3<sup>rd</sup> Edition for an EIS of 2025 [8]. The nozzle pressure ratio was set to 1.1 following Farokhi [9]. This design choice was made to ensure the net thrust of the engine was positive.

**Table 2.2: Cycle Efficiencies and Parameters**

Inlet PR	Burner PR	Turbine Interduct PR	Turbine Exit PR	Nozzle PR	Burner Efficiency	$\epsilon_c$	$\epsilon_t$	$\eta_{HPT}$	$\eta_{LPT}$
0.998	0.969	0.998	0.998	1.1	0.999	0.9	0.9	0.995	0.995

With the design parameters chosen, the cycle needed to be designed a minimal fuel flow by conducting parametric studies. Figure 2.3 and Figure 2.4 show carpet plots that were used in the final selection of design parameters. The team decided to design the SR-1000BDE for the loiter flight condition, as this was the flight condition that the engine would be in the most. The black box in each plot depicts the

the optimized cycle that was chosen for the SR-1000BDE.

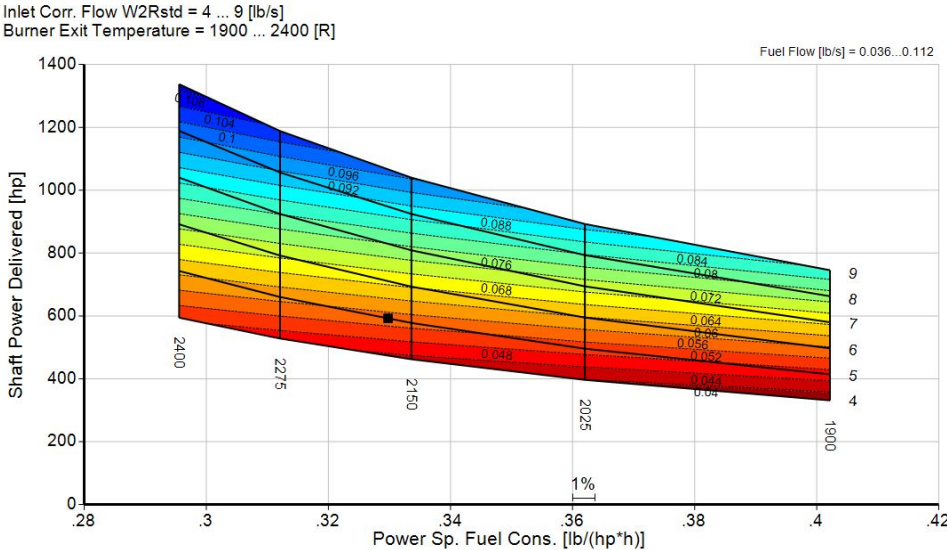


**Figure 2.3: Parametric Study Showing SHP, PSFC, T4, and Mass Flow Rate**

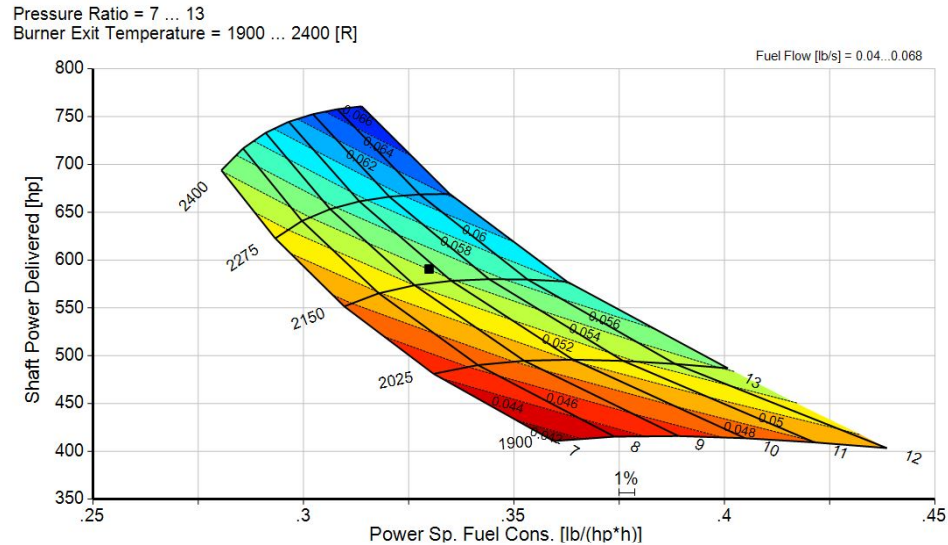


Figure 2.3 shows that the corrected mass flow rate at Station 2 is the driving factor for fuel flow. Decreasing the mass flow reduces the amount of fuel needed to maintain the same fuel-to-air ratio. A key thing to look for when decreasing mass flow rate, is the decrease in overall engine size as well. The plot shows that the burner exit temperature is the driver for PSFC.

Figure 2.4 shows that the cycle pressure ratio is a driver for PSFC. The plot also shows that T4 is a key parameter that contributes to the shaft power. The fuel flow rate is a function of both the burner exit temperature and the cycle pressure ratio.

The parametric studies allowed for the optimization of key parameters. Figure 2.3 was used to determine the inlet mass flow rate and the burner exit temperature. The inlet mass flow rate was set at 5

lb/s. This was chosen to help minimize PSFC. A smaller inlet mass flow rate could have been chosen, but it was deemed that the engine would then become



**Figure 2.4: Parametric Study for OPR and T4 [5]**

unrealistically small. To achieve a shaft horsepower of approximately 600hp, the burner exit temperature was set to 2170°R. When this burner exit temperature was evaluated in Figure 2.4, the optimal cycle pressure ratio was found to be 9.83. A cycle summary is shown in Table 2.3.

**Table 2.3: Summary of Cycle for SR-1000BDE [5]**

Station	W lb/s	T R	P psia	WRstd lb/s			
amb		493.71	11.340		PWSD =	590.8	hp
1	4.179	503.21	12.121		PSFC =	0.32953	lb/(hp*h)
2	4.179	503.21	12.097	5.000	Heat Rate=	6098.8	BTU/(hp*h)
3	4.179	1029.14	118.552	0.730	V0 =	337.70	ft/s
31	4.179	1029.14	118.552	0.331	FN res =	32.95	lb
35	4.179	1335.61	116.181		P35/P3 =	0.98000	
4	4.233	2170.00	112.811	1.128	WF =	0.05408	lb/s
41	4.233	2170.00	112.811	1.128	Therm Eff=	0.41765	
43	4.233	1718.23	38.937		P2/P1 =	0.99800	
44	4.233	1718.23	38.937		TRQ =	100.0	%
45	4.233	1718.23	38.859	2.913	P45/P44 =	0.99800	
49	4.233	1351.29	13.586		Incidence=	0.00000	°
5	4.233	1351.29	13.586	7.390	P6/P5 =	0.99800	
6	4.233	1351.29	13.558		PWX =	0	hp
7	4.233	1054.86	12.474		P7/P6 =	0.92000	
8	4.233	1054.86	12.474	7.111	P8/Pamb =	1.10000	
Bleed	0.000	1029.14	118.551		WB1d/w2 =	0.00000	
-----					A8 =	35.06	in <sup>2</sup>
Efficiencies:	isentr	polytr	RNI	P/P	WCHN/w2 =	0.00000	
Compressor	0.8651	0.9000	0.853	9.800	WCHR/w2 =	0.00000	
Burner	0.9990			0.971	Loading =	100.00	%
HP Turbine	0.9113	0.9000	1.435	2.897	WCLN/w2 =	0.00000	
LP Turbine	0.9117	0.9000	0.646	2.860	WCLR/w2 =	0.00000	
Heat Exch	0.9500				PW_gen =	573.0	hp
Generator	0.9700				eta t-s =	0.79524	
-----							
HP Spool mech Eff	0.9950	Nom Spd	38000	rpm			
PT Spool mech Eff	0.9950	Nom Spd	10000	rpm			
-----							
hum [%]	war0	FHV	Fuel				
0.0	0.00000	18500.0	Generic				

## 2.6 Off-Design Analysis of SR-1000BDE

GasTurb 13 was used for off-design analysis at both takeoff and cruise conditions. Table 2.4 shows the salient characteristics of off-design at takeoff, while Table 2.5 shows the key characteristics of off-design at +27°F Std. Day. Table 2.6 shows the key parameters at cruise conditions. Power generation at each condition is within 5% of the requirement.

**Table 2.4: Off-Design at Takeoff SLS Condition**

Mach Number	BSFC	T <sub>t4</sub> (°R)	Mass Flowrate	OPR	HP
0.0	0.329	2620	5.50	11.5	985

**Table 2.5: Off-Design at Takeoff +27°F Std. Day**

Mach Number	BSFC	T <sub>t4</sub> (°R)	Mass Flowrate	OPR	HP
0.0	0.479	2660	5.29	11.03	943

**Table 2.6: Off-Design at Cruise Condition**

Mach Number	BSFC	T <sub>t4</sub> (°R)	Mass Flowrate	OPR	HP
0.35	0.325	2460	3.83	11.62	669

## 2.7 Performance Comparison with the Baseline Engine

The SR-1000BDE must showcase a 25% fuel savings to reach a 20 hour loiter, a 10% increase in power to weight ratio at SLS, a power output within 5% of the baseline engine, and a range of 1000 nautical miles. The fuel used during the flight was found by generating a sample mission profile. The characteristics of the mission profile can be seen in Table 2.7 and Table 2.8. Table 2.9 shows the comparison of the SR-1000BDE to the baseline engine. The SR-1000BDE meets and exceeds all the requirements of the RFP, boasting a 41% fuel savings at loiter, a 74% increase in loiter time, and a 71% increase in range.

**Table 2.7: SR-1000BDE Mission Profile**

	Takeoff and Climb	Cruise Out	Loiter	Cruise Return	Landing
<b>HP</b>	985	668	632	668	468
<b>Fuel Flow (lbs/s)</b>	0.09002	0.0579	0.0541	0.0579	-
<b>Time (hr)</b>	0.035	0.17	20.28	0.17	0.08
<b>Altitude (ft)</b>	0	12500	7000	12500	0
<b>Fuel Used (gal)</b>	1.74	5.37	588.75	5.37	3.17
<b>Total Fuel Used (gal)</b>	602				

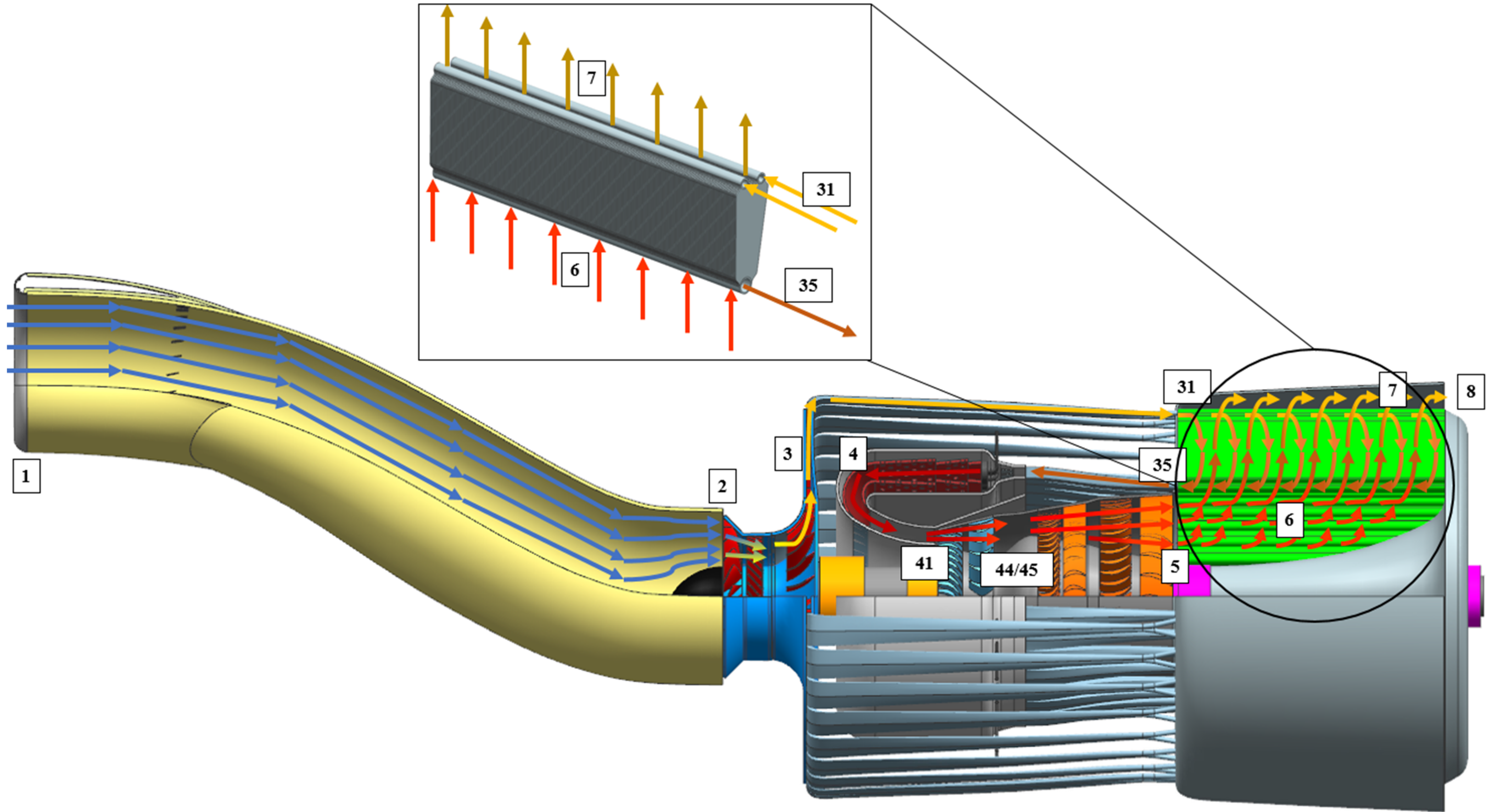
**Table 2.8: Baseline Engine Mission Profile**

	Takeoff and Climb	Cruise Out	Loiter	Cruise Return	Landing
<b>HP</b>	940	690	603	690	468
<b>Fuel Flow (lbs/s)</b>	0.14622	0.10931	0.09252	0.10931	-
<b>Time (hr)</b>	0.035	0.17	11.64	0.17	0.08
<b>Altitude (ft)</b>	0	12500	7000	12500	0
<b>Fuel Used (gal)</b>	2.72	9.77	993	9.77	2.07
<b>Total Fuel Used (gal)</b>	1017.33				

**Table 2.9: SR-1000BDE Comparison to Baseline Engine**

	TPE331-10	SR-1000BDE	Percent Difference
<b>Loiter Fuel Usage</b>	993 gal	588 gal	40.7% Fuel Savings
<b>Loiter Time</b>	11.64 hrs	20.28 hrs	74.2% Increase
<b>Power to Weight Ratio</b>	2.44 hp/lb	11.4 hp/lb	367% Increase
<b>Range</b>	2304 nmi	3946 nmi	71.1% Increase

3. Engine Flow Path



## 4 Detailed Component Design

### 4.1 Engine Subsonic Inlet

The SR-1000BDE uses a subsonic transitioning S-duct inlet to direct airflow to the compressor face. Figure 4.1 displays an isometric view of the inlet with respect to the entire engine, and Table 4.1 tabulates the salient inlet performance and geometric parameters.

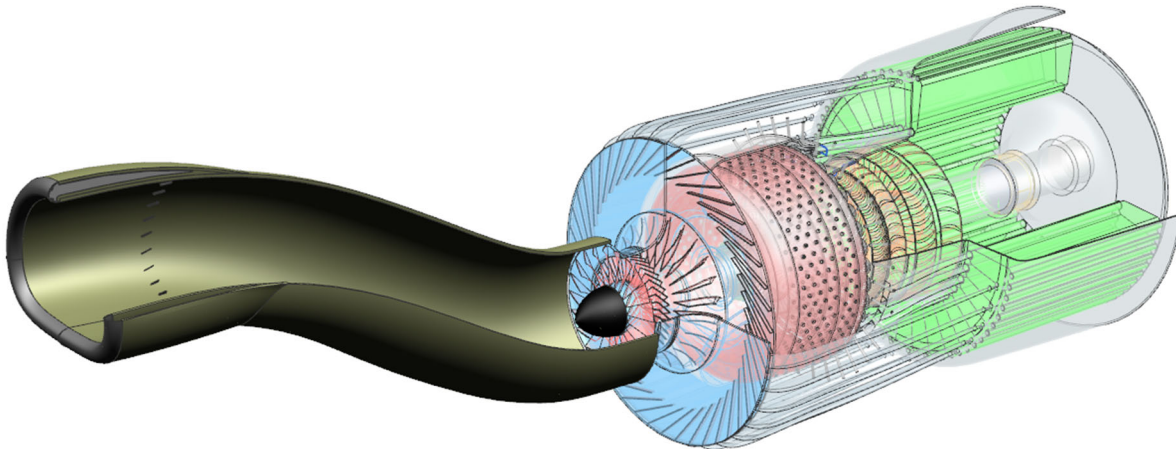


Figure 4.1: SR-1000BDE Subsonic Transitioning S-Duct Inlet

Table 4.1: Salient Characteristics of SR-1000BDE Inlet

Parameter	Value
Total Pressure Recovery, $\pi_d$	99.8 %
Length, $L$	59.5 cm
Offset Height, $h$	18 cm
Inlet Face Area, $A_1$	0.183 m <sup>2</sup>
Compressor Face Area, $A_2$	0.168 m <sup>2</sup>
Weight, $W_{inlet}$	1.48 kg

#### 4.1.1 Inlet Design Considerations

The major requirement for an inlet consists of providing flow to the compressor with low dynamic and steady-state distortion, while achieving high total pressure recovery across all flight phases. Additionally, a well-designed inlet should be light weight, have acoustic absorption, foreign object damage (FOD) tolerance, de-icing capabilities, and low installation drag. From the RFP, there are additional sizing constraints with an engine diameter less than 27 inches.

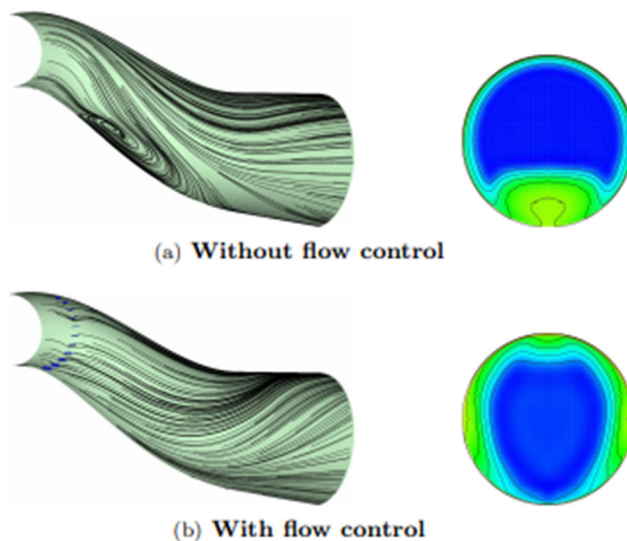
When delivering airflow with low distortion and high total pressure recovery, avoiding flow separation in the inlet is critical. To further prevent separation and improve flow quality at the compressor, an array of vortex generators is uniformly integrated into the duct walls to improve total pressure recovery while reducing flow distortion.

Unlike internal airflow, external flow produces installation drag which is directly related to the aircraft integration. To decrease drag, the engine is designed to be placed inside a UAV airframe. This requires the inlet to have a curved centerline exposing the inlet to incoming airflow, which is accomplished using an S-duct. Additionally, the S-duct is transitioning, allowing the inlet face to have geometry with better aerodynamic performance.

To limit overall engine weight, the inlet is designed to be lightweight by selecting a light material and limiting inlet size. For an S-duct inlet, size can be minimized by designing the duct with a large average wall angle and a small offset height.

**4.1.2 Inlet Auxiliary/Advanced Technologies**

Improvements in total pressure recovery and reductions in compressor face distortion, as previously discussed, have been achieved using vortex generators. Several computational and experimental studies have been conducted validating the benefits vortex generators have on flow quality through

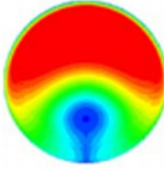
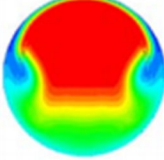


**Figure 4.2: Effect of Vortex Generators on Stall Mitigation [12]**

an S-duct inlet. Figure 4.2 displays streamlines and aerodynamic interface plane (AIP) pressure recovery contours obtained from a numerical simulation conducted by the Swedish Defense Research Agency. The plots illustrate the impact vortex

generator flow control has on the distribution of total pressure recovery at the AIP, as well as the prevention of flow separation. Table 4.2 presents computational results from NASA's Glenn Research Center. The data shows the beneficial impacts of vortex generators on the total pressure recovery and average

**Table 4.2: Diffuser Flow Quality Improvements Due to Vortex Generators [11]**

	Total Pressure Contour at AIP	PR	DPCP
<b>Baseline without VG's</b>		0.9561	0.0596
<b>Baseline with VG's</b>		0.9617 (+1.2%)	0.0286 (-56.5%)

SAE circumferential distortion (DPCP) at the AIP. The design, number, and location of the vortex generators in the SR-1000BDE inlet will be discussed in a later section.

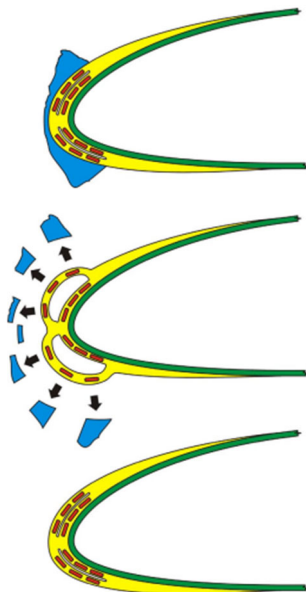


**Figure 4.3: Electro-Impulse De-Icing Operation [15]**

De-icing of the inlet lip is made possible by including an (EIDI) system. An EIDI system consists of spirally wound, flattened coils made from ribbon wire. The coils are rigidly supported inside the lip skin, separated by a gap of about 2.5 mm. During operation, an electric current pulse generated from a capacitor is transmitted through the coils. This current produces a magnetic field in the coils, which simultaneously induces an eddy current in the metallic lip skin. The two currents' fields repel each other, causing a low-displacement, high-acceleration jolt of the skin attached to the coils [14]. The corresponding jolt shatters the ice, breaking its bond with the lip skin. This de-icing process is illustrated in Figure 4.3.

An EIDI system is valuable due to its substantially lower energy requirements compared to other de-icing strategies and requires no external additions to the nacelle skin. In a joint study conducted by the U.S. Department of Transportation and the FAA Technical Center, theoretical energy requirements were compared between thermal de-icing/anti-icing methods and an EIDI system. The comparison is tabulated in Table 4.3. It is important to note that the values presented for

thermal methods do not account for heat losses in the thermal systems. Furthermore, because an EIDI system utilizes electromechanical devices, the inlet requires no bleed air from the compressor for de-icing, which would be

detrimental to cycle efficiency. Instead, the electromechanical devices (i.e., coils) are fed with high impulse currents by an impulse generator. Such an electrical set-up is illustrated by the schematic in Figure 4.4.

EIDI systems have been studied, developed, and tested at various institutions, such as: NASA’s Glenn Research Center, the Canadian National Research Council, Wichita State University, and Rolls-Royce [14]. The

company Innovative Dynamics, Inc. designs and manufactures an EIDI system that is certified by the FAA to operate on the Raytheon Premier I business jet [17]. Therefore, an EIDI system implemented on the SR-1000BDE inlet meets the TRL requirement for 2025 outlined by the RFP.

**4.1.3 Inlet Sizing and External Geometry**

Following strategies and guidelines from Farokhi [9], the subsonic transitioning S-duct inlet was sized accordingly. The first step involved calculating streamtube capture area for each flight phase. Streamtube capture area is a function of the flight Mach number, total temperature and total pressure, and inlet mass flow rate, as shown in Eq. 1.

$$\dot{m}_0 = \sqrt{\frac{\gamma}{R}} \frac{p_{t0}}{\sqrt{T_{t0}}} A_0 M_0 \left( \frac{1}{1 + \frac{\gamma - 1}{2} M_0^2} \right)^{\frac{\gamma + 1}{2(\gamma - 1)}} \tag{Eq. 1}$$

**Table 4.3: EIDI Energy Requirement Comparison with Thermal Strategies [14]**

De-Icing/Anti-Icing Strategy	Energy Required (W-hr/kg)
Evaporate Water	651.1
Melt Ice	93.8
Remove Ice with EIDI	0.7

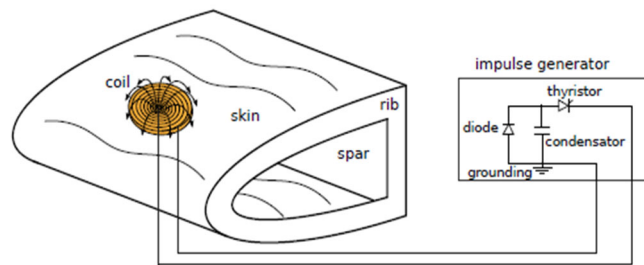


**Figure 4.4: Electrical Connection Diagram of EIDI System [14]**

For subsonic applications, the inlet highlight area is typically designed so that the capture streamtube itself acts like a diffuser. However, because the maximum flight Mach number is 0.35, and the compressor face requires a Mach number of 0.5, external diffusion via the capture streamtube is unnecessary. Therefore, the driving parameter for highlight area sizing was chosen to be spillage drag. Spillage drag, which is approximated by Eq. 2, is defined as the difference between inlet additive drag and lip thrust. The term  $K$  is a correction factor that multiplies the theoretical spillage drag. This correction factor typically ranges between 0.4-0.7, and is determined experimentally [20]. The correction factor was chosen to be the mean of the range, 0.55. Given the flow Mach numbers across two stations, the area ratio between the two stations could be calculated isentropically using Eq. 3.

$$D_{spillage} = F_{lip} - D_{add} \approx K(\dot{m}_1[V_1 - V_0] + A_1[P_1 - P_0]) \quad \text{Eq. 2}$$

$$\frac{A_0}{A_1} = \frac{M_1}{M_0} \left[ \frac{1 + \frac{\gamma - 1}{2} M_0^2}{1 + \frac{\gamma - 1}{2} M_1^2} \right]^{\frac{\gamma + 1}{2(\gamma - 1)}} \quad \text{Eq. 3}$$

Using the above equations, spillage drag and inlet highlight area were plotted with respect to inlet face Mach numbers in Figure 4.5 for cruise and loiter flight conditions. The goal of these calculations was to determine an optimal highlight area yielding the minimum spillage drag between the two flight phases.

As seen from the figure, the lowest spillage drag between cruise and loiter occurs with a highlight area of  $0.0183 \text{ m}^2$ , corresponding to an  $M_1$  at the inlet highlight of 0.322. With the highlight sized, the inlet throat area could

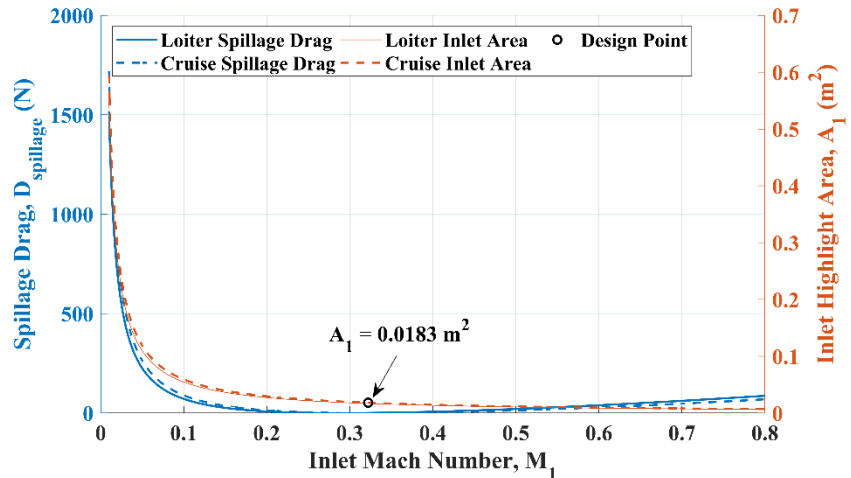
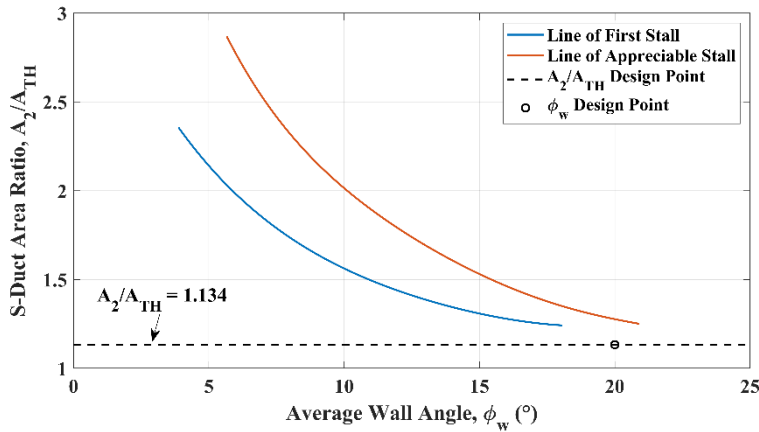


Figure 4.5: Spillage Drag and Highlight Area Calculations for Loiter and Cruise Flight Conditions



**Figure 4.6: Average Wall Angle Sizing with Respect to Geometric Stall Data [19]**

be sized using the isentropic relation from Eq. 3. Due to the throat curvature effect, the flow from the highlight to throat locally accelerates a greater amount near the duct walls. Figure 4.6 illustrates the throat curvature effect. Because of this phenomenon, the average throat Mach number must be

less than or equal to 0.75 to avoid locally choked flow [18]. An average throat Mach number of 0.4 was selected, ensuring the flow remains subsonic across its entire profile. This Mach number corresponds to a throat area,  $A_{TH}$  of  $0.0148 \text{ m}^2$ . Next, the length, face offset height, and average wall angle of the inlet were sized. Reference 18 was used extensively in the design of the S-duct diffuser. From the cycle analysis, the compressor face diameter was established as 0.1462 m, corresponding to an  $A_2$  of  $0.0168 \text{ m}^2$ . This increase in area from the inlet throat to compressor face results in an adverse pressure gradient downstream the throat.

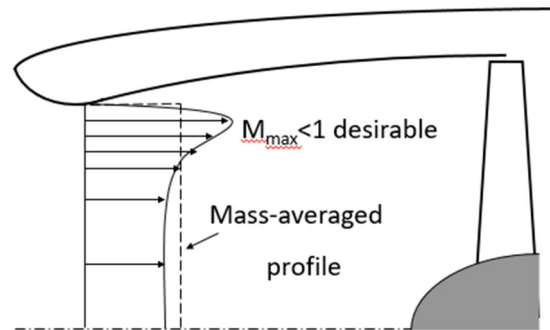


**Figure 4.7: Throat Curvature Effect [18]**

Because of this pressure gradient, it was essential that the S-duct average wall angle,  $\phi_w$ , not be so high that flow separation occurs. Therefore, geometric stall margins produced by Lee and Boedicker were used for selecting an appropriate  $\phi_w$ . The stall margin data was reproduced on a graph in MATLAB, as shown in Figure 4.6. This figure illustrates the effect of duct area ratio ( $A_2/A_{TH}$ ) and average wall angle  $\phi_w$  on stall tendencies within the duct. Because of the low duct area ratio of 13.4%, an average wall angle of  $20^\circ$  could be employed while maintaining separation-free diffusion.

With  $\phi_w$  acquired, the duct offset,  $h$ , and length,  $L$ , were calculated. Eq. 4 [19] relates  $h$  and  $L$  with the average wall angle. Using this equation, the graph in Figure 4.8 was produced.

$$\phi_w = \tan^{-1} \left( \frac{h}{L} + \left( 1 - \frac{1}{\sqrt{1/(A_2/A_{TH})}} \right) / \left( 2 - \frac{L}{D_2} \right) \right) \quad \text{Eq. 4}$$

As seen in the figure, the magnitude of  $\phi_w$  has a significant impact on the overall size of the S-duct. The larger the average wall angle, the smaller the duct length for a given offset height. It was chosen to set the offset height,  $h$ , to 18 cm. Based on the graph, this corresponds to an inlet length,  $L$ , of 55 cm.

With the length and face offset height determined, geometric functions for calculating centerline and area distributions of the S-duct were employed. The centerline shape

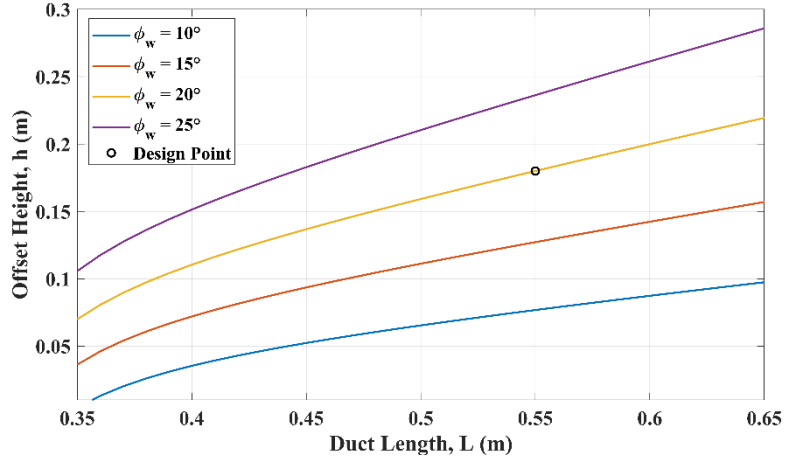
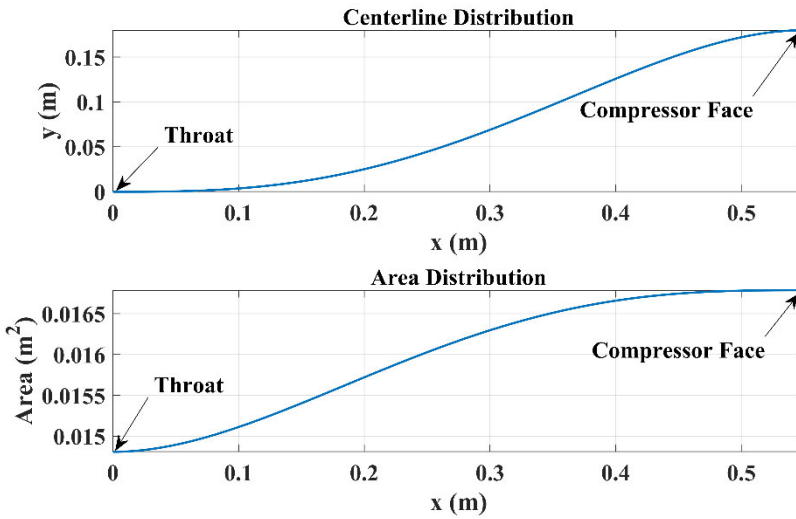


Figure 4.8: Duct Length Sizing

of the S-duct is important to consider because it dictates the transverse pressure gradient (and thereby the secondary flow). Area distribution is considered in the S-duct design due to its impact on the streamwise pressure gradient imposed upon the flow (and thereby the flow separation). According to Lee and Boedicker, the best diffuser performance is achieved by a combination of slow turning and high diffusion rate at the inlet face. Eq. 5 and Eq. 6 geometrically map out the centerline and area distributions that correspond to the best diffuser performance. Both distributions are plotted in Figure 4.9.

$$y(x) = h \left[ -3 \left( \frac{x}{L} \right)^4 + 4 \left( \frac{x}{L} \right)^3 \right] \quad \text{Eq. 5}$$

$$A(x) = A_{TH} \left( \frac{A_2}{A_{TH}} - 1 \right) \left[ 3 \left( \frac{x}{L} \right)^4 - 8 \left( \frac{x}{L} \right)^3 + 6 \left( \frac{x}{L} \right)^2 \right] + A_{TH} \quad \text{Eq. 6}$$



**Figure 4.9: S-Duct Centerline and Area Distributions**

centerline endpoints of 18 cm. The centerbody and duct transition design will briefly be detailed in the following section.

Summarizing the external geometry of the SR-1000BDE inlet, Figure 4.10 displays a side-view of the inlet with salient geometric parameters labelled. The total length of the inlet (including the centerbody) is 59.5 cm, and has an offset height between the

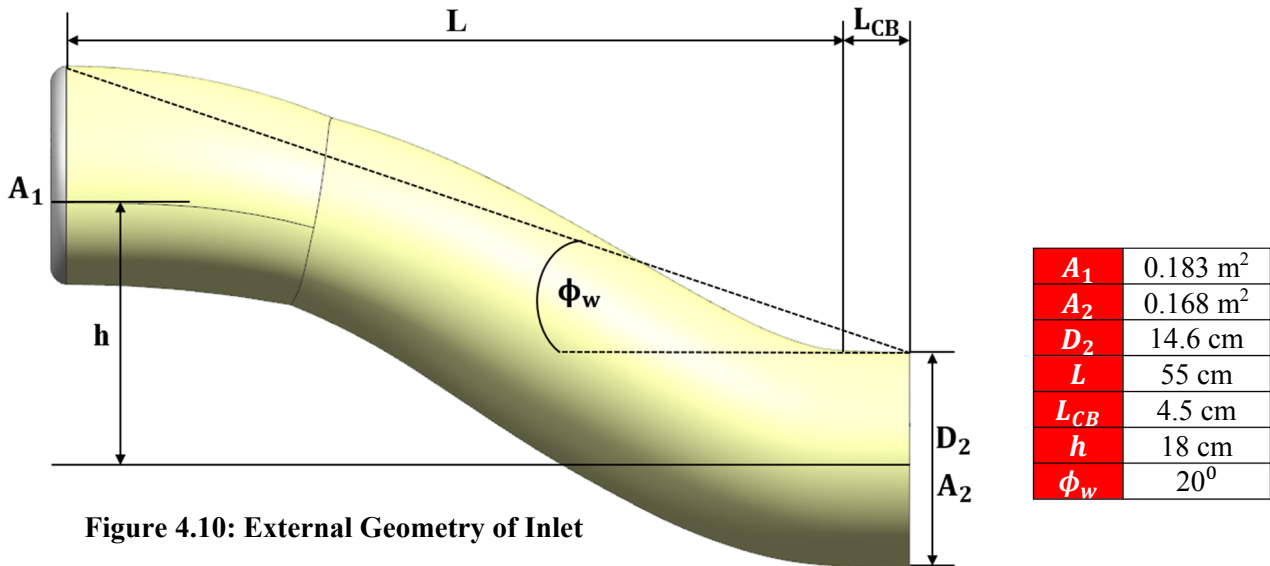


**Figure 4.10: External Geometry of Inlet**

#### 4.1.4 Inlet Internal Geometry

Focusing on the transitioning aspect of the SR-1000BDE inlet duct, Figure 4.11 displays a wireframe model of the inlet, showing the change in the cross-sectional shape from highlight to compressor face. The shape of the highlight cross-section was chosen by design to resemble the semi-super-elliptic cross-section of the General Atomics MQ-9 Reaper, shown in Figure 4.12. Several versions of the MQ-9 Reaper utilize the baseline TPE331-10 turboprop engine.

Since the highest rate of diffusion occurs near the inlet face, geometric stall margins with respect to inlet face aspect ratio needed to be addressed. Figure 4.13 shows the aspect ratio limits of the transitioning duct with respect to data provided by Abbott, Anderson, and Rice [22]. Although higher aspect ratios were considered, it was decided to design the highlight with a lower aspect ratio since no stealth requirements were outlined in the RFP. As Figure 4.13 shows, the transitioning inlet is well within the region of attached flow for its aspect ratio, length, and exit diameter.

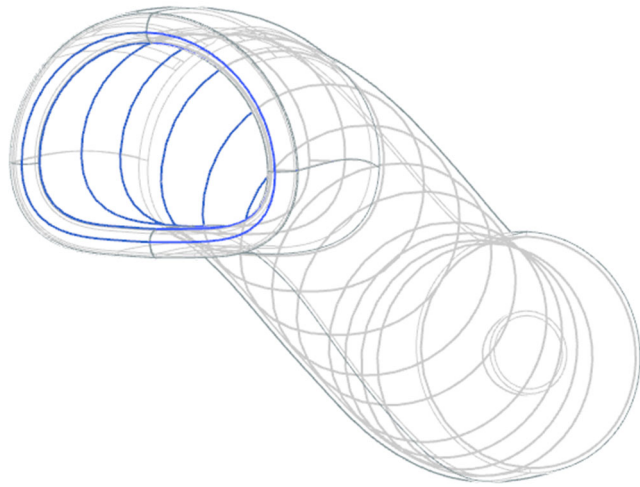


Figure 4.11: Wireframe Model of Transitioning S-Duct SR-1000BDE Inlet



Figure 4.12: Inlet Cross-Section of General Atomic MQ-9 Reaper [21]

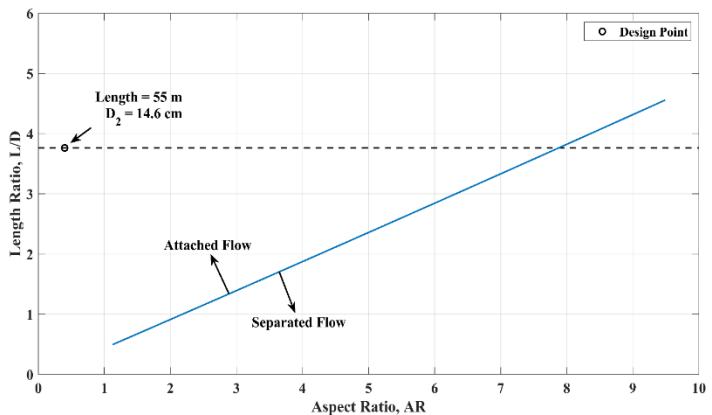
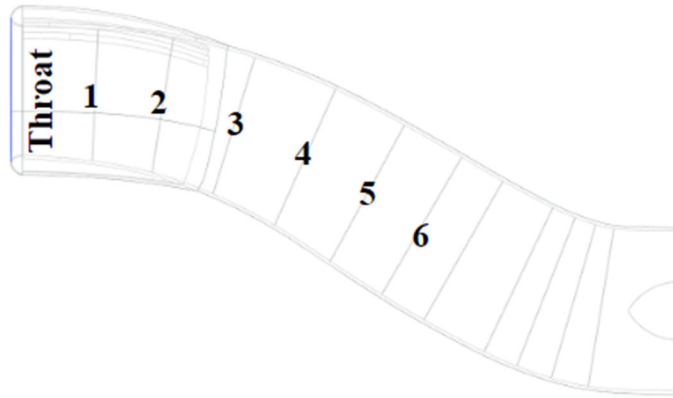


Figure 4.13: Inlet Face Aspect Ratio Limits with Respect to Geometric Stall Margin Data [22]

The inlet transitions from a semi-super-elliptic cross-section to a circular cross-section. As mentioned in the previous section, the area distribution from the inlet throat the compressor face was obtained. Using this area distribution, the inlet was cut up into slices with area values assigned



**Figure 4.14: Slices for Capturing Inlet Transition**

to each slice depending on its x-location with respect to the throat. Figure 4.14 illustrates and labels each slice. With the area known at each slice, the general shape of the semi-super-ellipse could be calculated using Eq. 7, Eq. 8, and Eq. 9, which are expressed in terms of Gamma functions. In these equations,  $a$  and  $b$  represent the semi-major and semi-minor axes, respectively. The parameter  $n$  determines the “sharpness” of the super-ellipse corners. The higher the value of  $n$ , the more pronounced the corner sharpness is.

$$S = S_{top} + S_{bottom} \quad \text{Eq. 7}$$

$$S_{top} = \frac{\sqrt{\pi} a_{top}^2 \left[ 4^{\left(1 - \frac{1}{n_{top}}\right)} \right] \Gamma\left(1 + \frac{1}{n_{top}}\right)}{2\Gamma\left(\frac{1}{2} + \frac{1}{n_{top}}\right)} \quad \text{Eq. 8}$$

$$S_{bottom} = \frac{\sqrt{\pi} a_{top} b_{bottom} \left[ 4^{\left(1 - \frac{1}{n_{bottom}}\right)} \right] \Gamma\left(1 + \frac{1}{n_{bottom}}\right)}{2\Gamma\left(\frac{1}{2} + \frac{1}{n_{bottom}}\right)} \quad \text{Eq. 9}$$

To generate the highlight shape, the cross-section was split into two semi-super-ellipses with different  $n$  values and semi-major axes. As the duct transitions, the semi-major axis of the bottom half increases closer and closer to equaling that of the top half. Simultaneously, the  $n$  value decreases towards 2. Doing so at each slice allows the cross-section to gradually transition from the semi-super-elliptic shape to a circular shape. Figure 4.15 displays the gradual transition from the throat cross-section down to the sixth slice. After slice six, the duct has fully transitioned into a circular cross-section.

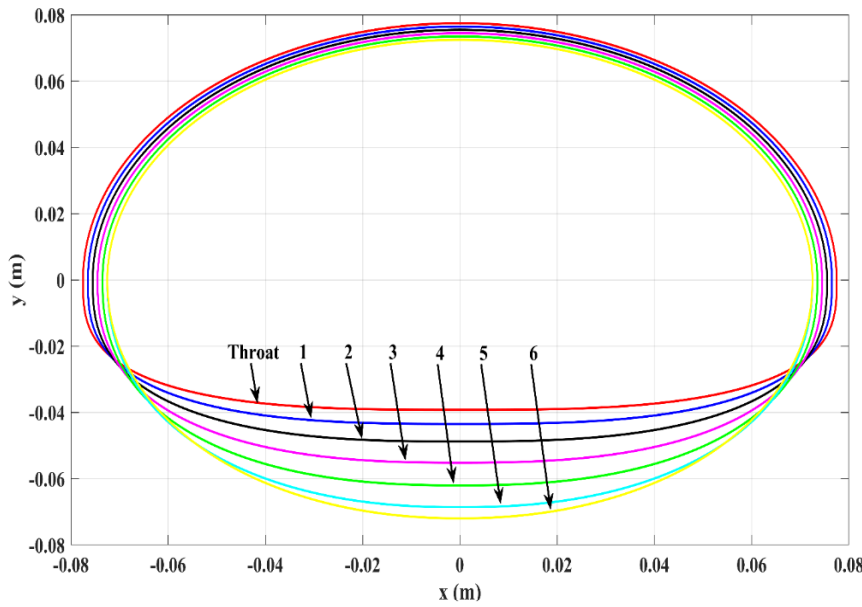


**Figure 4.15: Cross-Section Shape Transition from Inlet Throat to Slice 6**

Figure 4.16 summarizes the salient internal geometric parameters of the SR-1000BDE inlet. The centerbody was designed using standard ogive nose design principles. To match the hub diameter of the compressor, the centerbody was given a diameter of 5.2

cm. A standard NACA-1 was used for the nacelle external contour. The placement of the vortex generators relative to the throat was made at the location where maximum flow turning occurs. Design of the vortex generators is detailed in the following section.

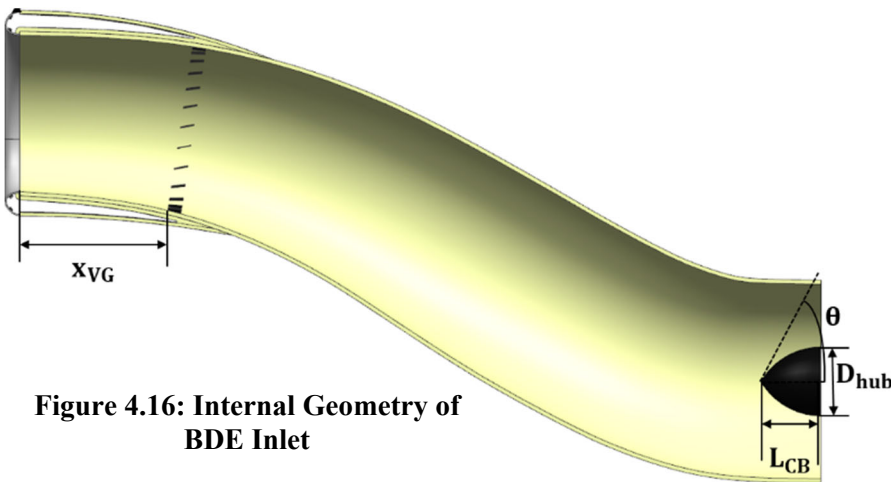


**Figure 4.16: Internal Geometry of BDE Inlet**

<b>Contraction Ratio</b>	1.24
<b>Fineness Ratio</b>	1.5
$x_{VG}$	12.2 cm
$L_{CB}$	4.5 cm
$D_{hub}$	5.2 cm
$\theta$	$60^\circ$

#### 4.1.5 Vortex Generator Design

Design of the vortex generators was done following a design optimization study conducted by the Swedish Defense Research Agency [12]. In the optimization study, the following parameters were varied across many numerical simulations:

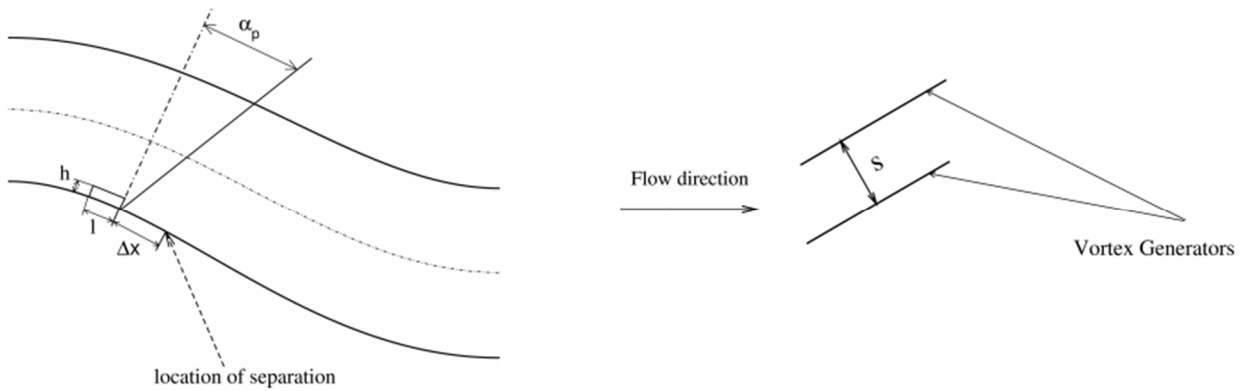
- vortex generator (VG) height relative to boundary layer thickness,  $h_{VG}/\delta$
- VG relative length,  $l/h_{VG}$
- VG spacing relative to length,  $s/l$
- relative distance of VG row from point of flow separation,  $\Delta x/h_{VG}$

Figure 4.17 provides a definition sketch of the geometric parameters mentioned above. From the simulations, the most optimized configuration yielded the highest increase in total pressure recovery and lowest amount of flow distortion. The geometric parameters for the most

**Table 4.4: Optimized Parameters Referenced for VG Design [12]**

Non-Dimensional Parameter	Optimized Value
$h_{VG}/\delta$	27.5%
$l/h_{VG}$	8.25
$s/l$	3.5
$\Delta x/h_{VG}$	6.75

optimized configuration have values listed in Table 4.4. Other than  $\Delta x/h_{VG}$ , the non-dimensional values were applied to the vortex generators of the SR-1000BDE inlet. The reason the value for  $\Delta x/h_{VG}$  wasn't used is because the inlet is designed with an average wall angle  $\phi_w$  of  $20^\circ$ , allowing for attached flow



**Figure 4.17: Definition Sketch of VG Geometry [12]**

throughout the entire inlet. Instead, the vortex generators were placed at the point where the highest wall angle occurs. At this point, turning of the flow is tight, resulting in higher flow diffusion.

Sizing the vortex generator height was done after approximating the local boundary thickness of the flow at the VG location. From the flat plate assumption in the Blasius solution, Eq. 10 was used to estimate the boundary layer thickness for the turbulent Reynolds number flow.

$$\delta \approx 0.37x_{VG}/Re_{x_{VG}}^{1/5} \quad \text{Eq. 10}$$

After estimating the local boundary layer thickness, the height, length, and spacing of the vortex generators were calculated using the optimized ratios listed in Table 4.4. The VG dimensions are labelled in Figure 4.18.

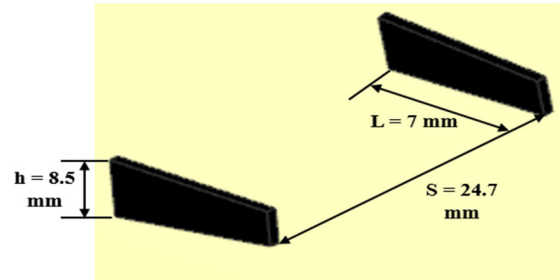


Figure 4.18: Vortex Generator

#### 4.1.6 Inlet FOD Tolerance



Figure 4.19: 3-D Printed Inlet Screen [23]

The inlet needed to be designed with the risk of foreign object damage taken into consideration. Birds, ice, hail, or various forms of debris could get sucked into the inlet and passed through the compressor, resulting in severe damage that could potentially destroy the entire engine. It was considered to include an inlet screen such as the additively manufactured screen (Figure 4.19) used on GE Aviation’s Catalyst engine to prevent relatively large foreign objects from being ingested by the compressor.

However, due to the added manufacturing costs/complexity, weight, total pressure losses, and de-icing complexity, it was decided to not include a screen with the inlet design. Since the SR-1000BDE is part of a hybrid propulsion architecture, complete FOD prevention for the turboshaft generator is not critical to the safety of the UAV. If an object is ingested, and the engine is destroyed, the electric motors can still operate and produce the required thrust to the UAV, assuming the on-board battery has enough power stored for landing.

Although an inlet screen was not included for the SR-1000BDE inlet design, the structural design of the inlet includes damage tolerance in the event of a bird strike to the lip. For the structural analysis, it was assumed the inlet lip is struck by a 0.12 kg Mourning dove [25] at cruise speed. According to the FAA, the Mourning dove is the most common species of bird struck by civil aircraft in the United States [24]. Such a bird strike has 778 J of kinetic energy at cruise velocity, corresponding to a point load of

approximately 1.37 kN. To analyze the stresses induced from the impact, the inlet skin structure was modelled as a tube with a point load applied to the tube edge perpendicular to its centerline. The point load is assumed to be purely axial, making buckling the failure mode for this analysis. Therefore, Euler’s critical load (shown in Eq. 11) was used to determine the maximum load the inlet could take without buckling. In the equation, KL represents effective length of the inlet, I is the second moment of area of a tube, and E is the elastic modulus of a Kevlar composite discussed in the next section.

$$P_{cr} = \frac{\pi^2 EI}{(KL)^2} \quad \text{Eq. 11}$$

Due to all the assumptions made for the structural analysis, a factor of safety of 10 was applied to the point load representing the bird strike. It was found that the inlet skin could have a thickness of 1 mm and achieve positive margins of safety with the bird strike scaled up by the safety factor of 10.

#### 4.1.7 Inlet Materials and Structure

The inlet structure is designed to be lightweight, have relatively simple manufacturing, and capable of meeting the FOD tolerances mentioned in the previous section. Material selection and structural design was done under technical consultations with Dr. Mark Ewing [27] and Dr. Ronald Barrett [26]. The materials selected for the inlet are listed in Table 4.5.

**Table 4.5: Inlet Material Properties [28] [29] [30]**

Material	Density (g/cc)	Tensile Strength / Compressive Strength	Attributes
<b>985 Epoxy Reinforced Kevlar 49 Fiber Laminate (50/50)</b>	1.35	427 MPa / 214 MPa	<ul style="list-style-type: none"> <li>• Very high specific strength (5x higher than steel)</li> <li>• Excellent impact absorption</li> <li>• Heat and fire resistant</li> </ul>
<b>High Density SF-0940 Polyimide Foam</b>	0.596	26.0 MPa / 41.4 MPa	<ul style="list-style-type: none"> <li>• High compressive strength</li> <li>• Excellent acoustic absorption</li> <li>• Excellent heat and fire resistance</li> </ul>
<b>2024 T3 Aluminum Sheet</b>	2.768	405 MPa	<ul style="list-style-type: none"> <li>• Good specific strength</li> <li>• Relatively low cost and simple manufacturing</li> </ul>

Table 4.5 provides density, strengths, and attributes for each of the three materials listed above. Majority of the inlet structure is composed of a monocoque skin made of reinforced Kevlar laminate. The lip takes on a semi-monocoque structure and is adhesively bonded onto the monocoque skin using a lap joint between the two structures. The lip contains aerospace-grade polyimide foam and is sheathed by an outer surface of 2024 T3 Aluminum plate. Figure 4.20 illustrates the structural layout of the inlet.

With the skin thickness determined by the structural analysis, volume estimates were calculated in Siemens NX. Using the density data of each material, the inlet has an approximate mass of 1.48 kg (3.26 lbf).

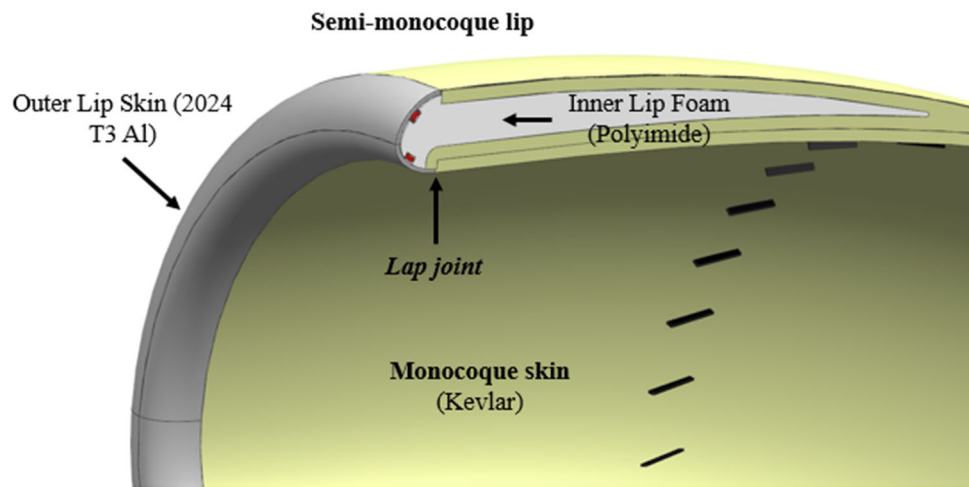


Figure 4.20: Inlet Structural Layout

## 4.2 Compressor

This section describes the design process and design decisions made for the SR-1000BDE compression system. It contains design choices, guidelines, assumptions, flow parameters, stage analysis, three stream surface analysis, structural analysis, and material selection. The SR-1000BDE compressor consists of a single axial stage followed by a single centrifugal stage. This decision was made to minimize the length of the compressor, and it is seen in industry in the FJ33 and FJ44 jet engines [31]. The two stages combine to have a pressure ratio of 9.83 as dictated by the optimized cycle.

The shaft rotational speed for the design is 62000 RPM with an annulus inlet area of 0.0126 m<sup>2</sup> and an exit area of 0.007 m<sup>2</sup>. The remaining compressor cycle parameters can be seen in Table 4.6.

#### 4.2.1 Compressor Inlet Conditions

The inlet total temperature, total pressure, and mass flow rate were supplied by the optimized cycle using GasTurb for analysis [5]. The flow at the compressor face was chosen to have an axial Mach number of 0.5 and no swirl. The static temperature

and static pressure were both found using isentropic assumptions. Having these values allowed for the calculation of the speed of sound, and the static density using the ideal gas law. The inlet flow parameters

**Table 4.7: Compressor Inlet Flow Parameters**

Parameter	Measurement
Total Pressure, $P_{t1}$	83.4 kPa
Total Temperature, $T_{t1}$	280 K
Mass Flow Rate,	1.90 kg/s
Axial Mach Number, $M_{z1}$	0.5
Static Temperature, $T_1$	266 K
Static Pressure, $P_1$	70.3 kPa
Speed of sound, $a_1$	327 m/s
Static Density, $\rho_1$	0.92 kg/m <sup>3</sup>

ratio will be explained in a later section. Having the tip radius then allowed for the calculation of hub

**Table 4.8: Compressor Inlet Geometric Parameters**

Parameter	Measurement
Annulus Area, $A_1$	0.013 m <sup>2</sup>
Hub-to-Tip Radius Ratio, $r_{-h1}/r_{t1}$	0.4
Tip Radius, $r_{t1}$	0.068 m
Hub Radius, $r_{h1}$	0.026 m
Pitchline Radius, $r_{-m1}$	0.047 m

**Table 4.6: Compressor Cycle Parameters**

Parameter	Value
Total Pressure Ratio, $\pi_c$	9.83
Total Temperature Ratio, $\tau_c$	2.08
Inlet Total Pressure, $P_{t1}$	83.4 kPa
Inlet Total Temperature, $T_{t1}$	280 K
Exit Total Pressure, $P_{t2}$	820 kPa
Exit Total Temperature, $T_{t2}$	580 K
Polytropic Efficiency, $e_c$	0.9
Shaft Rotational Speed, $\omega$	62000 RPM
Isentropic Efficiency, $\eta$	0.865
Inlet Hub Radius, $r_{h1}$	0.026 m
Inlet Tip Radius, $r_{t1}$	0.068 m
Exit Radius, $r_2$	0.160 m
Exit Area, $A_2$	0.007 m <sup>2</sup>

can be found compiled in Table 4.7.

Using the design axial Mach number, and speed of sound, the axial velocity was found to be 164 m/s. The axial velocity was then used to calculate the necessary inlet annulus area using continuity. The tip radius at the compressor entrance was found by choosing a hub to tip radius ratio of 0.4. The decision for hub to tip radius

radius using the hub to tip ratio, and the pitchline radius through the averaging of the tip and hub radii. The geometric characteristics of

the compressor entrance can be found in Table 4.8.

#### 4.2.2 Axial Compressor Design Guidelines

An analysis was done for the axial compressor stage, and the centrifugal compressor stage separately. Following the flow path, the first of the two stages analyzed was the axial stage. Using guidelines from Aircraft Propulsion [9], seen in Table 4.9, a set of initial design decisions for the axial stage were made.

As previously discussed, the flow entering the compressor was chosen to be swirl free at a Mach number of 0.5. At this point, the decision to set the shaft rotational speed to 62000 RPM was made. This decision was heavily influenced on optimizing the high-pressure turbine efficiency. With the chosen shaft rotational speed, it was necessary to choose a hub to tip radius ratio to achieve a large but practical single stage axial pressure ratio of less than 1.6 [32]. This resulted in the hub to tip radius ratio being chosen to be the previously mentioned 0.4. Due to the axial stage being followed by a centrifugal stage, the stator of the axial stage was chosen to remove only some of the swirl created by the rotor. The full effects of this choice will be explained during the centrifugal compressor design section.

**Table 4.9: Axial Compressor Parameters with Guidelines [9]**

Parameter	Range of Values	Typical Value
Flow Coefficient, $\phi$	$0.3 \leq \phi \leq 0.9$	0.6
D-Factor	$D \leq 0.6$	0.45
Axial Mach number, $M_z$	$0.3 \leq M_z \leq 0.6$	0.55
Tip Tangential Mach number, $M_T$	$1.0 \leq M_T \leq 1.5$	1.3
Degree of Reaction, $^\circ R$	$0.1 \leq R \leq 0.9$	0.5 (for $M < 1$ )
Reynold's number based on chord	$300,000 \leq Re_c$	$> 500,000$
Tip relative Mach number	$(M_{1r})_{tip} \leq 1.7$	1.3-1.5
Stage average solidity	$1.0 \leq \sigma \leq 2.0$	1.4
Stage average aspect ratio	$1.0 \leq AR \leq 4.0$	$< 2.0$
Polytropic efficiency	$0.85 \leq e_c \leq 0.92$	0.9
Hub rotational speed	$\omega_{r_h} \leq 380$ m/s	300 m/s
Tip rotational speed	$\omega_{r_t} \sim 450-550$ m/s	500 m/s
Loading Coefficient	$0.2 \leq \psi \leq 0.5$	0.35
DCA blade (range)	$0.8 \leq M \leq 1.2$	Same
NACA-65 series (range)	$M \leq 0.8$	Same
De Haller Criterion	$0.72 \leq W_2/W_{-1}$	0.75
Aspect ratio, compressor	$1 \leq AR \leq 4$	$\sim 2$

The axial rotor is chosen to have a degree of reaction of 0.7 to both maximize pressure ratio while also maintaining a diffusion factor of less than 0.6. In terms of blade design, the decision was made to have an aspect ratio of 2 and a pitchline solidity of 1.5. The solidity choice was based on wanting to minimize the number of blades while keeping of a blade tip solidity of about 1, following modern practice [32]. The aspect ratio was chosen following the typical value in the guidelines while also maintaining the tip solidity of 1 as previously mentioned. The choice to have a constant hub radius was made to support the transition from the axial compressor stage into the centrifugal compressor stage.

After setting the major design choices and assumptions, the axial stage analysis was done. The use of a rotor followed by a stator allows for the use of velocity triangles as defined in Figure 4.21. Using the definition sketch an in-depth design and analysis of the axial stage could be completed.

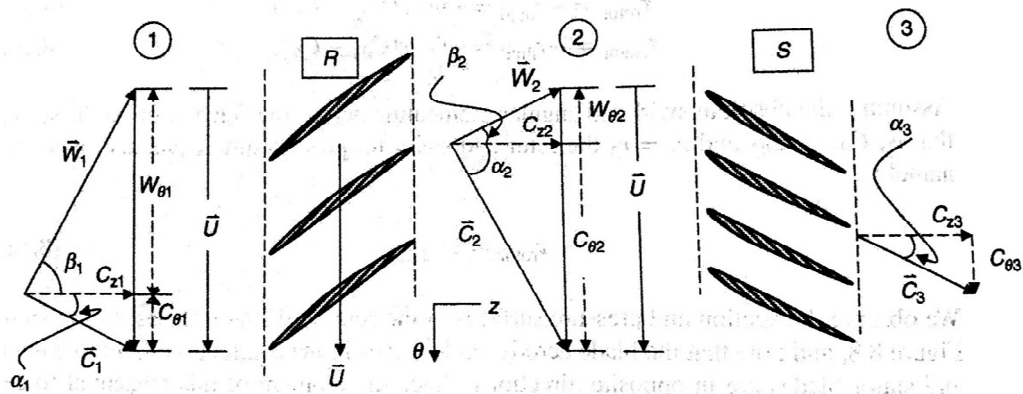


Figure 4.21: Velocity Triangle Definition Sketch [9]

#### 4.2.3 Compressor Pitchline Analysis

In a normal analysis, the compressor exit parameters would be the next step for calculations, however, due to having a mixed axial and centrifugal compressor that will not work. Instead a design for maximizing pressure ratio within a single axial stage was done, while sticking to the design choices listed earlier. The calculations begin with a complete pitchline analysis before looking at the effects of three-dimensional blade design.

To start, it was assumed that axial velocity stays at the constant 164 m/s calculated earlier. Then, using the shaft rotational speed and pitchline radius, the rotational velocity of the rotor was found. This allowed for the relative flow velocity to be calculated by utilizing velocity triangles, and in turn the relative Mach number. Due to assuming the flow entering swirl free, it is known that the absolute flow angle is zero at the entrance. However, the relative flow angle is not zero and can be found by using trigonometry with the now defined velocity triangle.

The flow characteristics after the rotor could then be analyzed. This began with the use of the previously discussed design choice for degree of reaction. Using that design choice, along with the rotational velocity, the rotor exit swirl velocity was found using Eq. 12. Using the now known swirl velocity, Euler's turbine equation can be used to calculate the total temperature after the rotor with Eq. 13.

$$C_{\theta 2,m} = 2U_m(1 - \sigma R) \quad \text{Eq. 12}$$

$$T_{t2,m} = T_{t1} \left( 1 + \frac{U_m C_{\theta 2,m}}{c_p T_{t1}} \right) \quad \text{Eq. 13}$$

The axial compressor pressure ratio was then found using temperature ratio, ratio of specific heats, and polytropic efficiency as shown in Eq. 14, and results in a pressure ratio of 1.59. This pressure ratio is accepted as about maximum practical modern practice [32]. Using the found pressure ratio, the total pressure after the rotor is found. This then allowed for a repeat of the process used to find all the compressor entrance parameters. The flow exits the rotor with swirl, which means the velocity triangle can be used to find the absolute and relative flow angles.

$$\pi_c = \tau_c^{\frac{\gamma e_c}{\gamma - 1}} \quad \text{Eq. 14}$$

As mentioned earlier, the choice was made to remove only some of the swirl produced by the rotor to help the centrifugal stage. This leads to needing a set of stators after the rotor to turn the flow. Due to stators being stationary, and only used for turning flow, the total temperature and total pressure do not change across the blades. Due to still having swirl, velocity triangles were used once again to find the absolute and relative flow characteristics. Using Euler's turbine equation again, the static temperature

after the stator is found, and in turn the speed of sound. The process continues in the same way as described earlier to get the static pressure, static density, and area after the stator.

The diffusion factor and blade loading were then checked to ensure they fall within the appropriate ranges. The diffusion factor is calculated using Eq. 15 for the rotor. The expected values must be less than 0.6 to avoid flow separation. To find the blade loading coefficient a relationship between swirl before and after the rotor is found as shown in Eq. 16.

$$D_r = 1 - \frac{W_2}{W_1} - \frac{C_{\theta 2}}{2\sigma_r W_1} \quad \text{Eq. 15}$$

$$\psi = \frac{C_{\theta 2}}{U_m} - \frac{C_{\theta 1}}{U_m} \quad \text{Eq. 16}$$

Using the design choice for the aspect ratio allowed for the estimation of how many blades will be needed for the rotor and stator. Using the already calculated radii to find the blade height and chosen aspect ratio the blade chord is found. A choice was made at this point to set the rotor and stator chords equal for simplicity. By rounding up the result of Eq. 17, the number of rotor blades is found. The number of stator blades is one less than twice the number of rotor blades. The larger number of stator blades is to help more effectively turn the flow. The choice to use one less than twice the number of rotor blades is made to reduce noise.

$$N_R = \frac{2\pi\sigma_r r_{m1}}{c_r} \quad \text{Eq. 17}$$

Using the blade chord lengths, the length of the axial portion of the compressor was then found. This was done through the averaging of flow angles and basic geometry. The spacing between the rotor and the stage was estimated as being one quarter of the average between the rotor and stator axial lengths. All that now remains to be calculated is how much power the axial compressor stage is going to require. This was done using another variation of Euler's turbine equation as shown in Eq. 18.

$$\dot{\phi} = \omega \dot{m} (C_{\theta 2} r_{m2} - C_{\theta 1} r_{m1}) \quad \text{Eq. 18}$$

#### 4.2.4 Three Stream Surface Analysis

A further analysis was then done in the form of a three-stream surface analysis to ensure necessary parameters are met. To perform three-dimensional blade design, a blade vortex design must be chosen to

help define how the flow will behave at the hub and tip of each blade. The chosen design type is a free-vortex design. This design is defined as having an equivalence between absolute swirl velocity and one over the streamline radius as seen in Eq. 19.

$$rC_\theta = \text{constant} \quad \text{Eq. 19}$$

The analysis for the hub and tip stream-lines were done in the same way as pitchline with the only difference being the free-vortex design defined swirl velocity instead of degree of reaction. With the additional analysis done, the velocity triangles were generated to better visual the flow behavior through the compressor. The triangles can be seen in Figure 4.22.

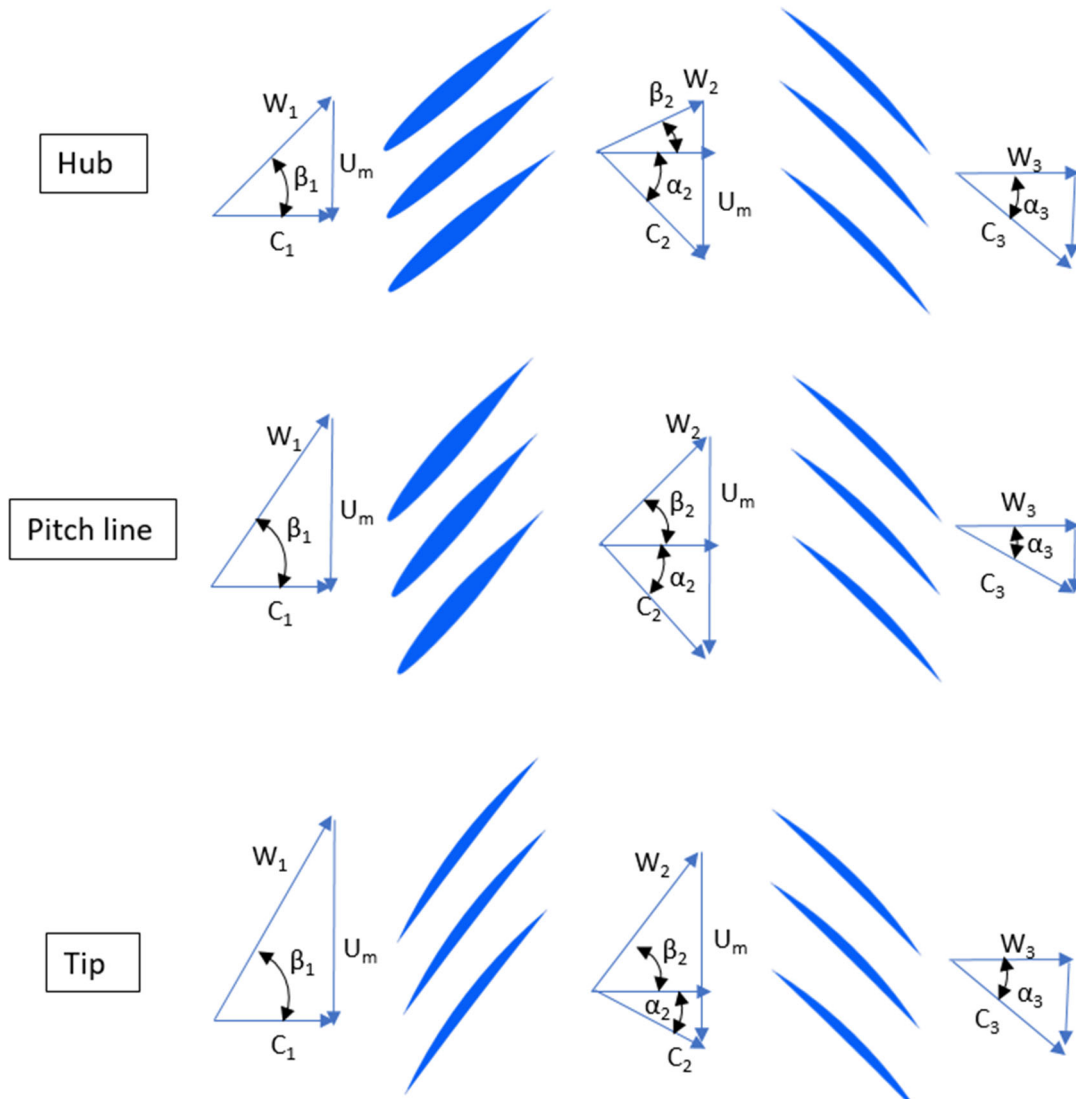


Figure 4.22: Three Stream Surface Velocity Triangles

### 4.2.5 Axial Compressor Blade Design

The next step was to perform a preliminary blade design. To do this, it was noted that the hub sees a maximum relative Mach number of less than 0.8, and the pitchline and tip both see a maximum relative Mach number greater than 0.8. This led to the decision to have a hub airfoil as a NACA 65-series, with a transition to a double-circular arc blade at the pitchline. The design choices made are supported by the design guidelines stated earlier. The last decision to be made was deciding on a suitable 65-series cascade geometry of a NACA 65-series cascade geometry of a NACA 65-(8)10. This was done using correlation data of Mellor found in Reference 9 seen in Figure 4.23.

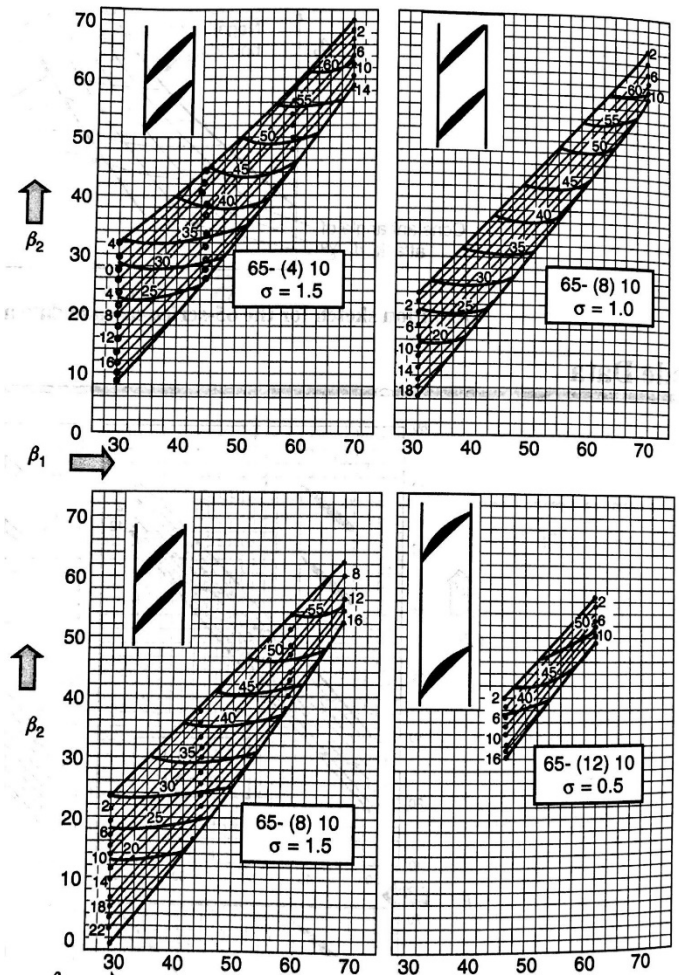


Figure 4.23: NACA-65 Series Cascade Data [10]

### 4.2.6 Axial Compressor Parameters

Data from the axial compressor analysis is compiled into a table of relevant parameters. This table can be seen in Table 4.10. Also, a preliminary conceptual CAD model of the axial compressor stage was created as seen in Figure 4.24.

Table 4.10: Axial Compressor Stage Parameters

Parameter	Rotor			Stator		
	Hub	Pitchline	Tip	Hub	Pitchline	Tip
<b>U (m/s)</b>	169	307	444	0	0	0
<b>r (m)</b>	0.026	0.047	0.068	0.026	0.039	0.052
<b>r<sub>h</sub>/r<sub>t</sub> (~)</b>	~	0.38	~	~	0.50	~
<b>C<sub>z</sub> (m/s)</b>	164	164	164	164	164	164
<b>M<sub>1</sub> (~)</b>	0.500	0.500	0.500	0.964	0.702	0.599
<b>M<sub>1r</sub> (~)</b>	0.719	1.062	1.448	0.587	0.583	0.971
<b>M<sub>2</sub> (~)</b>	0.964	0.702	0.599	0.569	0.669	0.821
<b>M<sub>2r</sub> (~)</b>	0.587	0.583	0.971	0.466	0.465	0.471
<b>M<sub>T</sub> (~)</b>	0.52	0.94	1.36	0	0	0
<b>T<sub>12</sub> (K)</b>	326	336	341	326	336	341
<b>P<sub>12</sub> (kPa)</b>	148	148	148	148	148	148
<b>α<sub>1</sub> (deg)</b>	0	0	0	59	48	40
<b>α<sub>2</sub> (deg)</b>	59	48	40	35	46	55
<b>β<sub>1</sub> (deg)</b>	46	62	70	33	37	62
<b>β<sub>2</sub> (deg)</b>	33	37	62	0	0	0
<b>°R (~)</b>	0.18	0.70	0.84	~	~	~
<b>σ (~)</b>	2.73	1.50	1.04	5.32	3.56	2.67
<b>D-Factor (~)</b>	0.38	0.59	0.41	0.55	0.42	0.31
<b>φ (~)</b>	0.97	0.53	0.37	~	~	~
<b>ψ (~)</b>	1.63	0.60	0.31	~	~	~
<b>c (m)</b>	0.0212	0.0212	0.0212	0.0212	0.0212	0.0212
<b>c<sub>z</sub> (m)</b>	0.0162	0.0129	0.0085	0.0162	0.0129	0.0085
<b>s (m)</b>	0.0078	0.0141	0.0205	0.0040	0.0060	0.0079
<b>N<sub>blades</sub> (~)</b>	~	21	~	~	41	~

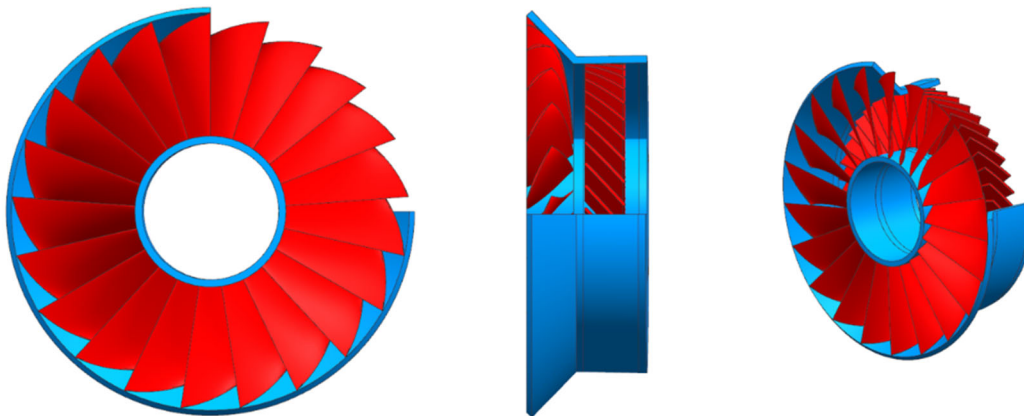


Figure 4.24: Axial Compressor Conceptual 3-View

#### 4.2.7 Centrifugal Compressor Design

The flow entering the centrifugal compressor is chosen to be swirl induced from that axial stage. This decision was made to minimize the power required to achieve a high pressure ratio. Having swirl in the flow from the axial stage also allows for the use of an inducer less centrifugal compressor. This reduces manufacturing complexity as well as reducing weight.

The impeller tip tangential Mach number was chosen to be 1.55. This decision was made to help achieve the high pressure ratio required for a two-stage compressor needing to produce a pressure ratio of 9.83. To also help meet the required pressure ratio, the final two design choices were having an impeller exit relative flow angle of 30 degrees.

The centrifugal stage of the compressor consists of an impeller followed by a vane diffuser. The choice of a constant hub radius allows for a smooth transition between the axial and radial compression stages. The vane diffuser is chosen to remove all swirl from the flow while also slowing down the flow to Mach 0.2. A basic velocity triangle definition sketch can be seen in Figure 4.25.

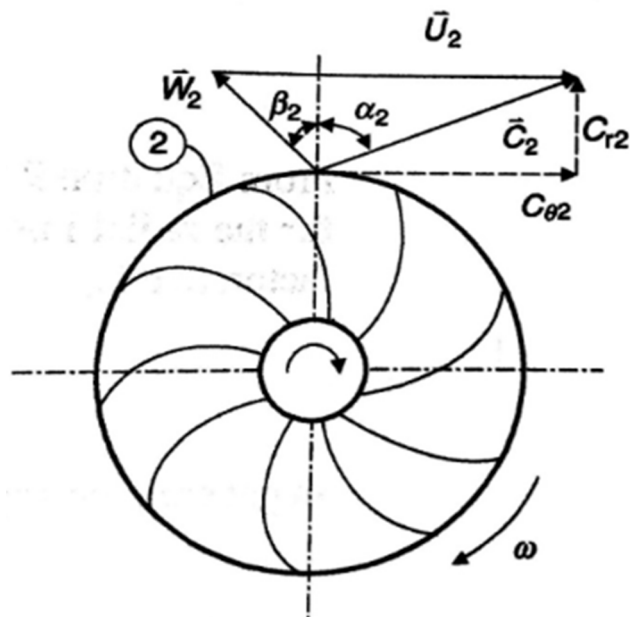


Figure 4.25: Impeller Exit Velocity Triangle Definition Sketch [9]

#### 4.2.8 Centrifugal Compressor Stage Analysis

The start of the stage analysis is setting the impeller entrance flow parameters equal to the stator exit flow parameters. This allowed for a quick geometric calculation of the eye radius for the impeller. Then, based on the design choice of 1.55 for tip tangential Mach number for the centrifugal stage, the impeller tip rotational velocity was found. Using the same relationship between shaft rotational speed, rotational velocity, and radius as earlier allowed for the solving of the impeller exit radius.

To find the exit flow parameters, the total temperature was calculated using Euler's turbine equation in the same way as after the rotor. Enough information was then known to use Eq. 20 to find the impeller pressure ratio. Using that, the total temperature after the impeller was found. Basic velocity triangles were utilized with the design choice of back sweep angle and slip angle, to find all the relevant velocities. This resulted in the calculation of static temperature, speed of sound, static pressure, and static density at the impeller exit. With all the previous calculations done, the impeller exit area is now solved for using continuity which in turn gives the blade height at the end of the impeller.

$$\pi_c = [1 + \eta_c(\tau_c - 1)]^{\frac{\gamma}{\gamma-1}} \quad \text{Eq. 20}$$

The power required for the centrifugal compressor was found using Euler's turbine equation in the same way the axial compressor required power was found. It was then necessary to find the number of blades required for the impeller design. This was done by first calculating the slip factor using the flow characteristics described in the velocity triangles. At the same time the blade loading coefficient was also calculated using basic velocity triangle characteristics. The number of blades was chosen to be 23 to achieve a slip factor of over 0.9, using the Stanitz-Ellis model seen in Eq. 21, while maintaining a low blade count to help minimize cost.

$$\varepsilon = 1 - \frac{1.98}{N_{blades}} \quad \text{Eq. 21}$$

Using basic thermodynamic relationships, the static pressures, static temperature, and static density were found at the diffuser exit. Continuity then is used to find the area at the end of the diffuser required to achieve the chosen exit velocity stated earlier. The velocity triangles created during the analysis can be seen in Figure 4.26.

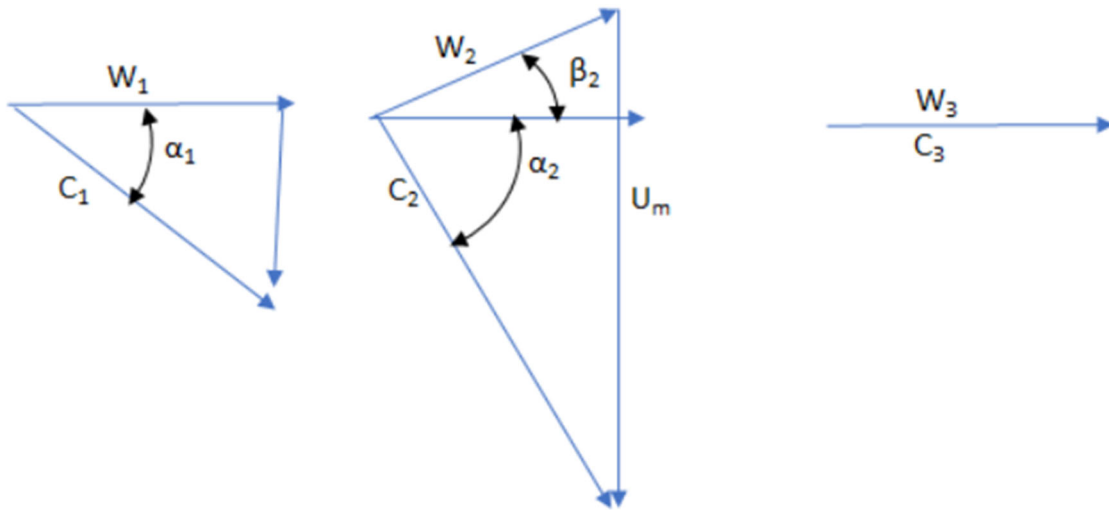


Figure 4.26: Centrifugal Compressor Velocity Triangles

#### 4.2.9 Centrifugal Compressor Parameters

The flow parameters at each station of the centrifugal compressor can be seen in Table 4.11. Following the table, a preliminary conceptual CAD model of the centrifugal compressor can be seen in Figure 4.27 as a three view.

Table 4.11: Centrifugal Compressor Parameters

Parameter	Station 1	Station 2	Station 3
U (m/s)	545	545	0
r (m)	0.052	0.084	0.160
$C_r$ (m/s)	0	164	86
$C_z$ (m/s)	164	0	0
M (~)	0.46	1.11	0.20
$M_T$ (~)	0.97	1.55	0
$T_t$ (K)	336	581	581
$P_t$ (kPa)	148	823	823
$\alpha$ (deg)	46	70	0
$\beta$ (deg)	0	30	0
$\epsilon$ (~)	~	0.912	~
$\psi$ (~)	~	0.924	~
b (m)	0.026	0.007	0.004
$N_{blades}$ (~)	~	23	45

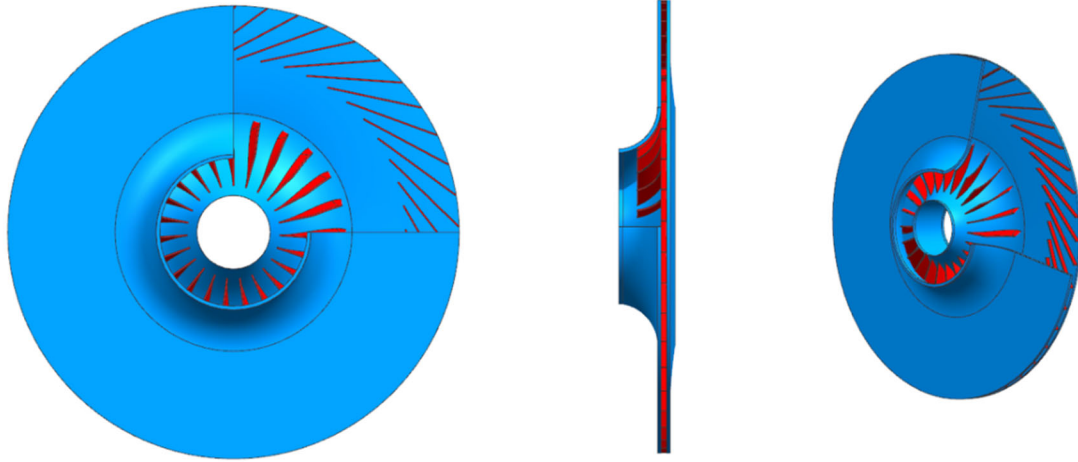


Figure 4.27: Centrifugal Compressor Conceptual 3-View

#### 4.2.10 Stall Margin Estimation

This was estimated using a method developed by Koch where the weighted diffusion length to staggered spacing ratio is compared to the effective pressure rise coefficient to estimate stall margin. To start the process of finding stall margin, Eq. 22 and Eq. 23 were used to find the diffusion length to staggered spacing ratio for the rotor and the stator. The weight diffusion length to staggered spacing ratio was then calculated with Eq. 24.

$$\varphi = \beta_i - \beta_{i+1} \quad \text{Eq. 22}$$

$$\left(\frac{L}{g_2}\right) = \sigma_m \frac{\frac{\varphi}{2}}{\sin\left(\frac{\varphi}{2}\right)} * \frac{A_{i-1}}{A_i} * \frac{h_i}{h_{i-1} \cos(\beta_i)} \quad \text{Eq. 23}$$

$$\left(\frac{L}{g_2}\right)_{stage} = \frac{\left(\frac{L}{g_2}\right)_{Rotor} q'_1 + \left(\frac{L}{g_2}\right)_{Stator} q_1}{q'_1 + q_1} \quad \text{Eq. 24}$$

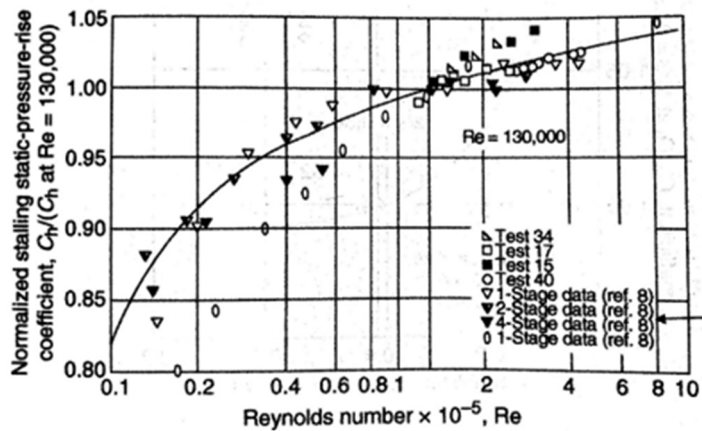
The next step was to calculate the stalling pressure rise coefficient using Eq. 25. However, the value needed was the effective stalling pressure rise coefficient. To get this value, a correction factor must be used from the graph shown in Figure 4.28. The correction factor is based on the Reynold's number across the blade chord length. Based on the chord length resulting from the chosen aspect ratio, a Reynolds

number of about 400,000 was achieved. Due to this, it is known that the correction factor is approximately 1.03. This resulted in the effective stalling pressure rise coefficient being calculated using Eq. 26.

$$C_h = \frac{c_p T_1 \left[ \left( \frac{p_{2,m}}{p_1} \right)^{\frac{\gamma-1}{\gamma}} - 1 \right]}{\frac{W_{1,m}^2 + C_2^2}{2}} \tag{Eq. 25}$$

$$C_{h_{eff}} = 1.02 C_h \frac{W_1^2 + C_2^2}{W_1^2 + F_{ef} C_2^2} \tag{Eq. 26}$$

With the two necessary values calculated, the stall margin was estimated for the pitchline of the compressor. This is done using the graph seen in Figure 4.28. The stall margin was estimated to be 30% and found acceptable for preliminary design. A goal of reducing it to a 15%



stall margin will be set for advanced design.

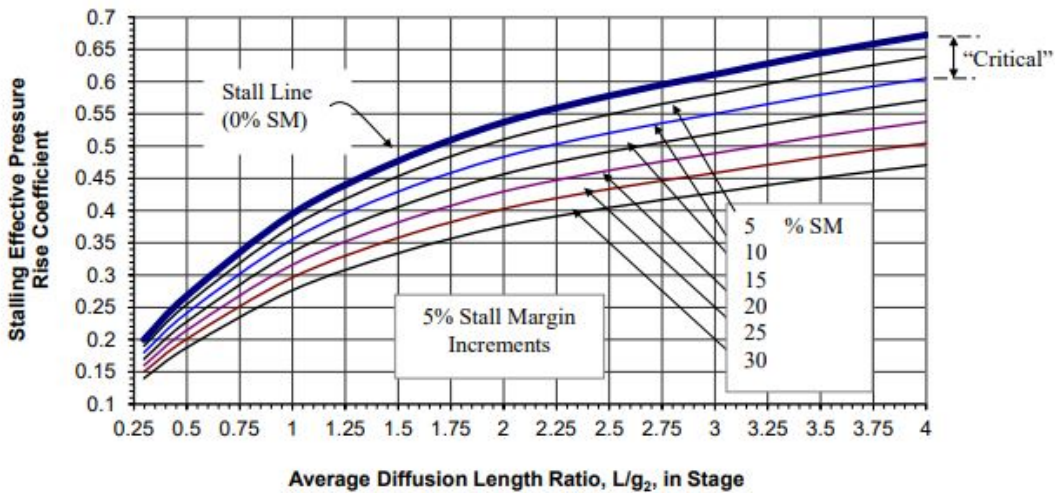
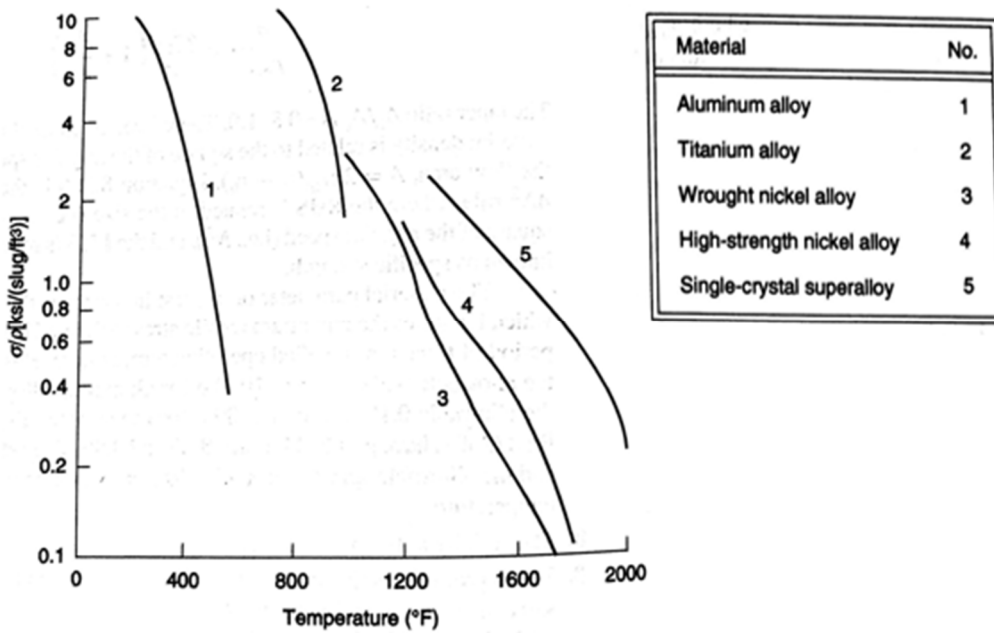


Figure 4.29: Stall Margin Chart [33]

**4.2.11 Compressor Material Selection and Stress Analysis**

To start the process of choosing a material a stress to density ratio had to be found. This was done using Eq. 27. Once that ratio was found for the rotor and impeller, Figure 4.30 was used to help determine what type of material would be best given a combination of the found ratio and max operating temperature.

$$\frac{\sigma}{\rho} = \frac{\omega^2 A}{4\pi} \left( 1 + \frac{A_t}{A_h} \right) \quad \text{Eq. 27}$$



**Figure 4.30: Allowable Stress vs. Temperature [9]**

From the graph, it was decided that a titanium alloy would be the best starting place for both the rotor and the impeller. When considering titanium alloys, it was decided to use titanium aluminide. This choice was based on the low relative density, high strength, high stiffness, and excellent oxidation resistance [34]. To ensure the material selection will not fail, the margins of safety were calculated. The results of the stress analysis are shown in Table 4.12.

**Table 4.12: Stress Analysis Results**

Parameter	<i>Axial</i>	<i>Centrifugal</i>
$\sigma$ (MPa)	221	382
Margin of Safety	3.4	1.6

#### 4.2.12 Three-View of the Compressor

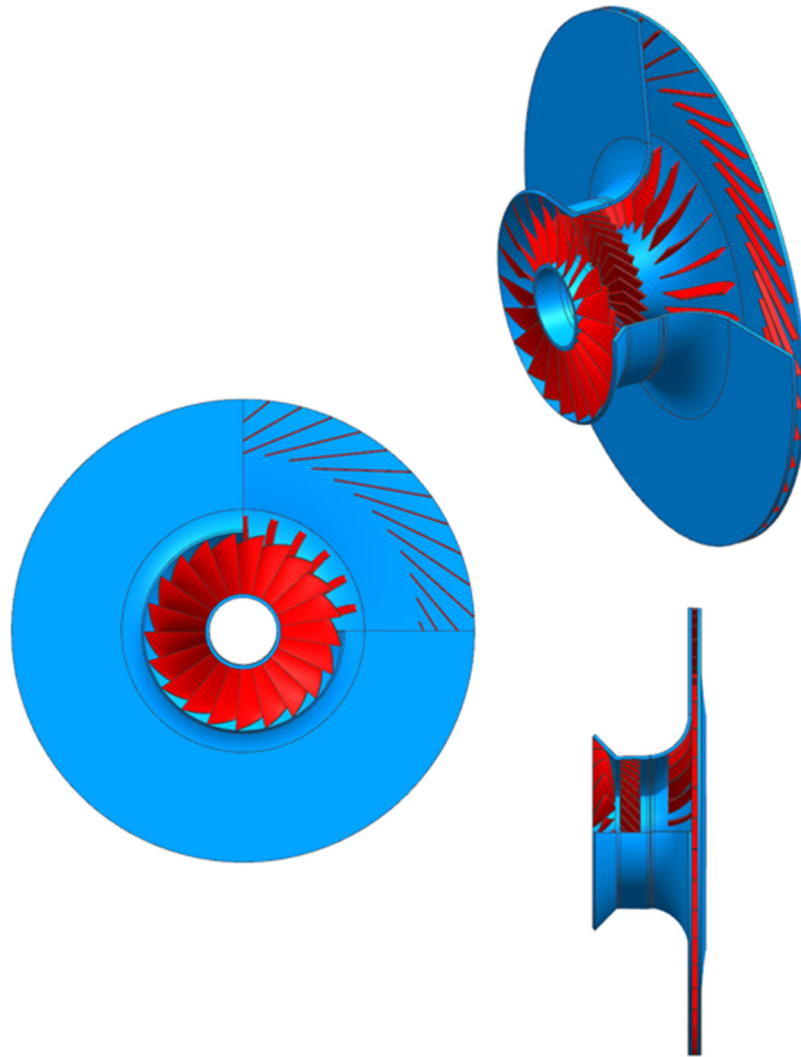


Figure 4.31: 3-View of the Compressor

### 4.3 Recuperator

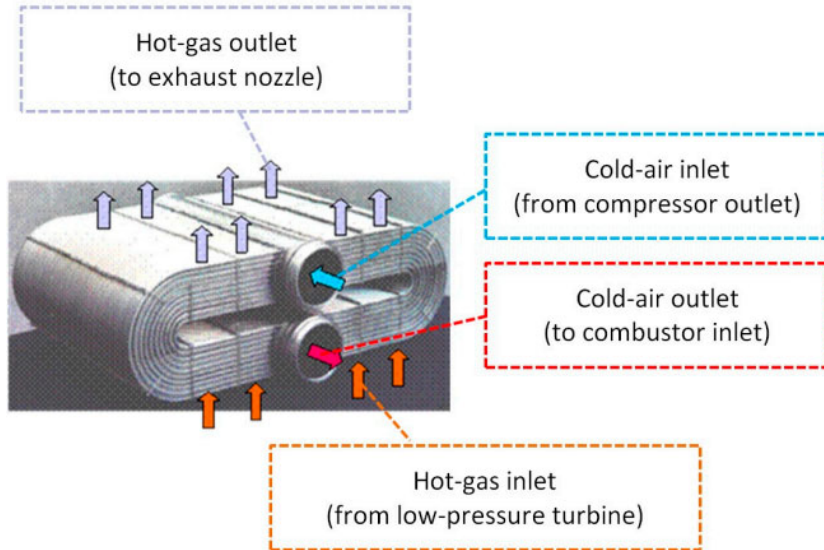
#### 4.3.1 Recuperator Design Philosophy

Following a fundamental thermodynamic design process laid out in Carozza [35] and sizing parameters from Vick and McDonald [36-38], the recuperator for the SR-1000BDE was designed. The SR-1000BDE engine is concentrated on being light weight and fuel efficient as shown from the major design drivers for the engine set forth by the AIAA RFP [1]:

- EIS of 2025

- Fuel savings of 25% to reach a 20+ hour loiter
- Required low acquisition cost for the designed engine

The SR-1000BDE recuperator could have various configurations, and to remain competitive for the service date of 2025, an annular recuperator matrix was chosen over a conical or classical elliptical tube matrix (shown in Figure 4.32). The recuperator will provide a temperature increase from the compressor



exit to the combustor inlet to decrease fuel usage at the expense of lowering the exhaust gas temperatures. The designed recuperator uses a state-of-the-art ceramic matrix to allow for a high heat transfer rate while maintaining a

**Figure 4.32: 4/3/4 elliptical tube MTU-heat exchanger matrix [39]**

resistance to the thermal stresses developed in the hot exhaust gases. Using Figure 4.33, from Reference 36, the chosen pressure ratio and the recuperated design allows for a theoretical thermal efficiency of 40%. This estimate is verified by the estimated thermal efficiency of the design at 41.7%, a vast improvement over the baseline's thermal efficiency of 25%. A recuperator's ability to regain thermal energy allows the engine to run at a lower overall cycle pressure ratio [35]. This design choice lowers the stresses encountered by the compressor and effectively shortens the length of the compressor.

### 4.3.2 Recuperator Thermodynamic Design

The recuperator of the SR-1000BDE is designed to facilitate heat transfer between the exhaust gases and the compressed air with minimal heat and pressure losses. A recuperator is characterized by the effectiveness of the heat transfer rate between the exhaust gases and the interim “cold” compressed air between the compressor and the combustor. The temperatures for the compressor exit and power turbine exit have previously been calculated in Sections 4.2 and 4.5, respectively, and are presented with other stage properties in Table 4.13. These form the thermodynamic base for the capability of the recuperator and simplify analysis by providing a basis to begin calculations.

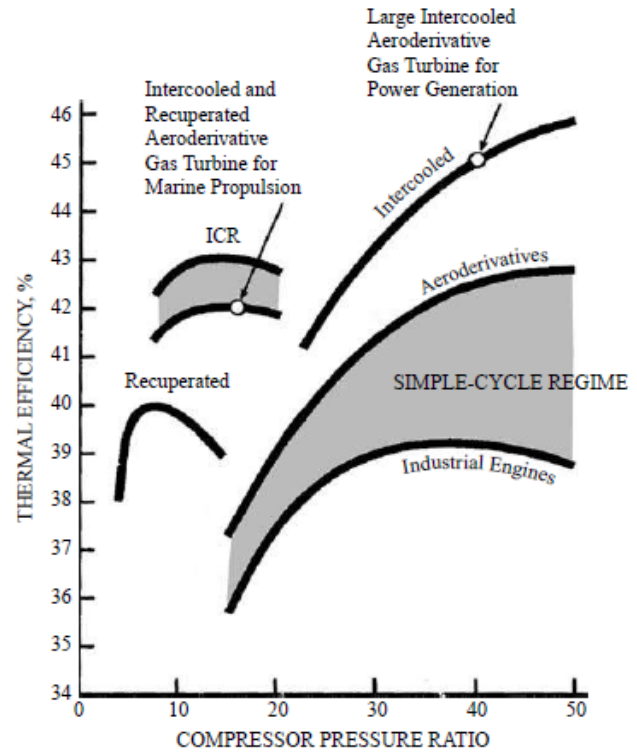


Figure 4.33: Comparative performance of power generation gas turbine variants [36]

Table 4.13: Initial values for the recuperator thermodynamic design

Name	Symbol	Value
Compressor Exit Massflow Rate	$\dot{m}_{c,i}$	1.89 kg/s
Power Turbine Exit Massflow Rate	$\dot{m}_{h,i}$	1.92 kg/s
Compressor Exit Ratio of Specific Heats	$c_{pc,i}$	1004 J/kg-K
Power Turbine Exit Ratio of Specific Heats	$c_{ph,i}$	1100 J/kg-K
Compressor Exit Total Temperature	$T_{tc,i}$	580 K
Power Turbine Exit Total Temperature	$T_{th,i}$	820 K

The defining characteristic of a recuperator, or any general heat exchanger, is the effectiveness. The recuperator heat transfer effectiveness is defined by the ratio between the actual heat transfer rate and the theoretical maximum. The definition of recuperator effectiveness is shown in Eq. 28.

$$\epsilon_r = \frac{\dot{q}_r}{\dot{q}_{r,max}} = \frac{\dot{m}_c c_{p,c} (T_{tc,o} - T_{tc,i})}{\dot{m}_h c_{p,h} (T_{th,i} - T_{tc,i})} \quad \text{Eq. 28}$$

By quantifying a value for recuperator effectiveness, the combustor inlet temperature can be determined. To find the 2025 design goal for recuperator effectiveness, several values found from industry and literature were plotted against time to extrapolate to the service date for the SR-1000BDE (Figure 4.34). As the trend is plateauing near 100%, a challenge was presented to attain as high an effectiveness as to lie within this trend. A recuperator effectiveness of 95% was chosen as the last known effectiveness of 92% can be achieved with a modest 3% increase to account for a 10-year gap where technology can advance.

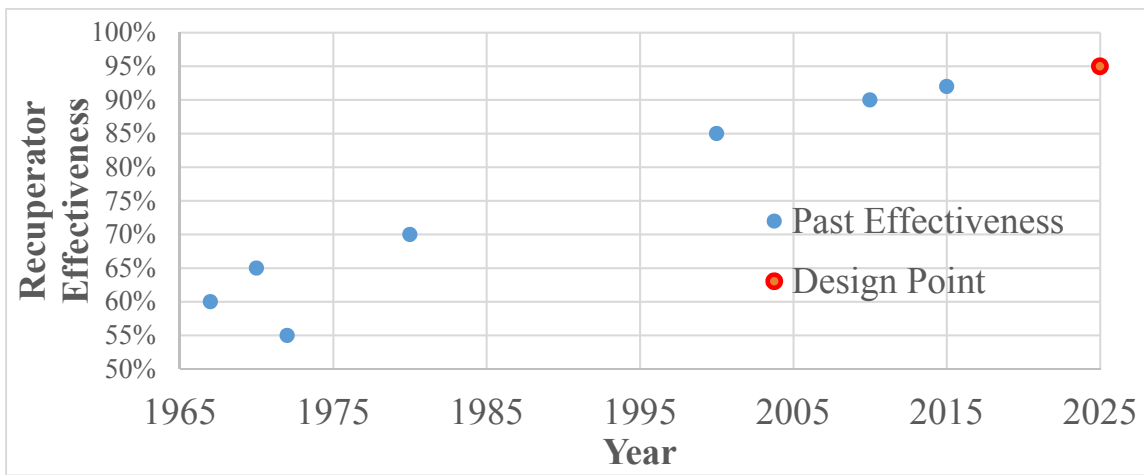


**Figure 4.34: Recuperator effectiveness over time [36,37,40]**

Using Eq. 28 and the chosen recuperator effectiveness, the resulting combustor entrance total temperature was calculated at 829 K. The resulting temperature of the turbine exhaust after the recuperator was then calculated using a simple energy balance across the recuperator [Eq. 29].

$$\epsilon_r Q_c = -Q_h \rightarrow \epsilon_r \dot{m}_c c_{p,c} (T_{tc,o} - T_{tc,i}) = -\dot{m}_h c_{p,h} (T_{th,o} - T_{th,i}) \rightarrow T_{th,o} = 584K \quad \text{Eq. 29}$$

Lastly, total pressure loss due to heat transfer needed to be considered. By treating the recuperator as a constant area duct and assuming zero friction, Rayleigh flow is assumed, and the associated theory was used to quantify the total pressure loss caused by heating. With a compressed stream temperature increase, the Mach number increases from 0.2 to 0.24 and induced a total pressure loss of 1.4%. While this decrease tightens the margin for pressure recovery in the combustor, the pressure loss and flow

acceleration during preheating are deemed acceptable because of the dramatic reduction in fuel burn required to reach the designed combustor exit temperature. Fuel flow would need to increase by 72% to accomplish the same temperature rise without a recuperator. The fuel savings are the primary reason the SR1000-BDE meets and exceeds the 20-hour loiter required by the RFP [1].

### 4.3.3 Recuperator Sizing and Configuration

To properly size the recuperator, the logarithmic mean temperature difference method was used [35]. Eq. 30 provides the general heat transfer rate in a recuperator where  $\Delta T_{lm}$  is the log-mean temperature (Eq. 31),  $V$  is the recuperator volume,  $\beta$  is the area density of the recuperator and  $U$  is the heat transfer coefficient. The temperature changes for the hot and cold side of the recuperator used in Eq. 31 represent the difference between the exit and inlet temperatures for each respective section of the recuperator.

$$Q = \Delta T_{lm} U \beta V = -472.5 \text{ kW} \quad \text{Eq. 30}$$

$$\Delta T_{lm} = \frac{(\Delta T_h - \Delta T_c)}{\ln \left| \frac{\Delta T_h}{\Delta T_c} \right|} \rightarrow \Delta T_{lm} = 9.66 \text{ K} \quad \text{Eq. 31}$$

Before solving for the matrix volume, the area density of the matrix and the heat transfer coefficient needed to be determined. Past area densities of a recuperator matrix have been estimated at  $6,600 \text{ m}^2/\text{m}^3$ , specifically for ceramic matrices (the choice of which is talked about in following sections) [41,42]. Assuming a technological increase in area density of ceramic recuperator's, the value used for the designed engine was  $8,000 \text{ m}^2/\text{m}^3$ . By using state-of-the-art mullite ceramics as the matrix material, the overall heat transfer coefficient for the recuperator was adjusted to  $400 \text{ W}/\text{m}^2\text{K}$  to accommodate for future advances [43]. Using these values, summarized in Table 4.14, a matrix volume of  $0.013 \text{ m}^3$  was found.

**Table 4.14: Values used for matrix volume estimation**

Symbol	Value	Reference
$Q$	-472.5 kW	Eq. 30
$\Delta T_{lm}$	9.66 K	, [35]
$U$	400 W/m <sup>2</sup> K	[45]
$\beta$	8,000 m <sup>2</sup> /m <sup>3</sup>	[43,44]
$V$	0.013 m <sup>3</sup>	Eq. 30

With the volume of the recuperator calculated, the matrix material needed a configuration to fit within the designed engine. Most historical metal recuperators use a shell and tube heat exchanger, which would be too large for this application, or a “block” plate recuperator that does not integrate well with the design of a gas turbine engine. Using Reference 36 and several modern recuperated engines, a radial design was chosen for the recuperator (Figure 4.36). This allows for several individual sections to be configured radially around the

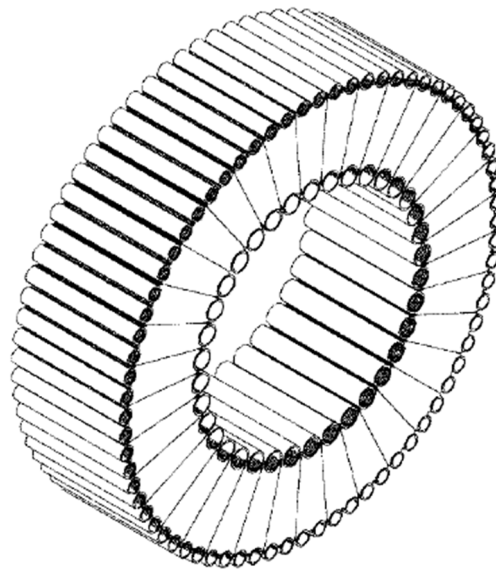


Figure 4.36: Radial recuperator [36]

engine for easy inspection and replacement. Each section of the radial recuperator consist of several hundred wafers: channel wafers and base wafers. Base wafers are exposed to the exhaust gases, allowing heat transfer, while the microchannel wafers [44] are placed between base wafers to allow for the compressed air to be guided from the inlet to the exit of the recuperator. Using basic design philosophy from Reference 36, the recuperator (Figure 4.35) was representatively modeled.

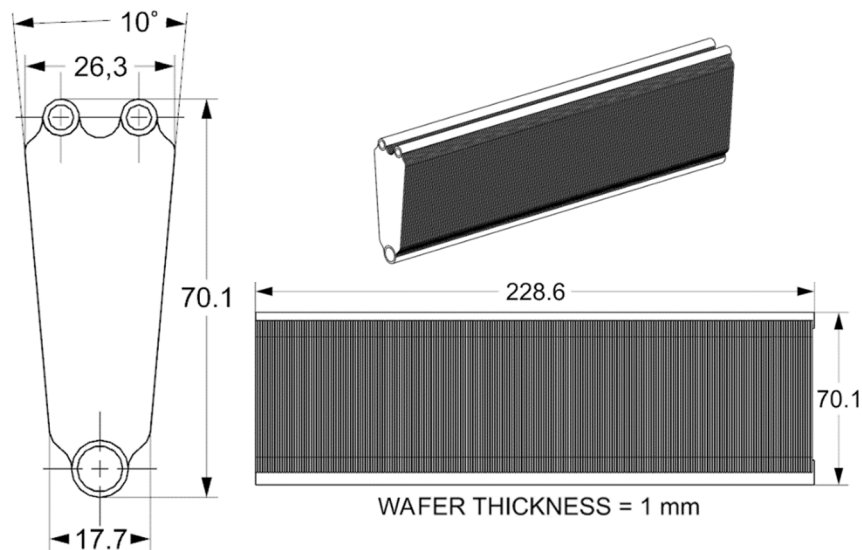
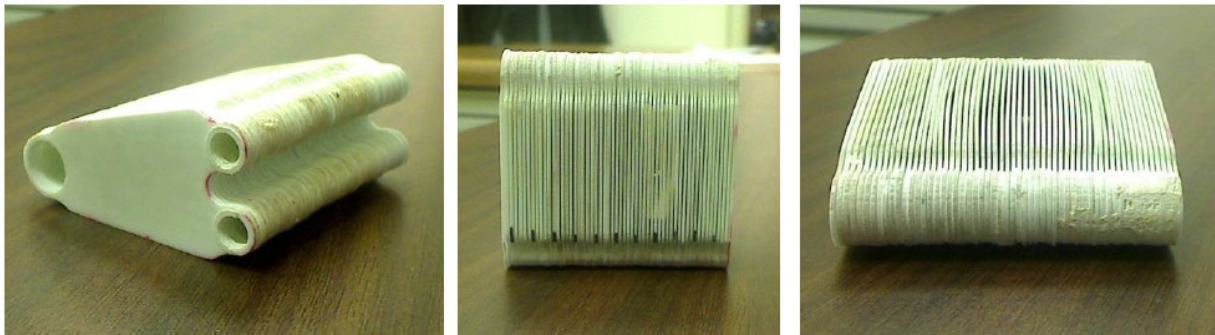


Figure 4.35: Designed recuperator dimensions (not to scale)

#### 4.3.4 Matrix Material Selection

Following References 35 and 45, the chosen material for the recuperator was mullite ceramic due to high temperature corrosion resistance, high thermal conductivity, durability and strength [36]. The specific design to be used is a ceramic microchannel recuperator fabricated using laminate laser-cut tape cast sheets [45]. Using data from 2005, the mullite and silicon carbon ceramics have a maximum stress and strength of 512 MPa and 745 MPa, respectively. Capable of achieving 92% effectiveness, Wilson et. al. [45] could achieve minimal pressure losses while producing turbine exit temperatures of  $1170^{\circ}\text{C}$ , well above the designed value for the SR-1000BDE. Ceramic was chosen over typical metal recuperators as the latter tends to introduce problems of creep and fatigue, which ceramic matrices has the structural advantage. A sample ceramic recuperator printed using laminate laser-cut tape is shown in Figure 4.37.



**Figure 4.37: Sample mullite ceramic recuperator [36]**

4.3.5 Isometric View of the Recuperator

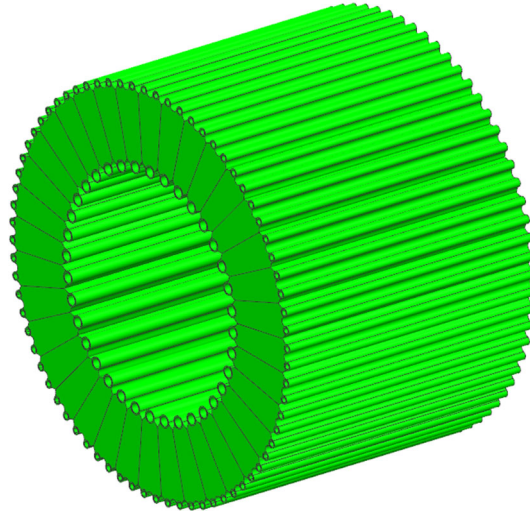


Figure 4.38: Isometric View of the Recuperator

4.4 Combustor

This Section will outline the design of the combustor for the SR-1000BDE. The burner must operate with high thermal efficiency and total pressure recovery to meet the endurance goal stated in the RFP [1]. Table 4.15 presents the exact targets for efficiency and pressure recovery that are based on Reference 8 for 2025 EIS [8].

Table 4.15: Major combustor cycle parameters

	Loiter (Design Point)
$\eta_b$ (%)	99.9
$\pi_b$ (%)	96.9
$T_{t4}$ (K)	1205

4.4.1 Combustor Architecture

There are three main classes of burner architecture: can, can-annular, and annular. Present-day can combustors are used primarily for industrial applications. Can and can-annular combustors, as found on many early jet engines, were quickly ruled out for their excess weight and length. All modern aircraft gas turbines employ annular burners which boast lower weight and better pressure recovery than can or can-annular burners. Turbofans and turbojets generally use straight-throughflow annular combustors while turboprop and turboshaft engines tend to use reverse-flow annular combustors [46]. The baseline engine, the TPE331-10, uses a reverse-flow architecture. The main benefit of the reverse-flow burner is a

reduction in engine weight and shaft length. Weight decreases because the shorter shaft has lower bending moments and requires fewer bearings. Shorter length enables closer coupling between the turbine and compressor. This is favorable for the high shaft speeds in this engine [46]. In keeping with industry practice for engines of its size, a reverse-flow burner was chosen for the SR-1000BDE.

The configuration of the SR-1000BDE burner is shown in Figure 4.39. The liner is shown as red while the casing is shown as silver. Air is turned by 180° through the recuperator and this heated air enters

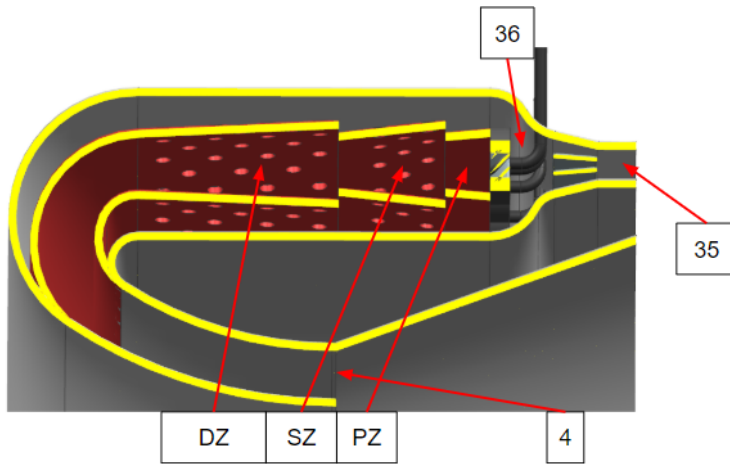


Figure 4.39: Configuration cutaway

through station 35 from the recuperator exit. Table 4.16 gives a description of each station number.

Table 4.16: Station descriptions

<b>3</b>	<b>Compressor Discharge</b>
<b>35</b>	<b>Heat Exchanger Exit</b>
<b>36</b>	<b>Diffuser Exit</b>
<b>PZ</b>	<b>Primary Zone</b>
<b>SZ</b>	<b>Secondary Zone</b>
<b>DZ</b>	<b>Dilution Zone</b>
<b>4</b>	<b>Turbine Inlet</b>

#### 4.4.2 Fuel Choice

While many alternative fuels are currently in development, this engine will employ Jet A-1 [46]. As the most popular jet fuel in the world, there is an established infrastructure for it at most airports [47]. This ability to launch from nearly any airport will permit greater on-target loiter. The slightly lower freezing point of Jet A-1 gives it an edge over Jet A. Greater flexibility in operating environment is permitted by the lower freezing point.

### 4.4.3 Combustor Efficiency

Thermal efficiency was estimated using primary zone equivalence ratio and Lefebvre’s  $\theta$ -parameter. The  $\theta$ -parameter is defined by the equation in Figure 4.40 [9]. The  $b$  term is calculated using Eq. 32, where  $\phi$  is the equivalence ratio of the primary zone.

$$b = \sqrt{2} \left( 1 + abs \left( \ln \left( \frac{\phi}{1.03} \right) \right) \right) \tag{Eq. 32}$$

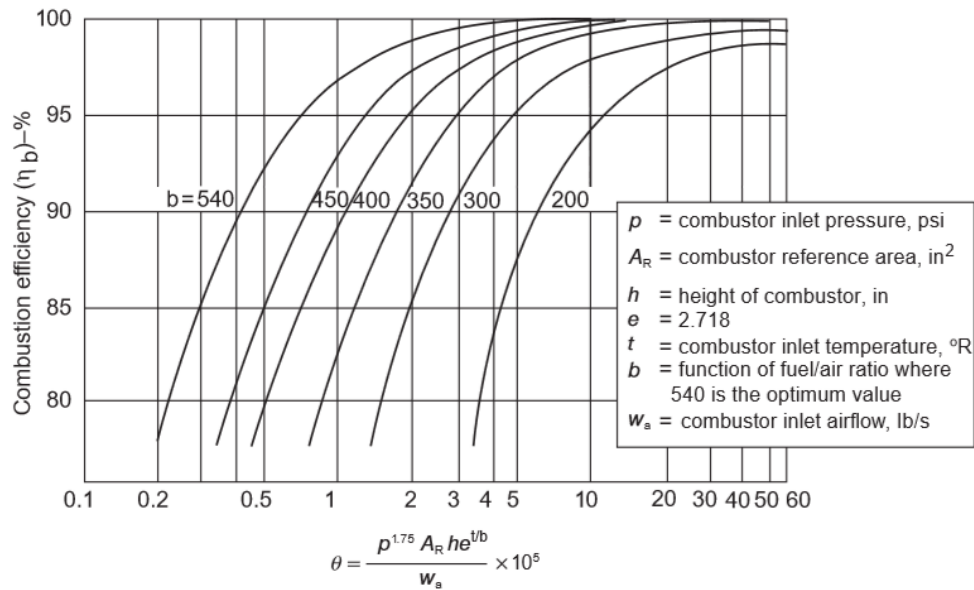


**Figure 4.40: Correlation of  $\theta$ -parameter to combustion efficiency [9]**

It is clear from Figure 4.40 that a higher value of  $\theta$  corresponds to higher efficiency. Inlet pressure, temperature, and mass flow were dictated by the overall thermodynamic cycle and were not considered variable for achieving the target efficiency. Burner size and primary zone equivalence ratio were the only design variables that could be altered to achieve favorable magnitude in  $\theta$  and  $b$ . While a higher  $b$  will decrease the required  $\theta$  for a given efficiency, the increase in  $b$  will decrease  $\theta$ . A primary zone equivalence ratio of 0.71 was found to yield a good magnitude of  $b$  with manageable impact on  $\theta$ . This is within the flammability limits presented in Figure 4.41 for kerosene type fuels in a quiescent environment at sea level. The increased pressure and temperature found in this burner will widen the flammability

limits from that sea level atmospheric condition. With adequate flameholding in the primary zone assured (Section 4.4.8), 0.71 was deemed a stable primary zone equivalence ratio for this design.

With  $\phi_{PZ}$  fixed, liner height and casing area were driven up to achieve the target thermal efficiency. The ratio of liner to casing height is a fixed ratio chosen to minimize mixing pressure loss. Section 4.4.8 will detail the selection of this ratio. Here, the important point is that liner height is not a free variable. Only casing area

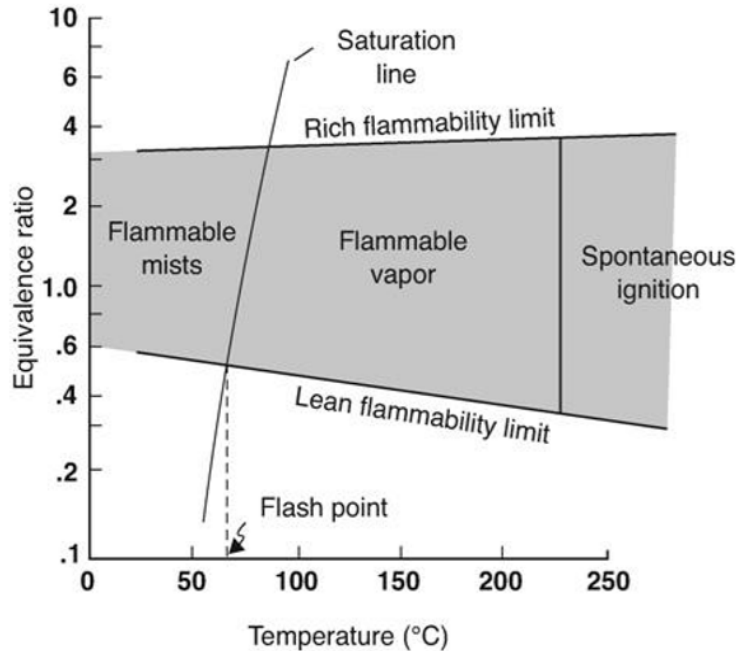


Figure 4.41: Flammability limits for kerosene type fuel [9]

Table 4.17: Values for calculating efficiency.

$P_{t36}$ (kPa)	769
$T_{t36}$ (K)	829
$A_{ref}$ (m <sup>2</sup> )	0.0212
$H$ (m)	0.0147
$\dot{m}_{36}$ (kg/s)	1.90
$b$ (~)	397
$\theta$ (~)	$9.54 \times 10^5$

can be changed to achieve the required magnitude of  $\theta$ . Table 4.17 gives the final values used to achieve 99.9% design point thermal efficiency. Casing area was chosen as the minimum required to reach the efficiency objective. Greater casing area means that the pre-diffuser must have a

larger area ratio. This carries losses in total pressure that must be mitigated in the diffuser design.

#### 4.4.4 Diffuser Configuration Selection and Design

To alleviate total pressure losses in the burner, air exiting the recuperator must be decelerated. The design objective for the diffuser is to minimize total pressure loss while decelerating air from the compressor by roughly 80% [46]. Total pressure loss in the diffuser arises from two different mechanisms: frictional losses and separation losses. The first diffuser considered was the dump diffuser, as pictured in Figure 4.42. This diffuser minimizes frictional losses at the expense of significant separation losses. Next,

a diffuser with splitter vanes was considered. This design reduces separation losses with its shallow wall angle but incurs frictional losses due to thick boundary layers [8]. Finally, a hybrid diffuser was considered. This architecture uses a bound vortex to prevent separation upstream of a wide-angle diffuser – seen in Figure 4.42. This bound vortex requires bleed air, such as that used for turbine cooling. It is the highest-risk of the three configurations [48].

An area ratio of 5.15 is required to reach the casing area stipulated by the  $\theta$ -parameter. This decelerates the incoming flow by roughly 80% to a Mach number of 0.04, in keeping with Lefebvre’s

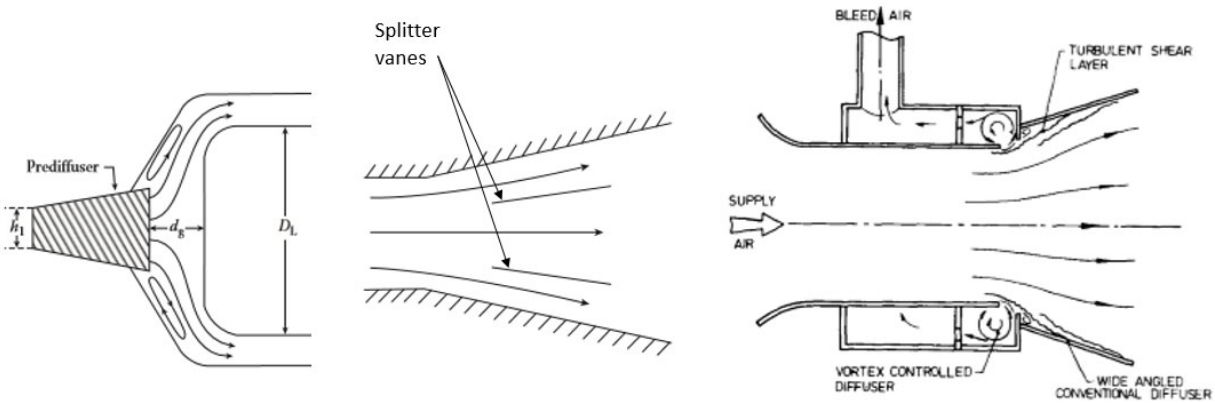


**Figure 4.42: Definition sketch for dump diffuser (left) [45], wide angle diffuser with splitter vanes (center) [45], and hybrid diffuser (right) [47]**

recommendation. Hybrid diffusers have not seen use at area ratios this high [46,49]. Additionally, with uncooled turbine nozzles, there is no use for the bleed air required in a hybrid diffuser. That architecture was determined to be too high risk and poorly suited for this application. For a diffuser with two splitter vanes separating three passages of 9-degree divergence angle [8], a length of 9.7 cm is required. This is greater than the preliminary estimates of overall combustor length so that architecture was ruled out. The dump diffuser offers short length and simplicity, however, the pressure loss of 3.5% is greater than the total burner pressure drop allocation.

Following recommendations from Reference 8, a compromise was reached by combining a three-stream flat wall diffuser with a dump diffuser. For this design, a split three-stream diffuser with area ratio of 2.0 feeds into a dump diffuser with area ratio of 2.6. Such a

**Table 4.18: Diffuser exit flow characteristics**

$P_{t36}$ (kPa)	771
$A_{35}$ (m <sup>2</sup> )	0.004
$M_{35}$ (-)	0.20
$A_{36}$ (m <sup>2</sup> )	0.0212
$M_{36}$ (-)	0.04

division of area ratios was found to give a good balance of pressure recovery and overall diffuser length. Maximally thick boundary layers are assumed at the exit of the recuperator. Following Eq. 33 from Reference 8, where  $B_t$  is the thickness of the turbulent boundary layer at the diffuser inlet, efficiency in the three-stream diffuser was found to be 64%. Total diffusion efficiency was then calculated using dump diffuser area ratio, flat wall diffuser efficiency, and flat wall area ratio. Pressure recovery was then calculated directly from diffusion efficiency. The combined diffuser configuration reduces the pressure loss to 1.4%, compared to 3.5% for the pure dump diffuser. Table 4.18 gives the state of flow exiting the diffuser in greater detail.

$$\eta_{D9^\circ} \cong 0.965 - 2.72B_t \quad \text{Eq. 33}$$

$$0.01 < B_t < 0.12$$

Flow exiting the dump diffuser must be given adequate distance to reattach on the casing wall. This is the assumption used in calculating pressure recovery.

If flow does not reattach, pressure losses will be extreme, and the diffuser could stall. This distance for reattachment is called the dump gap,  $D_g$ , shown in Figure 4.43. It is given as a ratio of split diffuser exit height,  $H_m$ . This design uses a dump gap equal to 1.2 times  $H_m$ , following References 50, 51, and 52.

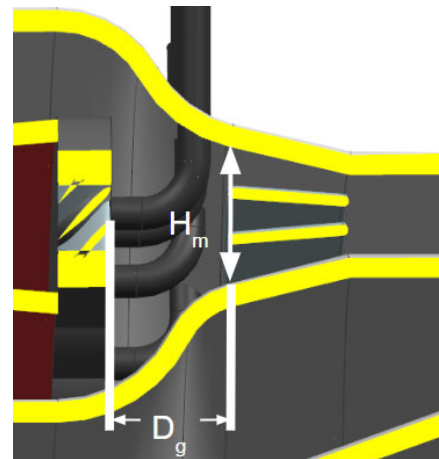


**Figure 4.43: Dump gap term definitions**

#### 4.4.5 Emissions

With global energy consumption constantly increasing, it is important that toxic emissions are mitigated as much as possible. Engine exhaust is composed mainly of carbon monoxide (CO), carbon dioxide (CO<sub>2</sub>), water vapor (H<sub>2</sub>O), particulate matter, unburned hydrocarbons (UHC), oxides of nitrogen (NO<sub>x</sub>), and excess atmospheric oxygen and nitrogen. Of these, CO, UHC, and NO<sub>x</sub> are toxic to humans and are of great relevance to combustor design. UHC and NO<sub>x</sub> also contribute to photochemical smog and acid rain [46]. These pollutants are regulated in the United States by the Environmental Protection Agency

(EPA) and internationally by the International Civil Aviation Organization (ICAO). Both agencies regulate aviation gas turbine engines with thrust greater than 26.7 kN [53]. This engine does not meet that criteria for regulation. Nonetheless, the impact of design choices on emissions will briefly be discussed.

The rates of formation for CO, UHC, and NO<sub>x</sub> are strong functions of temperature. NO<sub>x</sub> emissions increase with temperature, forming appreciably at temperatures above about 1800 K [9]. Meanwhile, CO and UHC emissions *decrease* with increasing temperature.

UHC production is related to the problem of injector fouling in small combustors [46]. Production of UHC and CO is a strong function of combustor inlet temperature. Figure 4.44 from Henderson and Blazowski shows how both CO and UHC decrease sharply with increasing inlet temperature [54]. The recuperator offers great benefit to this by increasing the inlet temperature significantly.

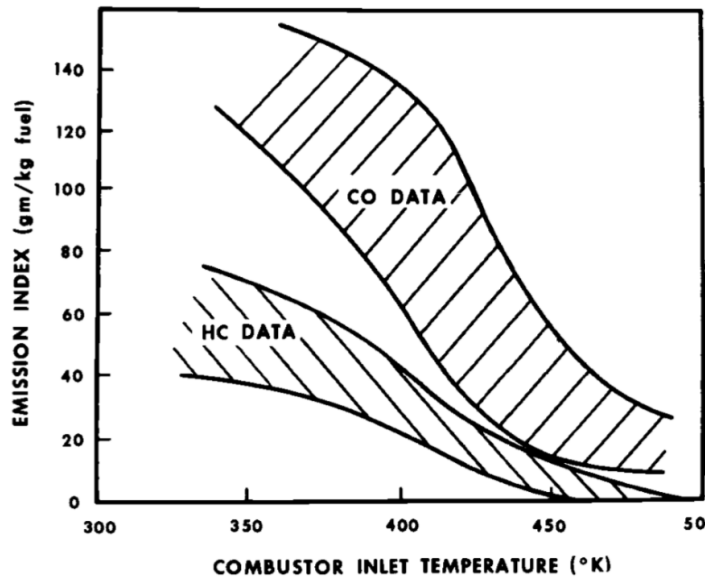


Figure 4.44: Relationship of CO and UHC production to combustor inlet temperature [54]

GasTurb cycle analysis provided a NO<sub>x</sub> severity index,  $S_{NO_x}$ , of 0.439. This was used to calculate the emission index, in grams of NO<sub>x</sub> per kg of fuel, using Eq. 34 [5]. Plugging this emission index into Eq. 35 gives that this engine emits 1.78 g/kN of shaft power [46]. This undercuts the requirements of both ICAO and the EPA for engines with 26.7 kN of power.

$$Emission\ Index\ \left(\frac{g}{kN\ fuel}\right) \approx 32 \times S_{NO_x} \tag{Eq. 34}$$

$$Emission\ \left(\frac{g}{kN}\right) = Emission\ Index\ \left(\frac{g}{kN\ fuel}\right) \times SFC\ \left(\frac{kg\ fuel}{kN\ hr}\right) \times Time\ (hr) \tag{Eq. 35}$$

Primary zone temperature,  $T_g$ , represents the maximum temperature reached during combustion.  $\text{NO}_x$  and CO emissions are also functions of this temperature. Figure 4.46 from Reference 8, shows that there is a range where both  $\text{NO}_x$  and CO are near a minimum. Following recommendations from Reference 8, a primary zone temperature of 1780 K was chosen. This temperature corresponds with the primary zone equivalence ratio of 0.71, stated earlier in Section 4.4.3. Because the

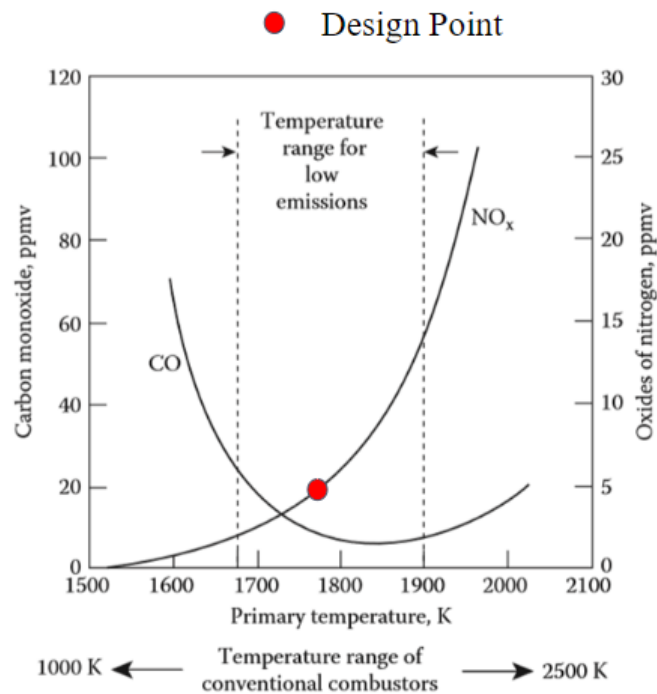


**Figure 4.46: Temperature dependence of regulated pollutants [8]**

equivalence ratio never reaches stoichiometric, where temperature is maximized,  $\text{NO}_x$  production is mitigated. This can be seen qualitatively in Figure 4.45 where maximum  $\text{NO}_x$  production occurs near stoichiometric conditions.

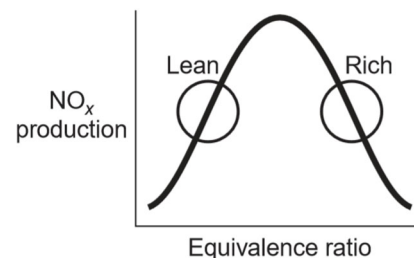


**Figure 4.45:  $\text{NO}_x$  production as a function of equivalence ratio [9]**

#### 4.4.6 Advanced Liner Material and Cooling

A primary objective for the combustor of a gas generator is to provide a uniform temperature profile at the turbine inlet. Recent advances in high temperature materials have enabled modern combustors to operate at higher temperatures with lower cooling. When less air is required for cooling of the liner, more air can be used for dilution. An increase in dilution air has a favorable impact on turbine inlet temperature uniformity. Traditionally, the best high temperature materials for the liner were nickel superalloys. Ceramic Matrix Composites, or CMCs, have recently been

introduced to gas turbine combustor liners on the GEnX and GE9X to enable combustor temperatures up to 1590 K (2400 °F) [55].

The SiC/SiC composite overcomes the embrittlement problems of monolithic SiC composites by using small SiC fibers in the matrix. This provides ductility and damage tolerance comparable to nickel superalloys [56]. Silicon based composites encounter problems with accelerated oxidation in the high-steam environment of the combustor. The water vapor in the air oxidizes the silicon fibers and gradually vaporizes the interior of the liner. This can be prevented with an Environmental Barrier Coating (EBC). An EBC provides a layer of nonreactive material to protect the underlying CMC from oxidation and volatilization. As part of the Department of Energy's Ceramic Stationary Gas Turbine program in 1996, a CMC combustor liner with an EBC was tested for over 15,000 hours of continuous operation at a temperature of 1480 K [57]. While this result was for a stationary gas turbine, this 15,000-hour lifespan was assumed as a reasonable estimate for this CMC combustor liner for EIS of 2025.

The impact of the CMC combustor liner on cooling is quantified with maximum wall temperature,  $T_m$ . While capability up to 1590 K is claimed, the max wall temperature is kept at 1480 K to enable longer life [55, 57]. Cooling air mass fraction is estimated using the cooling effectiveness parameter,  $\Phi$ , as defined in Eq. 36 from Reference 48. Based on the cooling method selected, this parameter can be used to find  $\dot{m}_c$ . Using an industry standard, film with convection cooling, the cooling effectiveness parameter of 0.32 gives a 3% mass fraction of cooling air from Figure 4.47. Significant air can therefore be used for dilution and achieving a uniform temperature profile at the turbine inlet.

$$\Phi = \frac{T_g - T_m}{T_g - T_c} \quad \text{Eq. 36}$$

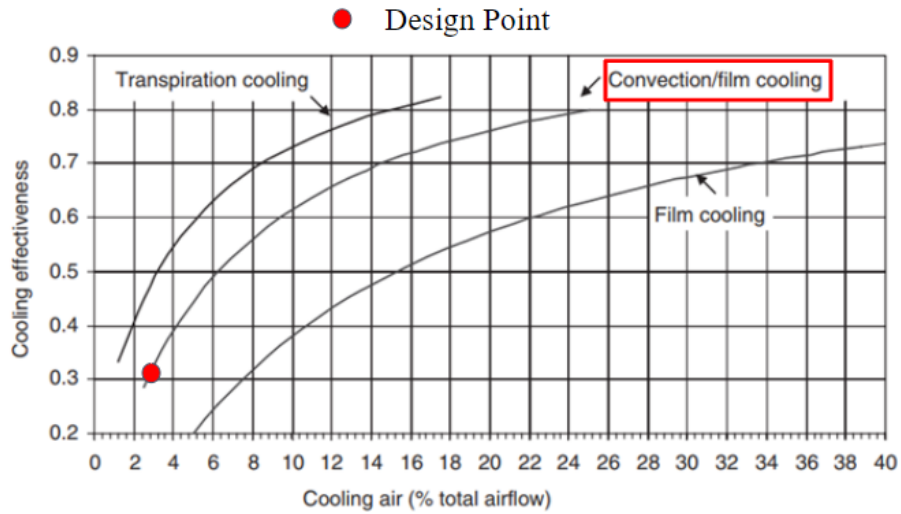


Figure 4.47: Correlation of cooling effectiveness to mass flow fraction [9]

#### 4.4.7 Air Partitioning

Methods for air partitioning between the primary zone, secondary zone, and dilution zone come from Reference 8. A schematic showing the division of air throughout the combustor is shown in Figure 4.48 [58]. Partitioning was driven primarily by combustion efficiency. Primary zone equivalence ratio was set to 0.71 to achieve a satisfactory value of the reaction rate parameter  $b$  used in estimating efficiency. This equivalence ratio sets the mass flow to the primary zone. Based on the assumption that combustion is complete at the end of the secondary zone, flow partitioning to the secondary and dilution zones is straightforward. Table 4.19 describes the air partitioning of this combustor.

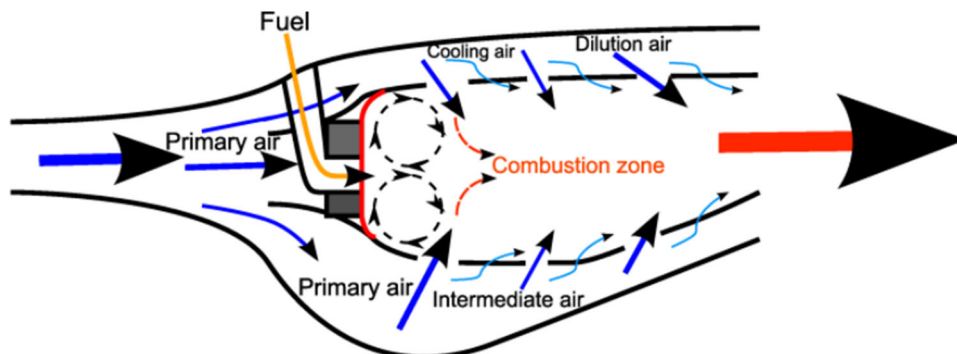


Figure 4.48: Air partitioning definition sketch [58]

**Table 4.19: Salient characteristics of combustor zones**

	Primary Zone	Secondary Zone	Dilution Zone
$\dot{m}$ (kg/s)	0.488	0.263	1.08
$\phi$ (-)	0.71	0.46	0.18
Length (m)	0.012	0.028	0.052

**4.4.8 Dome and Liner Sizing**

Four sources will be considered in estimating the total pressure loss of this combustor. The first two have already been considered: recuperator heat addition and diffusion. Mixing and combustion are the other two sources. Losses due to mixing are expected to dominate over losses from combustion. Pressure loss due to mixing cannot be eliminated entirely as there must be a pressure deficit across the liner to ensure adequate jet penetration. For an assumed total pressure loss, the optimal area ratio between the liner,  $A_L$ ,

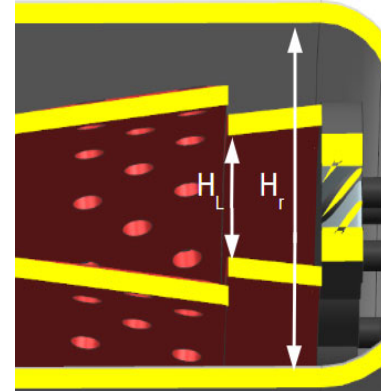


**Figure 4.49: Liner and reference height definitions**

and casing,  $A_R$ , is found with Eq. 37. The relevant heights for defining  $\alpha$ , Eq. 38, are shown in Figure 4.49.

$$\alpha = 1 - \left(\frac{\dot{m}_A}{\dot{m}_{32}}\right)^{\frac{2}{3}} \left(\frac{\Delta P_t}{q_r}\right)^{-\frac{1}{3}} \tag{Eq. 37}$$

$$\alpha = \frac{H_L}{H_r} \tag{Eq. 38}$$

After solving for  $\alpha$ , the critical pressure loss coefficient due to mixing was calculated using Eq. 39 where  $\tau_{PZ}$  is the total temperature ratio across the primary zone [8].

This critical pressure loss represents the minimum pressure loss across the liner that would ensure adequate jet penetration and mixing. By then solving for pressure loss from this critical  $C_p$ , a new assumed pressure loss can be used to calculate a new  $\alpha$ . This process was repeated, with slight modifications to ensure convergence in

**Table 4.20: Dome geometry**

$H_A$ (m)	0.0354
$A_A$ (m <sup>2</sup> )	0.0212
$H_L$ (m)	0.0147
$A_L$ (m <sup>2</sup> )	0.0088

different cases, to bring the total pressure loss within 5% of the critical value required for adequate mixing. This allowed for calculation of the dome and liner geometry presented in Table 4.20.

$$\left(\frac{\Delta P_t}{q_{ref}}\right)_{crit} = \left(\frac{\dot{m}_{PZ}}{\dot{m}_{32}}\right)^2 \left(\frac{1}{\alpha}\right)^2 \tau_{PZ}(2\tau_{PZ} - 1) \quad \text{Eq. 39}$$

The final component of total pressure loss is due to combustion raising the gas temperature from  $T_{132}$  to  $T_{t4}$ . Reference 9 provides a method to estimate this pressure loss based in Rayleigh flow. Eq. 40 shows the formula where  $q_{ref}$  is the dynamic pressure of flow exiting the dump diffuser. This equation gives a

**Table 4.21: Total pressure loss breakdown.**

$\pi_{Recuperator} (-)$	0.986
$\pi_{Diffuser} (-)$	0.986
$\pi_{b,cold} (-)$	0.997
$\pi_{b,hot} (-)$	0.999
$\pi_{b,tot} (-)$	0.969

0.04% pressure loss due to combustion. It is expected that this pressure loss is small compared to the aerodynamic losses in diffusion and mixing [9]. That is the case for this combustor. A summary of pressure loss sources for this burner design is presented in Table 4.21.

$$\Delta P_{t,hot} = q_{ref} \left(\frac{T_4}{T_{32}} - 1\right) \quad \text{Eq. 40}$$

Injection in small combustors is a technical challenge because of the small space available for complete mixing [46]. The injection of the fuel will take place through air blast atomizers based on modern industry practice and research done by NASA Glenn Research Center [59]. Design point for this engine is a low power setting. While many of the injectors tested in the NASA study experienced blowout at low power settings or idle, the air blast atomizers showed a high level of efficiency at all power settings [46, 59]. Air blast atomizers are superior to simplex nozzles at low power settings because they do not rely on high back pressures. Rather, they use the kinetic energy of a blast of air to atomize the fuel droplets coming from the injector. Air blast atomizers also have very low soot formation due to the high combustion uniformity they promote [46].

Following recommendations from Reference 8, airfoil swirlers are used. Effectiveness of the swirler is measured by the swirl number,  $S'$ , which is proportional to the size of the recirculation zone in front of the injector. Swirl number is defined in Eq. 41.

$$S' = \frac{2}{3} \tan(\alpha_{sw}) \left[ \frac{1 - \left(\frac{r_h}{r_t}\right)^3}{1 - \left(\frac{r_h}{r_t}\right)^3} \right] \quad \text{Eq. 41}$$

This number is calculated using swirler geometry and airfoil angles. Specifying 36 swirlers based on the size of the liner and gives a tip radius is 7.1 mm from continuity consideration. The swirler airfoil vane angle,  $\alpha_{sw}$ , is taken to be  $45^\circ$  following recommendations from Reference 2. Hub radius for the swirler, the air blast atomizer outer radius, is chosen to be 3.2 mm [60]. These design variables result in a swirl number of 0.62: more than the 0.60 recommended for adequate swirl and flameholding in the primary zone

[8]. Figure 4.50 shows the liner with swirlers and injectors shown.

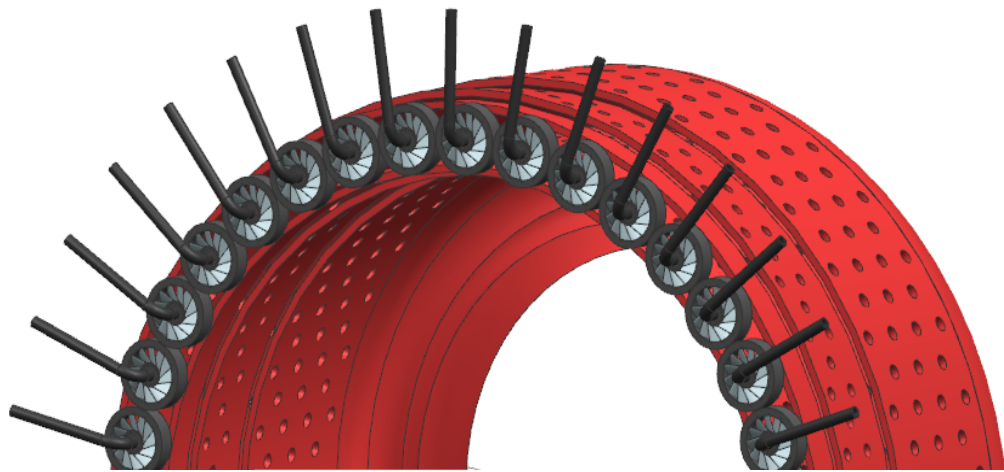


**Figure 4.50: Injectors and swirlers**

#### 4.4.9 Secondary and Dilution Zone Holes

With the pressure drop across the liner now known, air holes to enable the proper air partitioning can be sized. These holes were sized following methods provided by Reference 8. Secondary zone jets are designed to penetrate to half the liner height. This will allow flameholding and recirculation in the primary zone. Flameholding allows for a stable flame while recirculation enables adequate residence time for complete combustion. Dilution holes are sized to allow for jet penetration to one third of the liner height. The number and diameter of holes in each zone are presented in Table 4.22.

**Table 4.22: Hole distribution and size for air partitioning**

	Secondary Zone	Dilution Zone
<b>Number of holes, <math>N_h</math></b>	480	1110
<b>Hole diameter, <math>D_h</math></b>	3.7 mm	4.1 mm

**4.4.10 Combustor Length Determination**

Estimates for length came from Mattingly and are presented here in Eq. 42, Eq. 43, and Eq. 44. Primary zone length was calculated as 10 mm and secondary zone length as 29 mm. It was found that the specified hole spacing with seven rows of dilution holes did not fit within the length estimate for that section. The length was therefore increased from 21 mm to 52 mm to accommodate the required holes.

$$L_{PZ} \approx 2S'r_t \tag{Eq. 42}$$

$$L_{SZ} \approx 2H_L \tag{Eq. 43}$$

$$L_{DZ} \approx 1.5H_L \tag{Eq. 44}$$

**4.4.11 Relight Envelope**

Various flight conditions are presented in the RFP [1]. Table 4.23 gives those flight conditions and attendant U.S. standard atmosphere pressures [62]. Relight is assured for all segments of the reference mission provided. The relight envelope is shown in Figure 4.51. At maximum speed, the highest altitude where

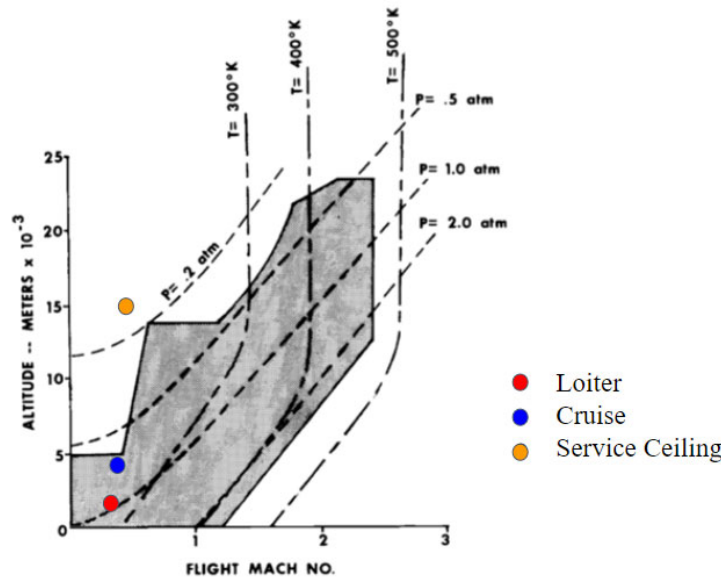


**Figure 4.51: Relight envelope [9]**

relight can occur is 20,000 ft. This maximum relight altitude can be increased significantly by the addition of a small mass fraction of oxygen, on the order of 0.5% [46]. The aircraft specified in the RFP will not carry oxygen for cabin air because it is unmanned. There is a tradeoff of risk between carrying excess onboard oxygen and the inability to relight at high altitude. The team decided that an onboard oxygen system is worth the added weight to ensure relight at high altitude.

**Table 4.23: Flight conditions from RFP [1]**

Flight Condition	Altitude	Velocity	P <sub>static</sub>	P <sub>total</sub>
Takeoff	MSL	Zero	101 kPa (1 atm)	101 kPa (1 atm)
Loiter	7,000 ft (2000 m)	190 KTAS (0.28 M)	78.2 kPa (0.77 atm)	82.5 kPa (0.81 atm)
Cruise	12,500 ft (4000 m)	220 KTAS (0.33 M)	63.5 kPa (0.63 atm)	68.3 kPa (0.67 atm)
Service Ceiling, Maximum Speed	50,000 ft (15,000 m)	260 KTAS (0.38 M)	11.1 kPa (0.11 atm)	12.2 kPa (0.12 atm)

**4.4.12 Combustor Material Selection, Stress Analysis and Mechanical Design**

The liner material, SiC/SiC CMC, has already been described in Section 4.4.6. Titanium alloys are viable for the compressor outlet; however, the temperature rise across the recuperator requires the use of a nickel superalloy for the combustor casing. The casing will be therefore made from Inconel 718 following recommendations from Reference 63.

The casing is treated as an annular pressure vessel. Maximum stress is given by the hoop stress, from Eq. 45. For an annulus, hoop stress is compressive on the interior and tensile on the exterior. Allowable stresses for SiC/SiC CMCs and Inconel 718 are presented in Table 4.24 [56, 64, and 65].

**Table 4.24: Combustor material properties**

Material	$\sigma_y$	$\rho$
SiC/SiC CMC	1000 MPa	2100 kg/m <sup>3</sup>
Inconel 718	160 MPa	8200 kg/m <sup>3</sup>

$$\sigma_{hoop} = \frac{Pr}{t} \tag{Eq. 45}$$

This stress is proportional to radius. Because this engine is so small, hoop stress calculations with a 1.5 factor of safety give the required thickness of the casing to be under one millimeter. For manufacturability and durability, this thickness was increased to 2 mm. Such a thickness agrees with the

thickness presented in Reference 63. The liner was also chosen to be 2 mm thick with a 0.5 mm thick EBC [56].

Following recommendations for bolt spacing from Reference 61, edges of the secondary and dilution zone holes are chosen to be separated by twice their diameter [61]. To save axial space, hole rows are offset from one another. This configuration is shown schematically in

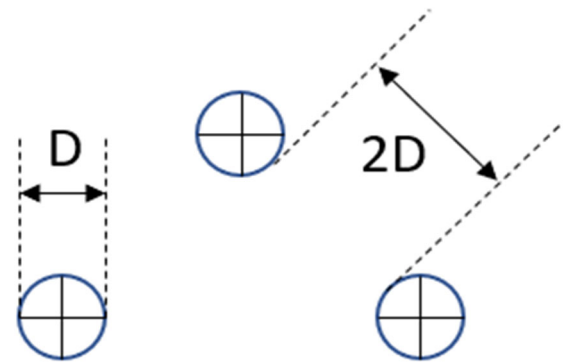


Figure 4.52: Hole spacing definition sketch

Figure 4.52. This spacing resulted in three rows of holes in the secondary zone and seven rows in the dilution zone.

#### 4.4.13 Isometric View of the Combustor

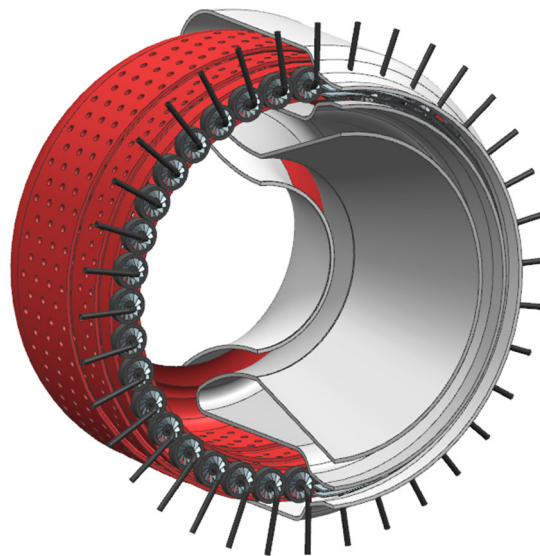


Figure 4.53: Combustor Isometric View

### 4.5 Turbine

The turbine section of the engine is designed with a single spool high-pressure turbine (HPT) which generates power for the compressor section of the engine, and a single spool low-pressure turbine (LPT) which generates power for the electric generator. The HPT, also known as the gas generator turbine, is

composed of one stage and the LPT, also known as the power turbine, is designed with two stages to generate the necessary shaft power. The two spools are designed to be counter-rotating because this is known to decrease both weight and length [66]. Further depth on the design of the gas generator turbine and power turbine is provided in this section.

#### 4.5.1 Turbine Pitchline Design Parameters

Both the gas generator turbine and power turbine were designed to have a constant axial velocity. The flow station data at loiter can be seen in Table 4.25 and Table 4.26 for the gas generator turbine and power turbine respectively. The first nozzle of each spool must be choked; therefore, the first nozzle exit Mach number was chosen to be slightly supersonic at  $M_2=1.13$  for the gas generator turbine and  $M_2=1.15$  for the power turbine [9]. The flow from the combustor was assumed to be swirl free. The shaft angular speed of the gas generator turbine is set by the compressor at 62,000 rpm. The power turbine was chosen to rotate at 45,400 rpm to generate the power required, while keeping positive margins of safety for the blades. The design was done using varying hub and tip radii to keep the pitchline radius constant throughout the gas generator turbine and power turbine, respectively. A definition sketch of a constant pitchline axial turbine is shown Figure 4.54.

**Table 4.25: HPT Flow Data**

<b>Flow Station Data: HP Turbine</b>	<b>Value</b>
<b>Inflow (kg/s)</b>	1.92
<b>Inflow Total Pressure (kPa)</b>	769
<b>Inflow Total Temperature (K)</b>	1205
<b>Inflow Fuel-air-Ratio</b>	0.015
<b>Inflow Mach #</b>	0.36
<b>Inflow Area (m<sup>2</sup>)</b>	0.0039
<b>Pressure Ratio</b>	0.297

**Table 4.26: LPT Flow Data**

<b>Flow Station Data: Power Turbine</b>	<b>Value</b>
<b>Inflow (kg/s)</b>	1.92
<b>Inflow Total Pressure (kPa)</b>	228
<b>Inflow Total Temperature (K)</b>	1022
<b>Inflow Fuel-air-Ratio</b>	0.013
<b>Inflow Mach #</b>	0.55
<b>Inflow Area (m<sup>2</sup>)</b>	0.0085
<b>Pressure Ratio</b>	0.445

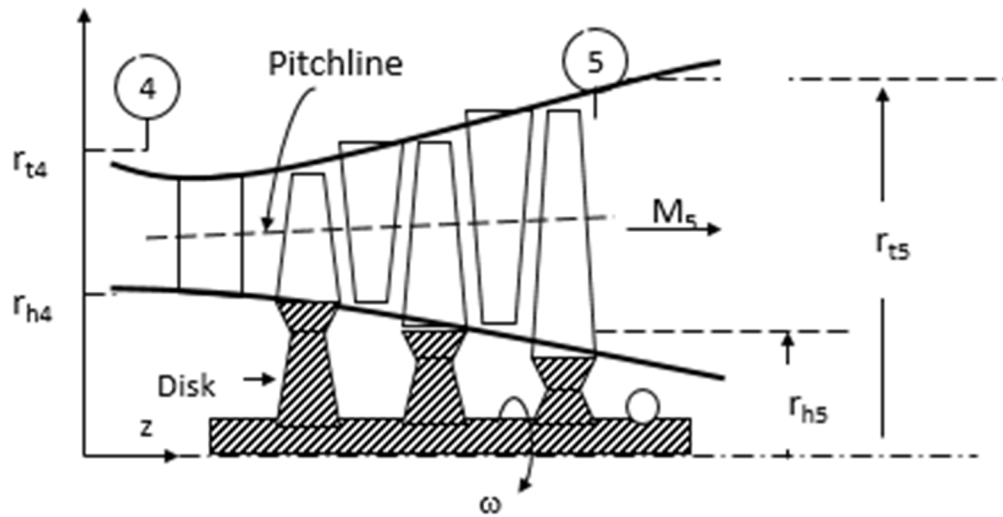


Figure 4.54: Constant Pitchline Turbine Definition Sketch [9]

#### 4.5.2 Turbine Flow Calculations and Aerothermodynamics

The baseline for the design was given in the RFP and calculated using GasTurb [1, 5]. A definition sketch for each stage can be seen in Figure 4.55. The optimized cycle was then used along with design choices discussed in this section to generate the power required for both the power turbine and gas generator turbine. There were three main design choices, which were the first nozzle Mach numbers, rotor relative Mach numbers, and the exit flow angles for the nozzles. There were three different stream surfaces that were evaluated for the gas generator turbine and the power turbine, which include the hub, pitchline, and tip.

The power that is needed from the gas generator turbine is determined by the compressor, which requires 542 hp. Assuming a mechanical shaft efficiency 0.995, the turbine needs to generate 542 hp. Power at pitchline was calculated using the Euler Turbine Equation, as shown in Equation 46 [9]. The total power generated by the gas generator turbine is 557 hp, which is 1.98% over what the compressor requires.

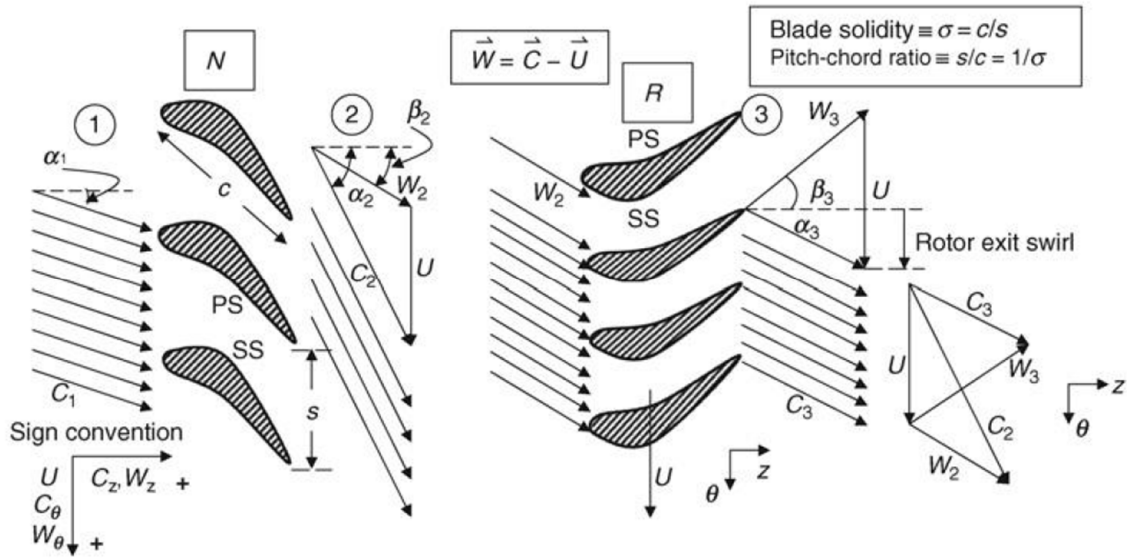


Figure 4.55: Stage Definition Sketch [9]

$$\dot{\rho}_{stage} = \dot{m}\omega(r_2 C_{\theta 2} - r_3 C_{\theta 3}) \quad \text{Eq. 46}$$

The Mach number and flow angle at the nozzle exit were both design variables that were set at 1.13 and 70 degrees, respectively. Mach number at the exit was set at 1.13 for the pitchline because the first nozzle must operate in a choked state across all stream surfaces. The nozzle exit flow angle was set at 70 degrees, as it is stated in Mattingly that the optimal performance is achieved at  $40^\circ < \alpha_2 < 70^\circ$  [9]. However, angles above 70 degrees were avoided as to not induce flow separation. The rotor relative exit Mach number was set at 0.66. This affects the power output and the stage performance, where higher values increase the stage performance. The maximum viable value is 0.9, which was avoided for the gas generator turbine design. The first nozzle exit flow angle and the relative Mach number at the rotor exit produced a rotor exit flow of  $-3.0^\circ$ , which is close to zero with the small angle assumption. This is desired to not induce swirl into the nozzle for the power turbine. The Mach numbers and velocity triangle components can be seen in Table 4.27.

**Table 4.27: HPT Stage Design**

		HPT							
		Streamline	M (~)	M <sub>r</sub> (~)	C (m/s)	α (deg)	β (deg)	U <sub>m</sub> (m/s)	W (m/s)
Stage 1	Inlet (1)	hub	0.36		135	0	0	0	0
		mean	0.36		135	0	0	0	0
		tip	0.36		135	0	0	0	0
	N (2)	hub	1.31	0.87	783	72.3	62.8	284	520
		mean	1.13	0.66	696	70	54.2	324	407
		tip	1.00	0.51	629	67.8	42.5	364	323
	R (3)	hub	0.39	0.62	239	-3.8	-51.6	284	383
		mean	0.39	0.67	238	-3.0	-54.7	324	412
		tip	0.39	0.72	238	-2.5	-57.6	364	444

The power needed to be generated by the power turbine is determined by the RFP. At loiter, the power turbine is required to generate 603 hp of power. Assuming a mechanical shaft efficiency  $\eta_m = 0.995$ , the power turbine must generate 606 hp of power. The power generation for the power turbine was calculated using Equation 46. Two stages were necessary to produce the power required, while maintaining efficiencies and an exit flow angle into the exhaust of nearly zero. The power turbine produces 633 hp of power, which is 4.41% more than the desired value, but still within 5% of the baseline.

The Mach number was set to 1.15, because it is required that the first nozzle operate in a choked condition at all three stream surfaces. The nozzle exit flow angle was set to  $59^\circ$  to maximize power output without having flow separation. The rotor relative exit Mach number was set at 0.77. The nozzle flow angle and the relative Mach number at the rotor exit produce a flow angle at the first stage rotor exit of  $3.0^\circ$ . The second stage had a nozzle exit flow angle set to  $41^\circ$  and a rotor relative Mach number of 0.83. This produced an exit swirl of  $-0.1^\circ$ . The Mach numbers and velocity triangle components can be seen in Table 4.28.

**Table 4.28: LPT Stage Design**

		LPT							
		streamline	M (~)	M <sub>r</sub> (~)	C (m/s)	α (deg)	β (deg)	U <sub>m</sub> (m/s)	W (m/s)
Stage 1	N (4)	hub	1.40	1.01	756	59.0	52.4	243	549
		mean	1.15	0.75	651	59.0	38.1	295	426
		tip	1.01	0.62	581	59.0	20.8	347	483
	R (5)	hub	0.60	0.71	336	4.2	-33.1	243	400
		mean	0.59	0.77	336	3.0	-39.6	295	435
		tip	0.60	0.84	336	2.4	-44.8	347	473
Stage 2	N (6)	hub	0.99	0.70	530	50.7	26.5	243	375
		mean	0.81	0.61	444	41.0	-0.6	295	335
		tip	0.73	0.64	405	34.0	-19.8	347	357
	R (7)	hub	0.62	0.77	335	-0.1	-36.0	243	415
		mean	0.62	0.83	335	-0.1	-41.4	295	447
		tip	0.62	0.88	335	-0.1	-46.0	347	483

The velocity triangles for the gas generator turbine and the power turbine at the three different stream surfaces can be seen in Figure 4.56. The pitchline is labeled and the other streamlines follow the same convention. Note that the power turbine is opposite of the gas generator turbine, which is due to it rotating the opposite direction. This causes the flow angles and directions of the speeds to be reversed.

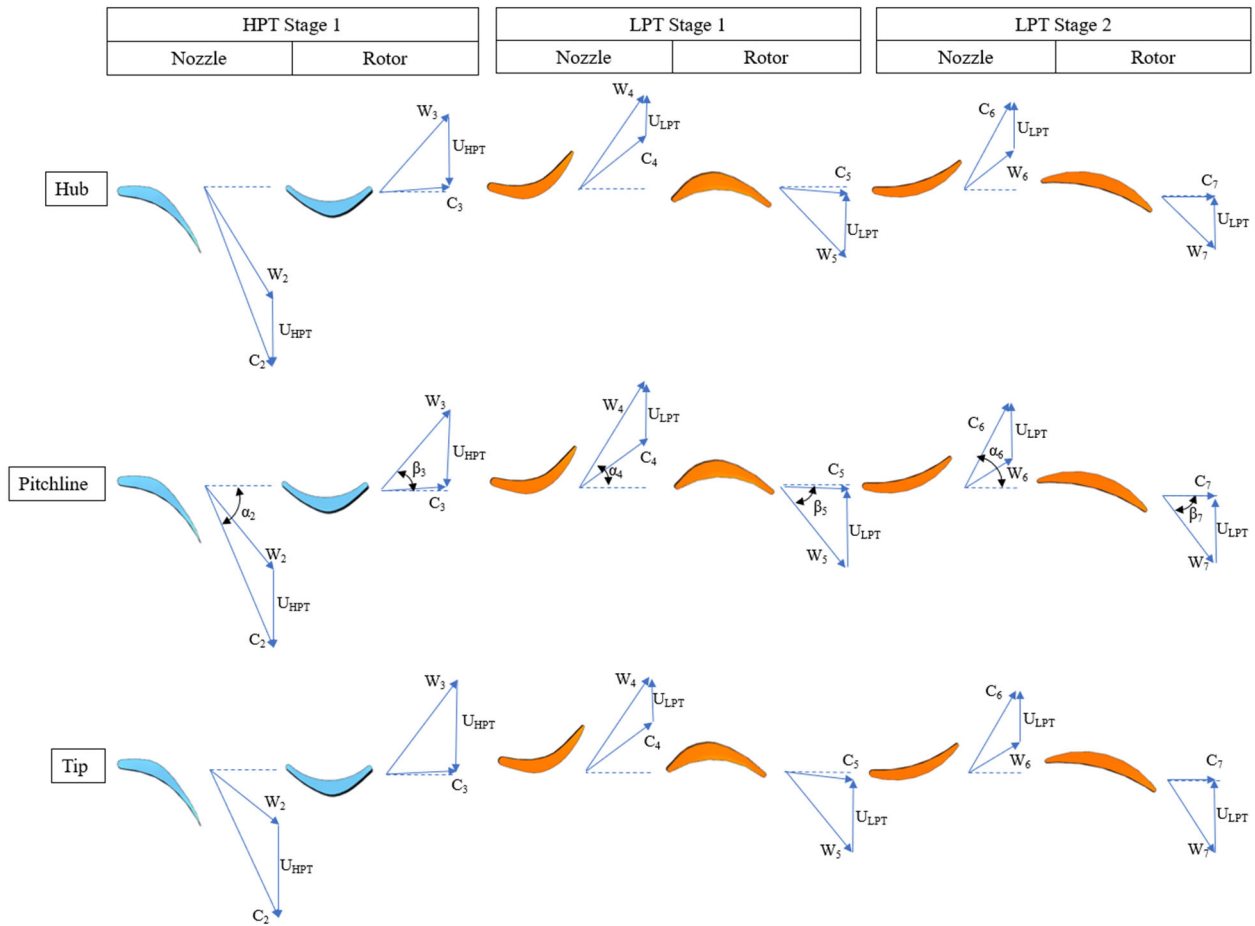


**Figure 4.56: Velocity Triangles for the Turbine**

The stage degree of reaction (Eq. 47) is the ratio of the rotor pressure drop to the total stage degree of reaction. For the turbine designed, most of the flow expansion is happening in the nozzle. This occurs here due to the degrees of reaction for the stages, which fall between 0 and 0.5. The second stage of the power turbine, however is a reaction stage because the total pressure drop is balanced across the rotor and the stator as the degree of reaction is close to 0.5. Degree of reaction is shown, along with the power and specific work for each stage in Table 4.29. To reach the power required for the cycle, the power turbine had to be composed of two stages that make 633 hp of power when combined.

$${}^{\circ}R_m = 1 - \frac{C_{\theta 2} + C_{\theta 3}}{2U_{m1}} \quad \text{Eq. 47}$$

**Table 4.29: Stage Parameters**

	HPT		LPT	
	Stage 1	Stage 1	Stage 2	Stage 2
<b>°R</b>	0.010	0.024	0.506	
<b>Specific work (hp)</b>	289.9	213.8	115.5	
<b>Power (hp)</b>	555.9	410.5	221.8	

The highest total temperature in the turbine is 1205 K at the inlet to the gas generator turbine. Ceramic Matrix Composites (CMC's) were chosen with a maximum material temperature of 1589 K. Due to this, cooling was not used throughout the turbine. This means that the engine can generate more power, while also being more fuel efficient [67]. These temperatures and pressures can be seen in Table 4.30 at the three different stream surfaces. The flow expansion across the rotor can be seen in this table as well, as noted when discussing the stage degree of reaction.

**Table 4.30: HPT Temperature and Pressure Characteristics**

HPT						
		streamline	T <sub>t</sub> (K)	T (K)	P <sub>t</sub> (kPa)	P (kPa)
Stage 1	Inlet (1)	hub	1205	1181	768	707
		mean	1205	1181	768	707
		tip	1205	1181	768	707
	N (2)	hub	1205	946	765	282
		mean	1205	1000	765	355
		tip	1205	1038	765	413
	R (3)	hub	1022	998	237	215
		mean	1022	998	228	207
		tip	1023	999	219	198

Table 4.31 shows the temperatures and pressures in the power turbine. Due to the flow temperatures being well below maximum material operating temperatures, there is no need for cooling. The exhaust gases leave the power turbine and go through the recuperator. Therefore, it was important to make sure that the gases were still hot enough to make the recuperator effective. The power turbine has a pressure ratio of 0.45. This decrease in pressure allows the nozzle pressure ratio to be close to one.

**Table 4.31: LPT Temperature and Pressure Characteristics**

		LPT				
		streamline	T <sub>t</sub> (K)	T (K)	P <sub>t</sub> (kPa)	P (kPa)
Stage 1	N (4)	hub	1022	770	226	73
		mean	1022	835	226	226
		tip	1022	874	226	226
	R (5)	hub	882	833	130	130
		mean	882	832	123	123
		tip	881	832	115	115
Stage 2	N (6)	hub	882	759	129	70
		mean	882	795	121	80
		tip	881	809	114	81
	R (7)	hub	810	760	89	69
		mean	820	771	102	79
		tip	827	778	79	62

### 4.5.3 Turbine Blade and Annulus Sizing

The turbine was designed for a constant pitchline. The gas generator turbine and the power turbine have different pitchlines to allow for larger blades in the power turbine. An interduct was implemented to account for the change in pitchlines between the gas generator turbine and the power turbine. The radii for the different stations within the turbine are listed in Table 4.32. These can be seen in Figure 4.57 to represent the 2-D flow path through the turbine.

**Table 4.32: Radii through the Turbine**

	I (1)	N (2)	R (3)	N (4)	R (5)	N (6)	R (7)
<b>Hub (m)</b>	0.044	0.039	0.032	0.051	0.045	0.044	0.041
<b>Mean (m)</b>	0.050	0.050	0.050	0.062	0.062	0.062	0.062
<b>Tip (m)</b>	0.056	0.060	0.068	0.073	0.079	0.080	0.083

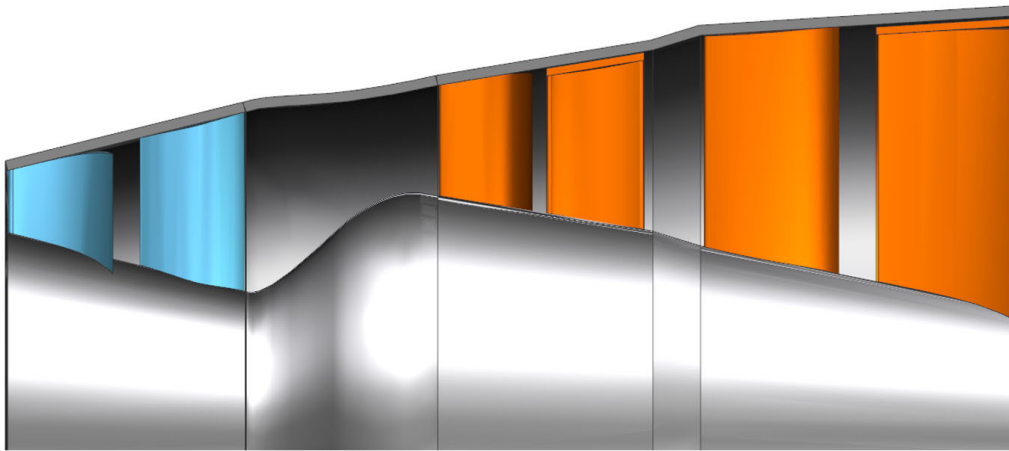


**Figure 4.57: One Stage Gas Generator Turbine and Two-Stage Power Turbine Flowpath**

Once the radii were determined throughout the turbine, the blades were then designed. The blades were designed to have a smooth contraction ratio, as shown in Figure 4.58, following Farokhi [9]. Axial chord was determined from the blade height and the aspect ratio. This then then led to the chord being determined using Eq. 48. Using the chord and the solidity of the blades the spacing was calculated using Eq. 49. Once the spacing was calculated the throat opening was determined using Eq. 50. Table 4.33 shows important blade design characteristics including the number of blades, blade height, aspect ratio, Reynolds number based on chord, and the characteristics discussed in this section.

$$c = \frac{c_z}{\cos(\gamma^\circ)} \tag{Eq. 48}$$

$$s = \frac{c}{\sigma} \tag{Eq. 49}$$

$$o = 0.347 * s \tag{Eq. 50}$$

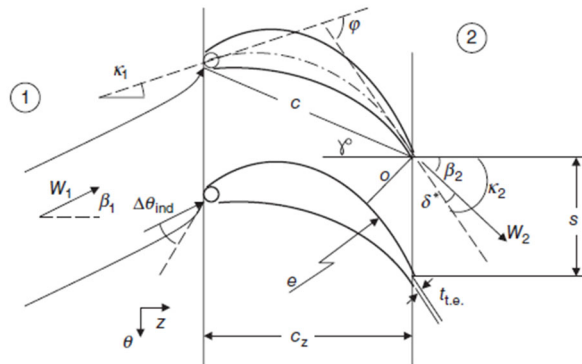


**Figure 4.58: Blade Design Definition Sketch [9]**

**Table 4.33: Salient Blade Design Characteristics**

	HPT		LPT			
	Stage 1		Stage 1		Stage 2	
	N (2)	R (3)	N (4)	R (5)	N (6)	R (7)
<i>h (in)</i>	0.021	0.036	0.035	0.036	0.042	0.050
<i>AR</i>	1	1	1.8	1.8	1.8	1.8
$\sigma$	1.61	1.80	2.83	1.80	3.89	1.97
$\gamma^\circ$	53.9	53.4	39.8	40.6	1.57	1.57
<i>c (m)</i>	0.035	0.035	0.025	0.026	0.028	0.028
<i>s (m)</i>	0.022	0.019	0.009	0.014	0.007	0.014
<i>o (m)</i>	0.008	0.007	0.003	0.005	0.002	0.005
<i># of blades</i>	55	28	73	37	55	28
<i>c<sub>z</sub> (m)</i>	0.021	0.021	0.019	0.019	0.028	0.028
<i>Re (based on c<sub>z</sub> at the hub)</i>	933,000	1,310,000	312,000	260,000	262,000	211,000
<i>Area (m<sup>2</sup>)</i>	0.007	0.011	0.014	0.014	0.042	0.050

The blade design for the turbine can be seen in Figure 4.59. Note that the rotor blades in the power turbine are shrouded. These are shrouded to provide stability and eliminate flutter caused by high aspect ratio blades, which also helps to eliminate tip losses. The rotor was not shrouded on the gas generator turbine because it would add a tip mass to the end of the rotor blade, which would increase the stress experienced by the blade.

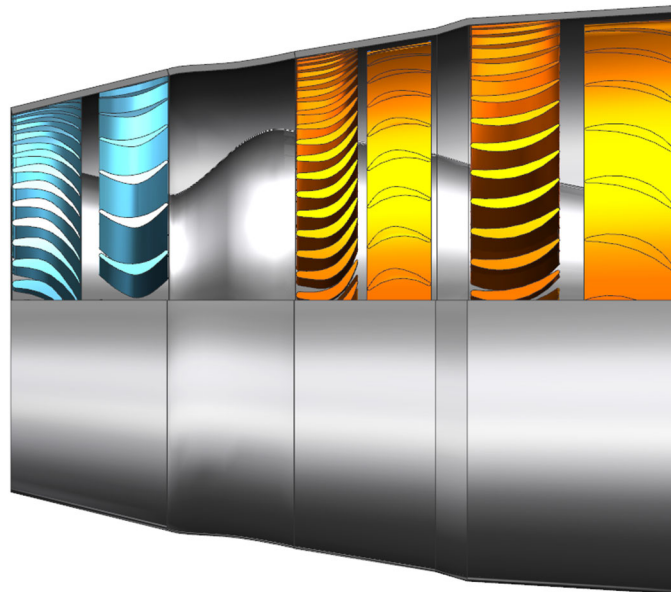


**Figure 4.59: Cutout of the Turbine**

**4.5.4 Turbine Blade Material Selection and Stress Calculations**

The SR-1000BDE uses ceramic matrix composites (CMCs) for the turbine blades. CMC blades are one-third the weight of metallic turbine blades. GE uses a special coating to get the maximum operating

temperature of CMCs up to 1589 K on their GE9x [67]. This allows the designed turbine blades to operate without any cooling, as the maximum operating temperature in the SF1000-BDE is 1456 K. This simplifies the architecture of the engine and increases turbine efficiencies. COI Ceramics Nextel™ AS-N610 Oxide Ceramic Matrix Composite, Aluminosilicate was used for the blades [68]. The casing and hub were chosen to be made of Inconel 625 [69] with a 2 mm thickness, which was determined to be acceptable based on positive margins of safety from the Hoop stress. To be certified, a finite element model would have to be made to determine if this casing thickness would be able to contain a single blade if it were to fail in flight [70]. This material was chosen because it could handle the high temperatures and stresses in the turbine.

Centrifugal and thermal stresses were calculated for the rotor blades in the turbine. The centrifugal stresses were calculated using Eq. 51 and was found to be the determining factor for material selection and sizing of the rotor blades. In an uncooled turbine the thermal stresses are very small because there is not a very large change in temperature and can therefore be neglected. Margins of safety for the rotors can be seen in Table 4.34 as they were the sizing factor for material selection and blade design. The stress on the casing and hub were calculated using the hoop stress equation, as shown in Eq. 52. This gave a positive margin of safety for both the hub and casing with a 2-mm thickness.

**Table 4.34: Blade Stresses**

	$\sigma_c$ (MPa)	MS
<b>R (3)</b>	330	0.11
<b>R (5)</b>	200	0.82
<b>R(7)</b>	173	1.11

$$\sigma_c = \rho_{blade} \frac{\omega^2 A}{4\pi} \left(1 + \frac{A_t}{A_h}\right) \quad \text{Eq. 51}$$

$$\sigma_\theta = \frac{Pr}{t} \quad \text{Eq. 52}$$

Life for the blades was determined based on data from NASA and GE. They estimate anywhere from 1000 hours, based on NASA [7], to above 4000 hours, based on time before overhaul (TBO) from the Catalyst [71], for the life of CMC turbine blades. CMC's are still a very new technology and advancements are being made quite rapidly. For the SR-1000 BDE the life is estimated to be over the

4000-hour mark by the EIS of 2025 for the CMC blades, however it would be recommended to implement a minimum of a 4000-hour TBO.

**4.5.5 Smith Chart**

The efficiency of each stage of the turbine was determined using a Smith Chart, as shown in Figure 4.60. This chart is a function of the stage-loading factor and flow coefficient. These can be calculated using Eq. 53 and Eq. 54 to get the flow coefficients and stage loading factors respectively in Table 4.35 [9]. Once these were calculated, the efficiencies were found to be between 89% and 91.3%, which has been optimized for this design. Multiple iterations and design considerations were evaluated, including lowering the turbine inlet temperature from 1221 K to 1205 K and increasing the power that each stage makes. The power turbine produced 632 hp which is 41 hp more than what GasTurb predicted.

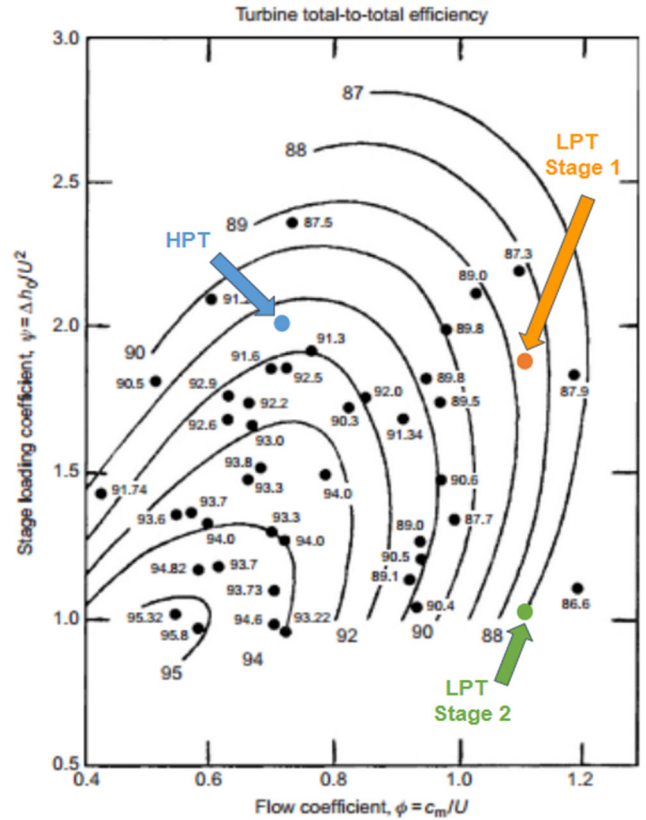


Figure 4.60: Smith Chart [9]

$$\phi = \frac{C_z}{U} \tag{Eq. 53}$$

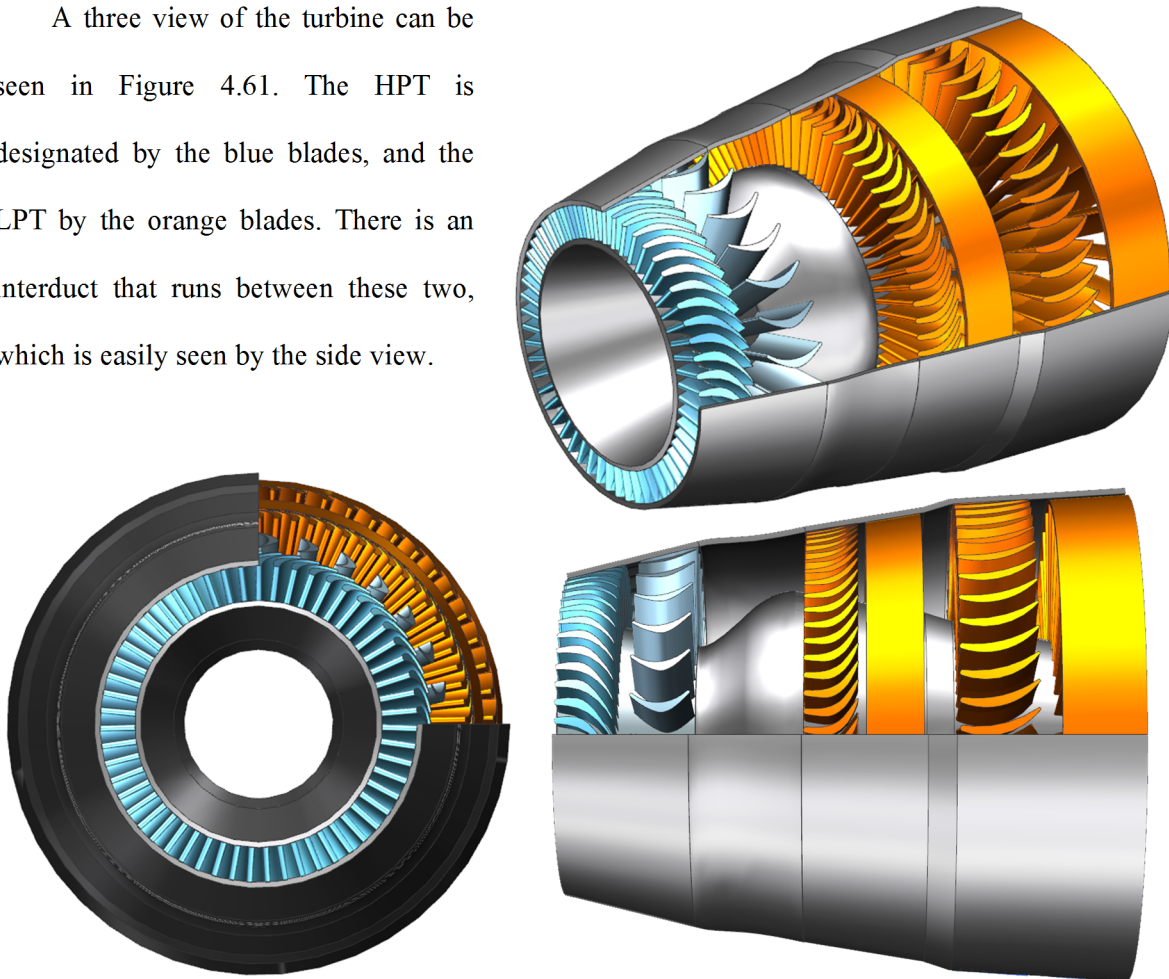
$$\psi = \frac{\Delta h_{stage}}{U^2} \tag{Eq. 54}$$

Table 4.35: Turbine Efficiency

	HPT	LPT	
	Stage 1	Stage 1	Stage 2
Flow coefficient, $\phi$	0.73	1.14	1.14
Stage loading factor, $\psi$	2.06	1.83	0.99
Efficiency	91.3%	89.5%	89.0%

#### 4.5.6 Three-View of the Turbine

A three view of the turbine can be seen in Figure 4.61. The HPT is designated by the blue blades, and the LPT by the orange blades. There is an interduct that runs between these two, which is easily seen by the side view.



**Figure 4.61: Three View of the Turbine**

#### 4.6 Engine Exhaust

The exhaust nozzle is sized to match the nozzle pressure ratio defined in Section 2, 1.1 as recommended by Farokhi [9]. The exhaust produces 77.4 lbs of gross thrust, which equates to 33.1 lbs of net thrust when ram drag is considered. The nozzle does what it was intended to do, which was to overcome the ram drag. The characteristics of the exhaust nozzle are shown in Table 4.36.

The design for the exhaust was based off the exhaust defined in Reference 36 which provides a casing for the recuperator as well as a path for the exhaust gases to vent through the recuperator and exit the

engine. The exhaust bulkhead and casing, seen in Figure 4.62, are made of 2 mm thick 321 stainless steel [72]. This material was chosen for having favorable thermal properties and its wide use in industry [73]. Insulation then fills the bulkhead and casing, providing decreased density for weight savings while maintaining advantageous thermal properties [74].

**Table 4.36: Exhaust Nozzle Parameters**

Parameter	Value
Exit Area (in <sup>2</sup> )	35.07
Exit Velocity at Loiter (ft/s)	589
Nozzle Pressure Ratio	1.1
Gross Thrust (lbf)	77.4
Net Thrust (lbf)	33.1

**Table 4.37: Exhaust Nozzle Flow Data**

Flow Station Data: Exhaust Nozzle	
Inflow (lb/s)	4.23
Corrected Inflow (lb/s)	7.17
Inflow Total Pressure (psi)	12.47
Inflow Total Temperature (°R)	1074.5
Inflow Fuel-air-Ratio	0.013
Inflow Mach #	0.3
Inflow Area (in <sup>2</sup> )	43.03
Pressure Ratio	0.98

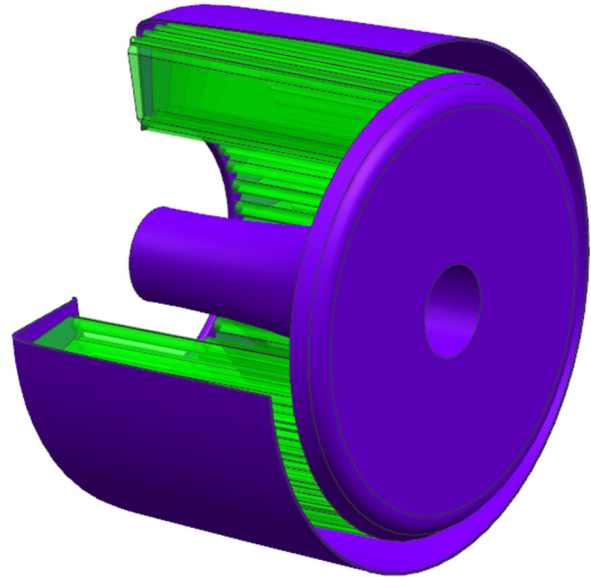


**Figure 4.62: Exhaust Nozzle**

## 5 Engine Subsystems

The SR-1000BDE incorporates numerous innovative subsystem technologies to optimize the performance, maintainability, and efficiency of the engine. These technologies include foil shaft bearings, an advanced FADEC, and an advanced magnetic starter.

### 5.1 Foil Bearing System

The SR-1000BDE uses contactless, gas foil bearings to support the shaft. These self-energizing bearings offer significant advantages over conventional roller bearings. Foremost, the foil bearings do not require the lubrication and cooling systems of conventional systems. In cutting the lubrication system from the engine, engine weight is reduced by 15% [75]. The use of foil bearings was validated by finding

the Sommerfeld Number (SN), shown in the equation below, where a value greater than 6 is deemed favorable for using foil bearings [76]. The SR-1000BDE was found to have an estimated SN of 8.

$$SN = \left(\frac{r}{c}\right)^2 \frac{\mu N}{P} \quad \text{Eq. 52}$$

The Generation III foil bearings will be coated with the NASA-developed PS400 coating. This coating greatly increases wear resistance and allows high temperature operation. The oil-free bearing has a lifespan of 100,000 start/stop cycles, compared to conventional bearing's 9,000-hour lifespan [75]. Generation III foil bearings have a greatly increased load factor over past generations of foil bearings. The foil bearings employed in the SR-1000BDE can be seen in Figure 5.1 and 5.2. The layout of the bearings in the SR-1000BDE can be seen in Figure 5.3.

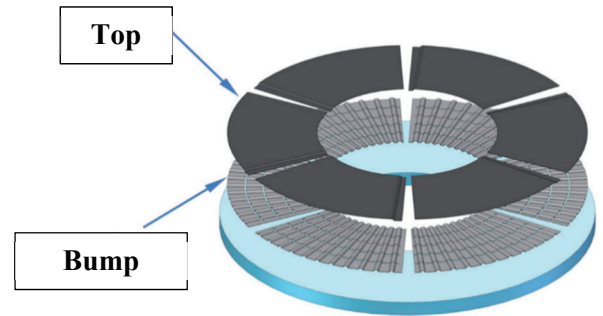


Figure 5.1: Foil Thrust Bearing [80]

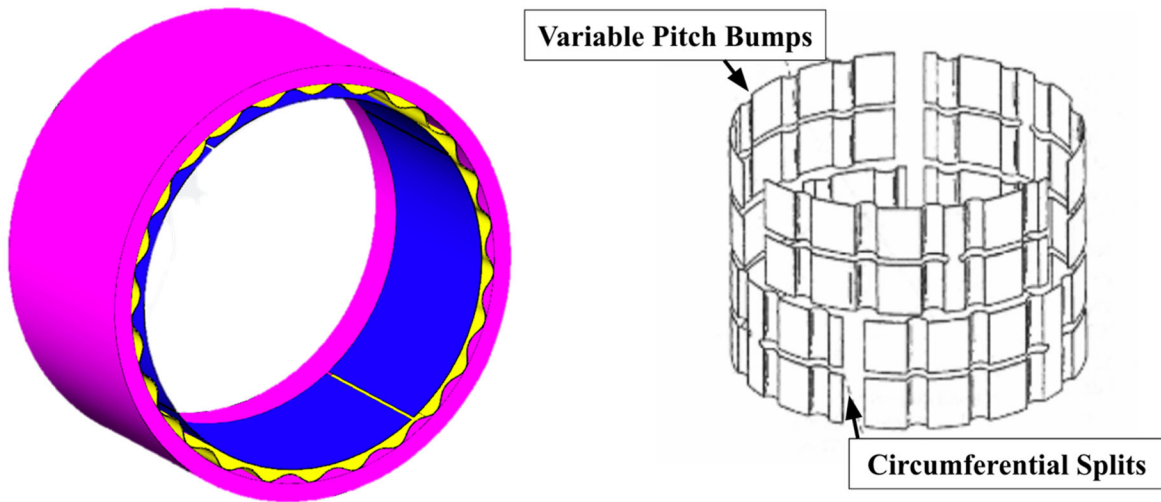


Figure 5.2: CAD of Foil Bearing on Left with Bump Foil Schematic Shown on Right [75]

## 5.2 Starting System

The SR-1000BDE is started by a High Reactance Permanent Magnet Starter/Generator (HRPMM). The high reactance improves the fault-tolerance of the S/G while the HRPMM reduces weight and improves efficiency compared to conventional electric or pneumatic starters. As seen in Figure 5.3, the

starter is located on the compressor shaft. The starter will bring the engine to 40% shaft speed to reach sustainable speeds for stable operation. Honeywell has demonstrated the ability to integrate an HRPMM onto the shaft with foil bearings [82]. Further, a Honeywell-Lockheed Martin Aeronautics effort integrated a HRPMM onto the shaft of the gas turbine engine of the Joint Strike Fighter program [81, 82]. With these programs in mind, it is assessed that the risk of integrating a HRPMM starting system on the SR-1000BDE is low for the 2025 EIS.

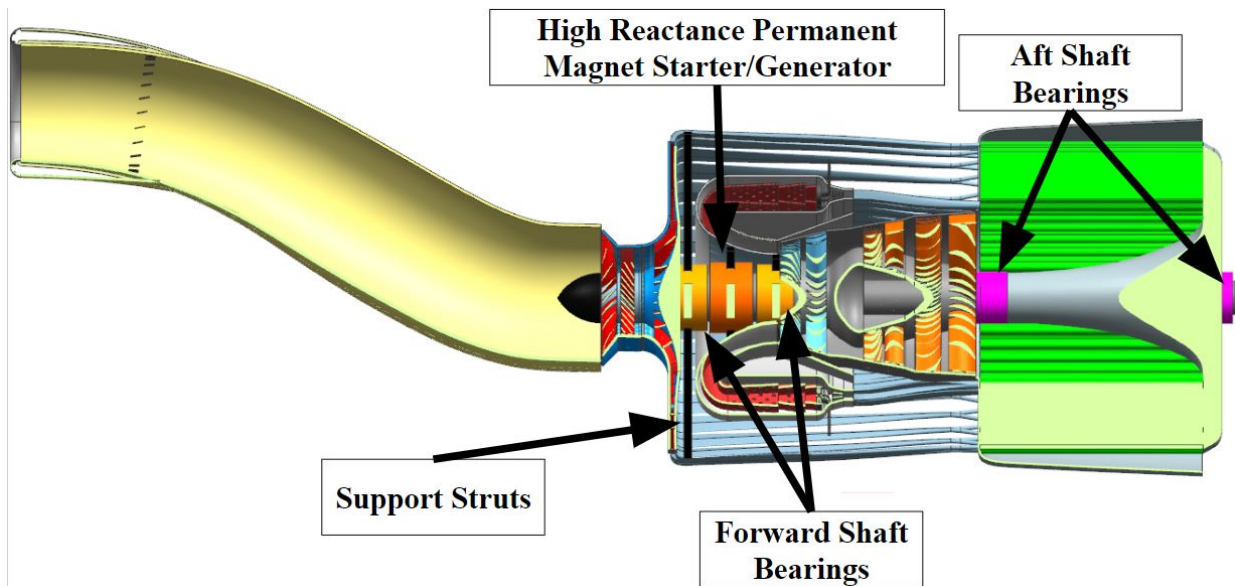


Figure 5.3: Layout of Bearings with Starter Shown in the SR-1000BDE

### 5.3 Full Authority Digital Engine Control

An advanced Full Authority Digital Engine Control (FADEC) is a cutting-edge technology that will be incorporated in the SR-1000BDE. The dual-independent-channel FADEC improves engine reliability, maintainability, and performance. It reduces pilot/operator workload as the entire system is controlled by one power control lever, automating fuel flow and mixture control. The system's Engine Electronic Controller (EEC) automatically adapts the engine for peak efficiency during off-design flight phases. The dual-channel system improves safety and reliability as the channels are independent of each other. Therefore, if a failure occurs in one channel, the redundant channel can keep the aircraft operational. Modern FADEC's, with incorporated redundancies, have demonstrated system reliability matching

mechanical systems across millions of flight hours [8]. The system will monitor engine inlet temperature and pressure, compressor inlet temperature, inter-turbine temperature, exhaust gas temperature, and position feedbacks from the fuel metering valves and actuated parts of the engine. The FADEC also will incorporate a health and usage monitoring system (HUMS). This system allows automatic engine diagnostics for ease-of-maintenance. Further, the FADEC allows for quick, reliable engine restarts. This is crucial to the advanced operational concepts envisioned discussed in later sections. The FADEC onboard the SR-1000BDE incorporates an integrated battery health and thermal management system.

This system will monitor the temperature and loading on the hybrid propulsion system's batteries to prevent overheating and potential failures. Using the onboard batteries, charged by the gas generator, the batteries could power the flight with the SR-1000BDE off. This greatly increases aircraft endurance. The designers included systems to ensure the reliability and safety of this system. Should the monitoring system detect a battery failure, the FADEC will automatically restart the SR-1000BDE gas generator to provide power to the aircraft, ensuring aircraft safety. This system mitigates the risks of modern aircraft onboard battery-power, while helping to ensure system reliability. Current hybrid-battery system designs are limited by cooling requirements. Batteries require all heat to be rejected to the atmosphere, whereas conventional propulsion systems can transfer heat through fluid heat exchangers in the engine [79]. Due to these limitations, the batteries must be monitored to ensure they do not overheat. The thermal management system can balance power delivered from the SR-1000BDE and the batteries while monitoring the battery's thermal condition. This system reduces onboard direct battery cooling needs which greatly reduce the efficiency and increase the weight of hybrid systems. The advanced FADEC onboard the engine ensures the SR-1000BDE offers unparalleled mission reliability and performance while enabling advanced concepts of operation.

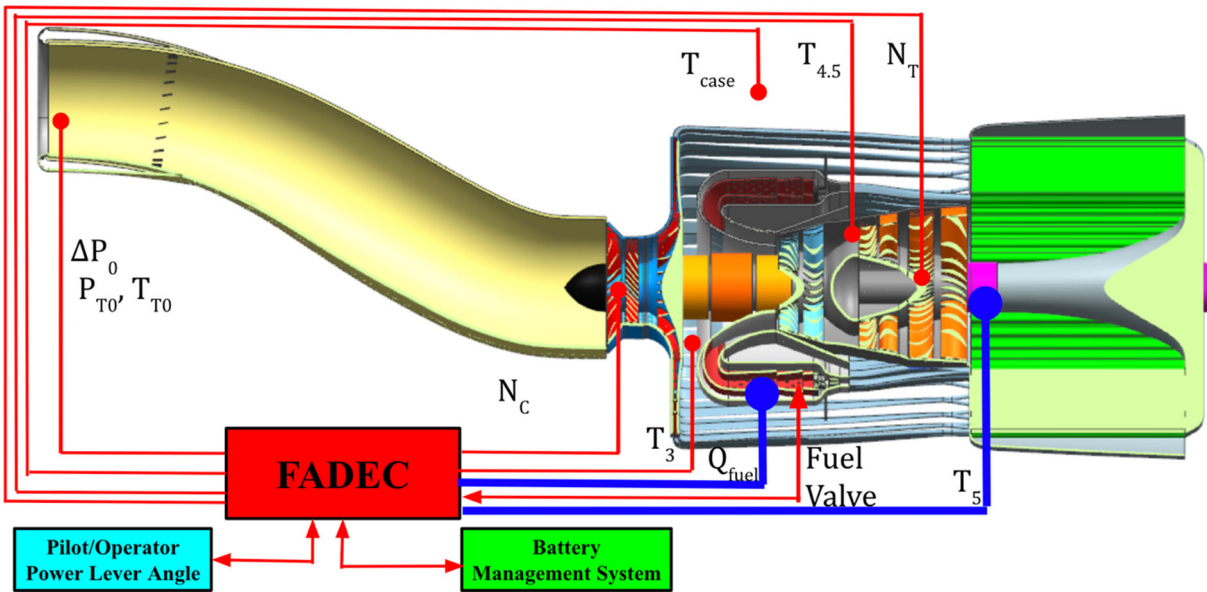
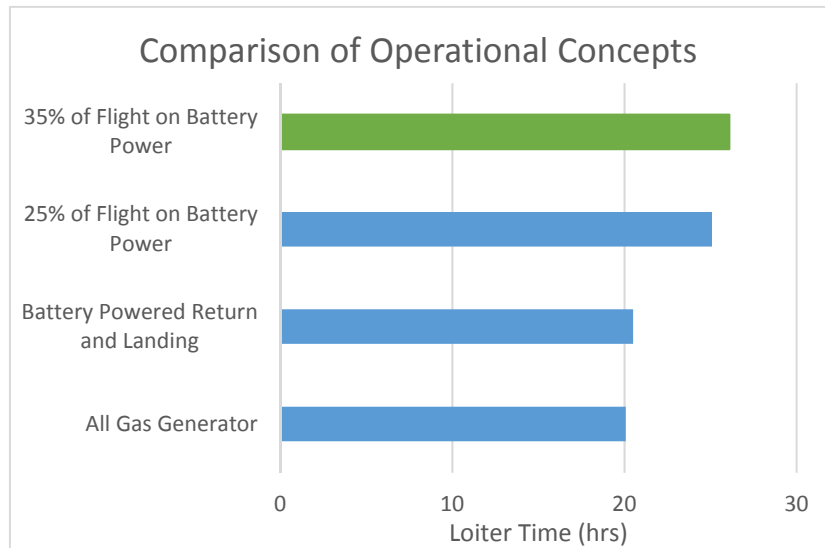


Figure 5.4: SR-1000BDE FADEC Engine Control and Sensor Schematic

#### 5.4 Advanced Operational Concepts

To take full advantage of the potential performance improvements of hybrid-electric propulsion, the SR-1000BDE has been designed with advanced operational concepts in mind. The engine was designed to meet all requirements of the RFP with sole power from the gas turbine. However, with the onboard advanced FADEC, the engine can support advanced concepts of operation to increase overall performance and endurance. Using onboard batteries charged from the SR-1000BDE, the FADEC can shut down the gas generator in flight and transition to the batteries to power the distributed ducted fan system. Figure 5.5 shows a comparison of feasible operational concepts using the SR-1000BDE. Using battery power during the later stages of flight will improve aircraft endurance considerably. It is preferred to use battery power in later stages of flight to reduce the weight of onboard fuel, improving overall efficiency of the flight. The weight of batteries required to power 35% of the flight on battery power was deemed the

maximum allowable following current hybrid-electric industry practices [78]. Regeneration concepts were explored for incorporation in the design of the SR-1000BDE, but studies indicate the energy available for recuperation at less than 0.5% of total mission energy expenditures [79]. As previously discussed, the FADEC is the enabling system for these concepts. Without this advanced system, the engine’s reliability to perform these concepts would falter. High redundancy and reliability, with automatic failure response, is a requirement to execute these concepts.



**Figure 5.5: A Comparison of Viable Operational Concepts with Respect to Loiter Time**

**6 SR-1000 BDE Cost Estimation**

Costs for the SR1000-BDE were estimated using correlations for preliminary engine design provided in Reference 83. These correlations come from turbofan historical data provided by the Rand Corporation. While this engine is not a turbofan, the correlations provide a rough cut for cost estimation. Development costs for this engine were calculated to be \$369 million in 2019 dollars. This cost fits with comparable engines. GE Aviation spent roughly \$400 million to develop their brand-new Catalyst turboprop engine [84]. Acquisition cost for the first production engine was estimated to be \$2.29 million in 2025 dollars. This is expected to drop to \$933,000 for the 375<sup>th</sup> engine produced. Prices in 2025 were calculated using a projected inflation rate of 2.5% [85]. Time Between Overhauls (TBO) is assumed to be 4000 hours for early iterations of this engine. Over time, this should increase as the system performance and fatigue behavior is better characterized. With the advancements in fuel efficiency it was calculated that the SR-

1000BDE will save \$74.66 per hour of loiter when compared to the baseline engine, with the cost of Jet A-1 estimated to be \$3.62 in 2025 [86].

## 7 SR-1000 BDE Weight Estimation

**Table 6.1: SR-1000BDE Weight Estimation**

The weight of the SR-1000BDE was estimated and verified using several methods. Jan Roskam’s Airplane Design Series gave a preliminary range for the weight of our engine [87]. Using

Weight Estimation Method	Resulting Weight (lb)
<b>Roskam</b>	42-136.5
<b>GasTurb 13</b>	62.45
<b>Siemen’s NX</b>	66.48
<b>Siemen’s NX with 1.3 Mass Factor</b>	86.42

GasTurb 13, we found that the unadjusted weight of the engine should be approximately 62.45 lbs. Using the CAD model generated using Siemen’s NX 12, we found our unadjusted weight to be 66.48 lbs. After consulting with Dr. Ian Halliwell [88], we decided to use a mass factor of 1.3 to account for the controls and accessories that our CAD model did not account for. This put the preliminary weight estimate of the SR-1000BDE at 86.42 lbs. This puts our engine close to the center of the range prescribed Jan Roskam. These values are all shown in Table 6.1.

**8 Request for Proposal Requirements Summary**

	<b>TPE331-10</b>	<b>SR-1000BDE</b>	<b>Percent Difference</b>	<b>Requirement Met?</b>
<b>Loiter Fuel Usage (To Reach 20 hours)</b>	993 gal	581 gal	41.5% Decrease	✓
<b>Loiter Time (602 gal Fuel Capacity)</b>	11.64 hrs	20.28 hrs	74.2% Increase	✓
<b>Power to Weight Ratio</b>	2.44 hp/lb	11.39 hp/lb	366.8% Increase	✓
<b>Range (602 gal Fuel Capacity)</b>	2304 nmi	3946 nmi	71.2% Increase	✓
<b>Engine Weight</b>	385 lbf	86.42 lb	77.5% Decrease	✓
<b>Power Output</b>	940 shp	984.5 shp	4.73% Increase	✓

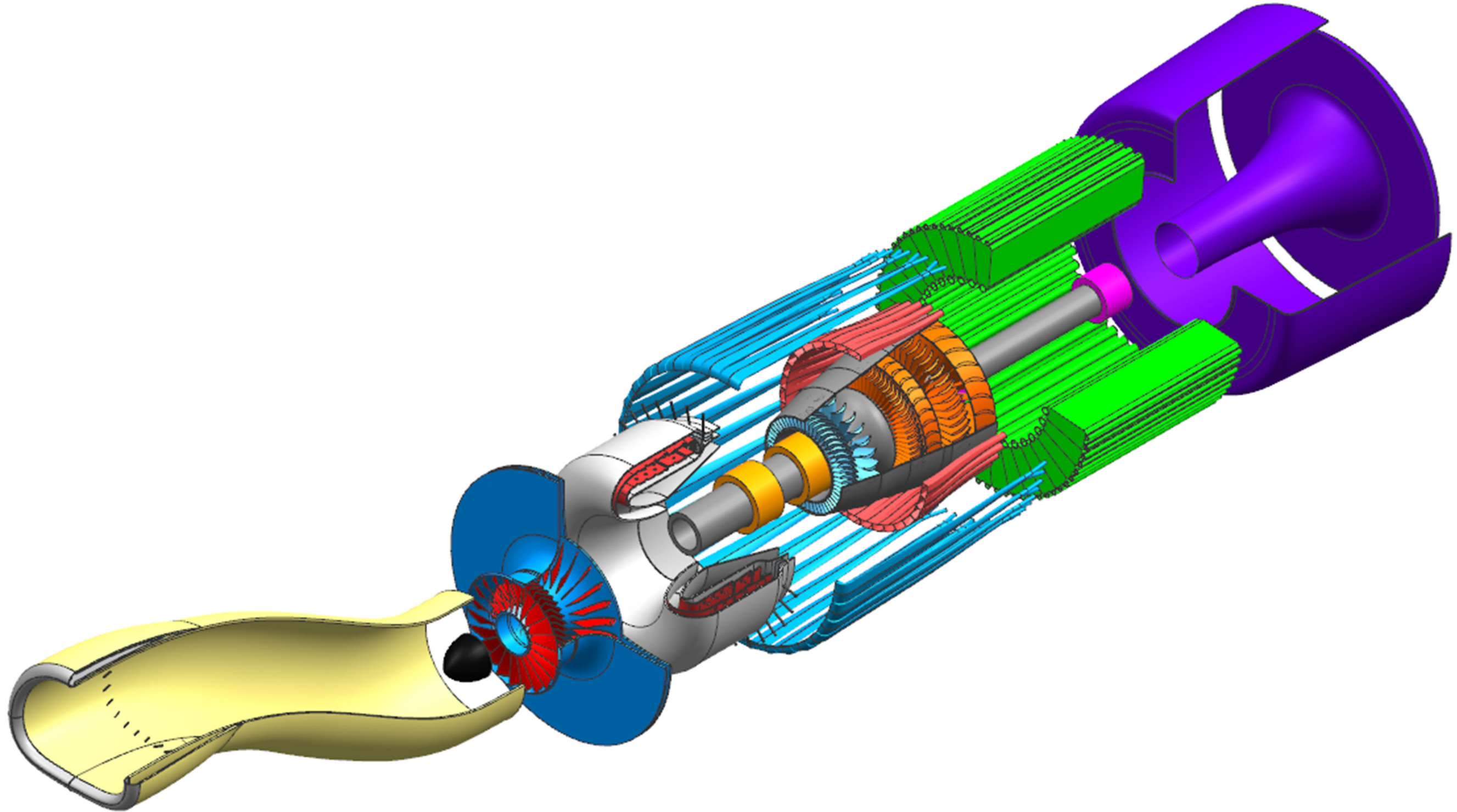


Figure 8.1: SR-1000BDE Exploded View

## 10 References

1. American Institute of Aeronautics and Astronautics, "Candidate Engines for a Hybrid Electric Medium Altitude Long Endurance Search and Rescue UAV," 2018-2019 AIAA Undergraduate Team Engine Design Competition.
2. Brecken, S., "Honeywell Continues to Hone Turboprop Engine for 50th Anniversary," Honeywell Press Release, July 2016.
3. Rhode, S., "Drone Search-and-Rescue Study Reveals Potential, Limits," *AOPA Foundation*, 1 October, 2018.
4. Rolls-Royce, *The Jet Engine (5th Edition)*, S.I.: John Wiley & Sons.
5. Kurzke, Joachim, "GasTurb 13: A Design & Off-Design Performance Program for Gas Turbine,"[<http://www.gasturb.de>], GasTurb GmbH, Templergraben 55, 52062 Aachen, Germany, 2012.
6. "Here's How Ceramic Matrix Composites Are Changing Aviation - GE," *GE Reports* Available: <https://www.ge.com/reports/space-age-cmcs-aviations-new-cup-of-tea/>.
7. Grady, J. E., "CMC Research at NASA Glenn in 2018: Recent Progress and Plans," *US Advanced Ceramics Association*.
8. J. Mattingly, W. Heiser, K. Boyer, B. Haven and D. Pratt, *Aircraft Engine Design*, Reston, AIAA, 2018.
9. Farokhi, S., "Technical Discussion on Nozzle Pressure Ratio," 5 February 2019.
10. Farokhi, S., "Aircraft Propulsion." 2nd Edition, John Wiley & Sons Ltd, West Sussex, United Kingdom, 2014. Print
11. Byung Joon Lee , Takayasu Kumano, Meng Sing Liou, "Design Exploration for Vortex Generators for Boundary-Layer-Ingesting Inlet", 13th AIAA/ISSMO Multidisciplinary Analysis Optimization Conference, AIAA 2010-9399, 13 - 15 September 2010, Fort Worth, Texas
12. Adam Jirasek, "Development and Application of Design Strategy for Design of Vortex Generator Flow Control in Inlets", 44th AIAA Aerospace Sciences Meeting and Exhibit, AIAA 2006-1050, 9-12 January, Reno, Nevada, 2006
13. Bernhard H. Anderson and James Gibb, "Vortex-Generator Installation Studies on Steady-State and Dynamic Distortion", *Journal of Aircraft*, Vol.35, No.4, 1998, pp. 513-520
14. H.A. Rosenthal, D.O. Nelepovitz, H.M. Rockholt, "De-Icing of Aircraft Turbine Engine Inlets", FAA Technical Center, DOT/FAA/CT-87/37, June 1988
15. Zdobyslaw Goraj, "An Overview of the Deicing and Antiicing Technologies with Prospects for the Future", 24th International Congress of the Aeronautical Sciences, Warsaw University of Technology.
16. A.C Kodet, "Electro-Impluse Deicing", *IEEE*, 6 Aug 2002
17. Innovative Dynamics, Inc., "EIDI, Electro Impulse Deicing", Web Page, <http://www.idiny.com/eidi.html>, March 2019.
18. Farokhi, S. "Shortcourse Notes on Preliminary Inlet Sizing and Engine Matching." University of Kansas Department of Aerospace Engineering. Lawrence, KS. 2019
19. Lee, C.C. and Boedicker, C. "Subsonic Diffuser Design and Performance for Advanced Fighter Aircraft", AIAA Paper Number, AIAA-85-3037, 1985.
20. "Inlet Performance." NASA. NASA, n.d. Web. 24 Apr. 2019.
21. Tom Tschida, "Satellite antenna and sensors of a NOAA-NASA flight demonstrator, 2005", NASA Dryden Flight Research Center, EC05-0090-19, 20 Apr. 2005
22. Abbot, Anderson, and Rice, 1987.
23. O'Connor, D. "The 3D printing industry temporal illusion", *The Magazine for Design-to-Manufacturing Innovation*.
24. Federal Aviation Administration, "Frequently Asked Questions and Answers", United States Department of Transportation, [www.faa.gov](http://www.faa.gov), n.d., 13 Dec, 2018.
25. Miller, Wilmer J. (1969-01-16). "The biology and Natural History of the Mourning Dove". Retrieved 2008-04-14.
26. Barrett, R., Private Communication, March 2019
27. Ewing, M., Private Communication, March 2019
28. MatWeb Material Property Data, "Cytec (Solvay Group) CYCOM® 985 Epoxy + Kevlar 49 Fiber Laminate", [www.matweb.com](http://www.matweb.com), n.d., Mar 2019.
29. MatWeb Material Property Data, "DuPont Performance Polymers Vespel® SF-0940 Polyimide Foam, High Density", [www.matweb.com](http://www.matweb.com), n.d., Mar 2019.
30. MatWeb Material Property Data, "Alclad Aluminum 2024-T3", [www.matweb.com](http://www.matweb.com), n.d., Mar 2019.



31. Anon., "Williams International," Williams International Web Site, [<http://www.williams-int.com/products>], Spring, 2019
32. Farokhi, S., Private Communication, April 2019.
33. Farokhi, S., "Excerpt from Aircraft Propulsion Notes: Compressor," The University of Kansas Department of Aerospace Engineering, Lawrence, KS, 2018.
34. Lagow, B. W., "Materials Selection in Gas Turbine Engine Design and the Role of Low Thermal Expansion Materials,"
35. Carozza, A., "Heat Exchangers in the Aviation Engineering,"
36. Vick, M. J., Heyes, A., and Pullen, K. R., "Design overview of a three-kilowatt recuperated ceramic turboshaft engine," ASME Turbo Expo 2009, GT2009-60297, June 8-12, 2009, Orlando, FL, USA.
37. McDonald, C. F., Massardo, A. F., "Recuperated gas turbine aeroengines, part II: engine design studies following early development testing", Aircraft Engineering and Aerospace Technology, Vol. 80 Issue: 3, pp.280-294, <https://doi.org/10.1108/00022660810873719>.
38. McDonald, C. F., "Gas Turbine Recuperator Technology Advancements," The American Society of Mechanical Engineers, 1972.
39. Misirlis, D., Vlahostergios, Z., et. al., "Optimization of Heat Exchangers for Intercooled Recuperated Aero Engines," *Aerospace – Open Access Journal*, 2017.
40. Muley, A., "Advanced Heat Exchangers for Enhanced Air-Side Performance: A Design and Manufacturing Perspective," ARPA-E Advanced Dry Power Plant Cooling Workshop, 2010.
41. Anon., "Classification of Heat Exchangers," 2012.
42. McDonald, C. F., "Recuperator Development Trends for Future High Temperature Gas Turbines," The American Society of Mechanical Engineers, 1975.
43. Jackson, T. B., Virkar, A. V., et. al., "High-Thermal-Conductivity Aluminum Nitride Ceramics: The Effect of Thermodynamic, Kinetic, and Microstructural Factors," *Journal of the American Ceramic Society*, Vol. 80, No. 6, 1997.
44. Kee, R. J., Almand, B., B., et. Al, "The design, fabrication, and evaluation of a ceramic counter-flow microchannel heat exchanger," *Applied Thermal Engineering*, vol. 31, 2011.
45. Wilson, M. A., Rechnagle, K., "Design and Development of a Low-Cost, High Temperature Silicon Carbide Micro-Channel Recuperator," ASME Turbo Expo 2005: Power for Land, Sea and Air, 2005.
46. Lefebvre, A. H., Ballal, D. R., *Gas Turbine Combustion: Alternative Fuels and Emissions*, CRC Press, 2018.
47. Anon., "Types of Aviation Fuel," *Aeronautics Guide*, Jun. 2017. [<https://www.aircraftsystemstech.com/2017/06/types-of-aviation-fuel.html>]
48. Adkins, R.C., Matharu, D.S., Yost, J. O., "The Hybrid Diffuser," *Journal of Engineering and Power*, Vol. 103, Issue 1, 1981, pp. 229.236.
49. Walker, A. D., "Experimental and computational study of hybrid diffusers for gas turbine combustors," Ph.D. Dissertation, Department of Aeronautical and Automotive Engineering, Loughborough University, 2002.
50. Xing, F., Su, H., Chan, S., Xu, L., Yu, X., "Optimization Study of the Dump Diffuser in Gas Turbine to Reduce Pressure Loss," *International Journal of Aerospace Engineering*, 2018.
51. Walker, A. D., McGuirt, J. J., "The Influence of Dump Gap on External Combustor Aerodynamics at High Fuel Injector Flow Rates," *Journal of Engineering for Gas Turbines and Power*, May 2009.
52. He, P., Suo, J., Xie, K., Chen, S., Shen, S., Zeng, Q., "Influence of Dump Gap on Aerodynamic Performance of a Low-Emission Combustor Dump Diffuser," *ASME Turbo Expo 2013: Turbine Technical Conference and Exposition*, ASME, Jun. 2013.
53. Environmental Protection Agency, "Control of Air Pollution from Aircraft and Aircraft Engines; Emission Standards and Test Procedures; Final Rule," *Federal Register*, Jun. 2012.
54. Henderson, R. E., Blazowski, W. S., "Turbopropulsion Combustion Technology," *Aircraft Propulsion Systems Technology and Design*, 1<sup>st</sup> ed., AIAA, 1989, pp. 103-165.
55. Levy, D., "Ceramic matrix composites take flight in LEAP jet engine," Oak Ridge National Laboratory, Jan. 2017. [<https://www.ornl.gov/news/ceramic-matrix-composites-take-flight-leap-jet-engine>]
56. DiCarlo, J. A., Yun, H. M., Morscher, G. N., Bahatt, R. T., "SiC/SiC Composites for 1200°C and Above," NASA TM-2004-213048.
57. Vedula, V., Shi, J., Liu, S., Jarmon, D., "Sector Rig Test of a Ceramic Matrix Composite (CMC) Combustor Liner," *ASME Turbo Expo 2006: Power for Land, Sea, and Air*, ASME, May 2006.



58. Mavris, D., Tai, J., Denney, R., Yang, P., “Enhanced Emission Prediction Modeling and Analysis for Conceptual Design,” Georgia Institute of Technology, Nov. 2010.
59. Norgren, C. T., Riddlebaugh, S. M., “Effect of Fuel Injector Type on Performance and Emission of Reverse-Flow Combustor,” NASA TP-1945, Dec. 1981.
60. Batarseh, F. Z., Tropea, C., Dreizler, A., Roisman, H. I. V., “Spray Generated by an Airblast Atomizer: Atomization, Propagation, and Aerodynamic Instability,” Ph.D. Dissertation, Department of Mechanical Engineering, Technical University of Darmstadt, 2008.
61. Department of Defense, “Metallic Materials and Elements for Aerospace Vehicle Structures,” MIL-HDBK-5H, 1998.
62. Anon., “Altitude above Sea Level and Air Pressure,” The Engineering ToolBox, 2003. [[https://www.engineeringtoolbox.com/air-altitude-pressure-d\\_462.html](https://www.engineeringtoolbox.com/air-altitude-pressure-d_462.html)]
63. Panigrahi, S. K., Sarangi, N., Chandrasekhar, U., “Experimental Evaluation of Overload Capacity of an Annular Combustor Casing of a Gas Turbine Engine,” *Experimental Techniques*, Vol. 40, Issue 2, 2016, pp. 841-848.
64. Anon., “Inconel Alloy 718,” Special Metals, Sep. 2007. [[http://www.specialmetals.com/assets/smc/documents/inconel\\_alloy\\_718.pdf](http://www.specialmetals.com/assets/smc/documents/inconel_alloy_718.pdf)]
65. Park, S., Seo, M., “Interface Science and Composites,” *Interface Science and Technology*, Vol. 18, 2011, pp. 501-629.
66. Moroz, L., Pagur, P. Govorushchenko, Y., Grebennik, K., “Comparison of Counter-rotating and Traditional Axial Aircraft Low-pressure Turbines Integral and Detailed Performances,” Softinway Web Site, [<http://www.softinway.com/en/education/articles-and-technical-papers/>], August 2009
67. Kellner, Tomas, “GE Develops Jet Engines Made From Ceramic Matrix Composite,” GE Reports Website, [<https://www.ge.com/reports/post/112705004705/ge-develops-jet-engines-made-from-ceramic-matrix/>], March 2015
68. Anon, “Aluminosilicate Matrix CMCs Mechanical Properties,” COI Ceramics Inc. Web Site, [<http://www.coiceramics.com/oxidepg.html>]
69. Anon, “INCONEL® alloy 625,” Special Metals Web Site, [<http://www.specialmetals.com/tech-center/alloys.html>], 2018
70. Jain, Rajeev, “Prediction of Transient Loads and Perforation of Engine Casing During Blade-Off Event of Fan Rotor Assembly,” SEMI MAC Website, [<http://semimac.org/wp-content/uploads/2015/12/sem.org-IMPLAST-2010-SEM-Fall-s006p01-Prediction-Transient-Loads-Perforation-Engine-Casing-During.pdf>], October 2010
71. Anon, “GE Catalyst,” GE Aviation Website, [<https://www.geaviation.com/bga/engines/ge-catalyst>], 2019
72. Anon., “321 Stainless Steel Sheet, Coil, Plate & Bar – AMS 5510, 5645,” *United Performance Metals Material Summary Page*, 6 May, 2019.
73. Anon., “Aircraft Exhaust Catalog,” *Acorn Welding Website*, 6 May 2019.
74. Anon., “Thermo-Tec Exhaust Insulating Wrap,” *Aircraft Spruce & Specialty Company Website*, 6 May 2019.
75. Anon. (2001). *Creating a Turbomachinery Revolution*. (NASA Glenn Research Center) Retrieved April 02, 2019, from <https://www.nasa.gov/centers/glenn/about/fs14grc.html>
76. Anon. (2013, October). *Guidelines for Determining Foil Bearing Applicability*. (Barber-Nichols Inc.) Retrieved March 28, 2019
77. Anon. (2017). Typical Fadec Structure. (Aviation Stack Exchanges) Retrieved February 22, 2019
78. Anon. (n.d.). Panthera. (Pipistrel USA) Retrieved April 15, 2019, from <https://www.pipistrel-usa.com/panthera/>
79. Epstein, A., & O’Flarity, S. (2019). Considerations for Reducing Aviation’s CO2 with Aircraft Electric Propulsion. *Journal of Propulsion and Power*.
80. . Feng, K., Liu, L., Guo, Z., & Zhao, X. (2014). Parametric study on static and dynamic characteristics of bump-type gas foil thrust bearing for oil-free turbomachinery. *Journal of Engineering Tribology*.
81. Ganev, E. (2006). High Reactance Permanent Magnet Machine for High-Performance Power Generation Systems. SAE Power Systems Conference.
82. Zhang, Z., Huang, J., Jiang, Y., Geng, W., & Xu, Y. (2017). Overview and Analysis of PM Starter/Generator for Aircraft Electrical Power Systems. *CES Transactions on Electrical Machines and Systems*, 1(2), 117-131.
83. Byerley, A., Rolling, A., Treuren, K., “Estimating Gas Turbine Engine Weight, Costs, and Development Time During the Preliminary Aircraft Engine Design Process,” *ASME Turbo Expo 2013: Turbine Technical Conference and Exposition*, ASME, June 2013.

84. Anon, "GE announces name for its Advanced turboprop: The GE Catalyst engine," GE Aviation Website, [<https://www.geaviation.com/press-release/business-general-aviation/ge-announces-name-its-advanced-turboprop-ge-catalyst%E2%84%A2-engine>], 2019
85. Anon, "Inflation Calculator," Smart Asset Website, [<https://smartasset.com/investing/inflation-calculator#NY0qGJA3KW>], 2019
86. *FAA Aerospace Forecast: Fiscal Years 2017-2037*, 2017.
87. Roskam, Jan, Airplane Design: Part V, Component Weight Estimation, *DARcorporation*, Lawrence, KS, 2005.
88. Halliwell, I. "Technical Discussion on Engine Weight Estimation," 15 April 2019.